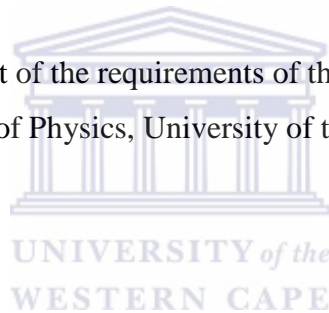


DYNAMIC VARIATION OF HYDROGEN DILUTION DURING HOT-WIRE CHEMICAL VAPOUR DEPOSITION OF SILICON THIN FILMS

by

NAZLEY TOWFIE

Submitted in partial fulfilment of the requirements of the degree Magister Scientiae in the
Department of Physics, University of the Western Cape



Supervisor: Prof. C. J. Arendse, University of the Western Cape

Co-supervisor: Dr. T. F. G. Muller, University of the Western Cape and Dr. G. Malgas, Council of Scientific and Industrial Research (CSIR)

SEPTEMBER 2013

KEYWORDS

DYNAMIC VARIATION OF HYDROGEN DILUTION DURING HOT-WIRE CHEMICAL VAPOUR DEPOSITION OF SILICON THIN FILMS

Nazley Towfie

Hydrogenated amorphous silicon

Hydrogenated nanocrystalline silicon

Hot wire chemical vapour deposition

Tandem solar cells

Nano-voids

Morphology

Microstructure

Hydrogen Etching



ABSTRACT

DYNAMIC VARIATION OF HYDROGEN DILUTION DURING HOT-WIRE CHEMICAL VAPOUR DEPOSITION OF SILICON THIN FILMS

Nazley Towfie

MSc Thesis, Department of Physics, University of the Western Cape

It has been debated that among all the renewable energy alternatives, only solar energy offers sufficient resources to meet energy demands. Silicon thin film solar cells are at the frontier of commercial solar technology. Hot wire chemical vapour deposition (HWCVD) is the technique of choice for silicon thin film deposition due to the absence of ion bombardment and its independence toward geometry or electromagnetic properties of the substrate, as seen by plasma enhanced chemical vapour deposition (PECVD). With the implementation of nanostructures in a multi-band gap tandem solar cell, considerable improvement has been achieved over the single junction solar cells. Defect assisted tunnelling processes at the junctions between individual solar cells in a tandem structure solar cell largely affect the efficiency of these solar cells. In this contribution, the investigation toward the improvement of silicon thin films for tandem solar cell application is initiated.

This study reports on the effects of hydrogen dilution and deposition time on six silicon thin films deposited at six specific deposition regimes. The thin film properties are investigated via X-Ray diffraction analysis, Raman spectroscopy, Fourier transform infra-red spectroscopy, elastic recoil detection analysis, scanning and transmission electron microscopy and UV-visible spectroscopy. This investigation revealed the dominating etching effect of atomic hydrogen with the increase in hydrogen dilution and a bonded hydrogen content (C_H) exceeding 10 at.% for

each of the six thin films. The optically determined void volume fraction and static refractive index remain constant, for each thin film, with the change in C_H .

A new deposition procedure, utilising the deposition conditions of the previously investigated thin films, is performed by HWCVD to deposit two silicon thin films. This deposition procedure involved either increasing (protocol 1) or decreasing (protocol 2) hydrogen dilution during deposition. Structural and optical variation with depth was observed for the dynamically deposited silicon thin films, with nano-voids existing across the entire cross section and bond angle variations which are indicative of good structural order. The optical absorption curves differ for the two silicon thin films whereas the optical density remains constant for both.



Declaration

I declare that

**“DYNAMIC VARIATION OF HYDROGEN
DILUTION DURING HOT-WIRE
CHEMICAL VAPOUR DEPOSITION OF
SILICON THIN FILMS”**



Is my own work, that it has not been submitted for any degree or examination in any other university and that all the sources I have used or quoted have been indicated and acknowledged by means of complete references.

Name: Nazley Towfie

Date: September 2013

Signature:

Acknowledgements

I am speechless with gratitude and joy to the following people and organisations without whose assistance, advice and guidance, this thesis would not have been possible.

Professor C. J. Arendse for his encouragement, insight, patience and guidance throughout this process.

Dr T. G. Muller (UWC) and Dr G. Malgas (CSIR) for their support and co-supervision.

Professor B. Julies (EMU, UWC) for his time and assistance during the electron microscopy studies.

Staff of UWC physics department for their support and care.

My immediate and extended friends and family for all their encouragement and support, particularly to my parents, Suheimah and Shaheed Towfie for being my inspiration and motivation to do great things and allowing me to follow my passions.

To my colleagues and friends Razia Adam, Abdul Ghaaliq Adams, Natasha Petersen, Valentino van de Heyde, Sulaiman Jacobs, Mishka Ebrahim and Shuayb Davids for helping me keep my sanity throughout the duration of my thesis work.

NRF for the opportunity to further my studies and for their gracious financial support.

Table of Contents

TITLE PAGE	I
KEYWORD	II
ABSTRACT	III
DECLARATION	V
ACKNOWLEDGEMENTS	VI
CHAPTER ONE: INTRODUCTION	1-25
1.1 The solar heritage.....	1
1.2. Amorphous silicon	5
1.2.1. Structural Properties.....	5
1.2.1. Doping	8
1.2.2. Metastability: The Staebler – Wronski Effect	9
1.3. Nanocrystalline Silicon.....	10
1.3.1. Growth Models.....	11
1.3.1.1. Selective etching model	11
1.3.1.2. Chemical annealing model.....	12
1.3.1.3. Surface diffusion model	13
1.4. Application: Solar Cells	14
1.4.1. Operating Principles	14
1.4.2. Single junction solar cells.....	16
1.4.3. Multi-junction solar cells.....	17
1.5. Aims and Outlines	19

CHAPTER TWO: HOT WIRE CHEMICAL VAPOUR DEPOSITION

SYSTEM.....	26-38
2.1. Introduction.....	26
2.2. Hot-wire chemical vapour deposition system.....	27
2.3. Gas Inlet System	29
2.4. Growth Mechanism for a- and nc-Si:H.....	32
2.4.1. Dissociation at the filament	32
2.4.2. Gas phase reactions.....	33
2.4.3. Film growth.....	35

CHAPTER THREE: ANALYTICAL TECHNIQUES 39-81

3.1. Introduction.....	39
3.2. UV-Vis Spectroscopy	40
3.3. X-ray Diffraction	46
3.4. Raman Spectroscopy	53
3.5. Fourier Transform Infra-red Spectroscopy	55
3.6. Elastic Recoil Detection Analysis.....	59
3.7. Atomic Force Microscopy	62
3.8. Scanning Electron Microscopy	65
3.9. Transmission Electron Microscopy	71

CHAPTER FOUR: STRUCTURAL AND OPTICAL PROPERTIES OF SILICON THIN FILMS 82-119

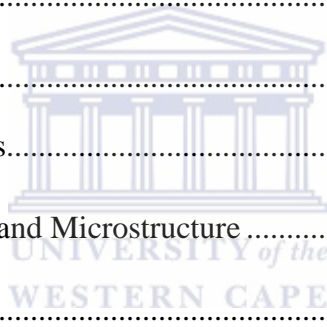
4.1. Introduction	81
4.2. Experimental Details.....	82

4.3. Results and Discussion	85
4.3.1. Structural Properties.....	85
4.3.1. Hydrogen Configuration	91
4.3.2. Morphological Investigation	101
4.3.3. Optical Properties	106
4.4. Conclusion	114

CHAPTER FIVE: SILICON THIN FILMS BY DANAMIC VARIATION OF HYDROGEN DILUTION..... 120-144

5.1. Introduction	119
5.2. Experimental Details.....	120
5.3. Results and Discussion	123
5.3.1. Structural Properties.....	123
5.3.2. Hydrogen Bonding and Microstructure	130
5.3.2. Optical Properties.....	134
5.4. Conclusion	141

SUMMARY 145-147



CHAPTER ONE

INTRODUCTION

1.1 The solar heritage

Energy is the most vital commodity needed to sustain life. With the dawn of the industrial era, the depletion of fossil fuels such as oil, coal, natural gas and the on-going changes in the earth's climate leaves our future uncertain. In addition to the high safety risk of nuclear power, great attention is now paid to alternative renewable energy sources and methods of generating power. Many alternatives show great promise in efficient and low cost energy production, such as fuel cells, wind energy, hydrostatic energy, turbines and photovoltaic's [1.1].

The sun's radiation is the primary source of energy for all living species on Earth. Its energy is derived from the nuclear fusion of hydrogen that results in the release of energy from the surface. On average one square meter of the earth receives an amount of energy equal to fourteen 100 W light bulbs per second [1.2]. Photovoltaic devices make use of this energy to do a direct conversion of solar energy into electrical power, due to the photoelectric effect. With the enormous amount of free energy readily provided by the sun, solar energy becomes an ideal alternative as seen in figure 1.1, which displays the thermal energy map of Africa. It has been estimated by the International Energy Agency's photovoltaic roadmap that by 2050 photovoltaic systems will provide approximately 11% of the global electricity production and avoid 2.3 gigatons of CO₂ emissions per annum [1.3].

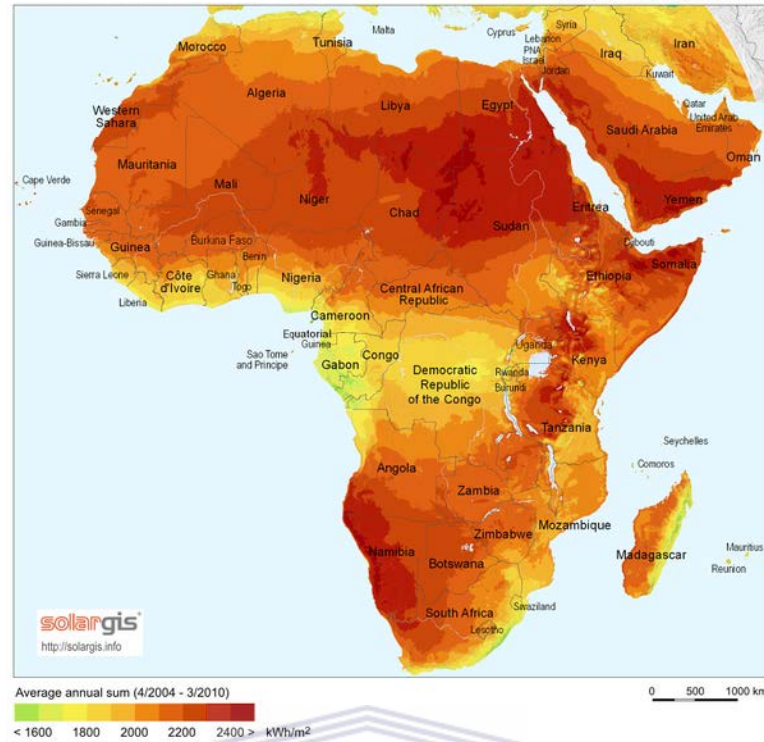
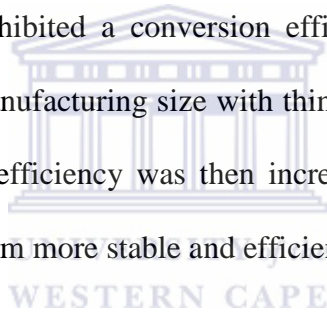


Figure 1.1 Thermal map of the earth depicting the average energy (kWh) received from the sun per m² between the years 2004-2010 [1.4].

In the 1950's it was found, with the development of high-quality silicon wafers, that potentially useful quantities of power could be produced by a photovoltaic devices using crystalline silicon. Following the development of silicon electronics, was the birth of the first silicon solar cell in 1954 by Chapin, Fuller and Pearson, with an efficiency of 6% [1.2]. This was then classified as a first generation photovoltaic device. At the time these cells were not considered much for power generation, as the scarcity of energy resources were not in question, and the efficiency of established solar cells produced then were low. It was however found useful in 1958 with the successful launch of the first solar powered satellite, Vanguard. Vanguard's solar technology paved the way for satellites that followed, since satellite solar cells operated for about seven years, while conventional batteries powered on board transmitters lasted only 20 days. After the last solar cell died in 1964 the Vanguard fell silent, but continues to allow mankind to understand and discover the effects of the sun, moon and atmosphere on the orbits of satellites [1.5].

The energy supply crisis in 1970 then led to the major growth interest in alternative energy sources and the improvement of solar cell efficiencies on Earth. Today crystalline silicon solar cells reach an efficiency of 25% and are highly stable under illumination of the sun [1.6]. Even though the stability of crystalline silicon solar cells was extremely good; the cost of production is still not competitive to fossil fuels.

Research then focused on methods of cheap production of solar cells and its improvement. The idea of thin film silicon solar cells intrigued the minds of scientist for decades and in 1976 Carlson and Wronski produced the first experimental amorphous silicon thin film solar cell deposited on a glass substrate at RCA laboratories [1.7]. This formed part of the second generation of photovoltaic devices. This thin film amorphous silicon solar cell drastically reduced production cost, but exhibited a conversion efficiency of only 2.4% [1.8]. Another advantage was the increase in manufacturing size with thin film solar cells compared to the first generation solar cell [1.9]. The efficiency was then increased by the alloying of silicon with hydrogen, which made the thin film more stable and efficient.



Other thin films such as GaAs and CdTe show high efficiencies approaching that of crystalline silicon. The Fraunhofer Institute of Solar Energy Systems has reported an efficiency of 24% for a single junction GaAs solar cell. It however fails to impress when it comes to manufacturing costs of such solar cells. The production and material acquisition becomes expensive due to the rarity of a material type and production time.

The concept of a multi-junction solar cell was introduced to improve the output voltage of hydrogenated amorphous silicon. “Stacked” solar cells showed an improved stability and each junction can be tailored to absorb a specific region of the solar spectrum which resulted in an increase in light absorption [1.8]. Concentrated photovoltaic systems were then introduced as a method to increase the power output even further. It uses lenses and mirrors to concentrate direct

sunlight onto a small, multi-junction solar cell. Laboratory efficiencies have reached 40% though commercially only 25% [1.10]. Though efficient, the production costs are extremely high due to the requirement of a multi-junction solar cell and a sun tracking system, for maximum efficiencies.

Polymeric and dye sensitized solar cells are still in the early research and development stage and are considered to be the third generation of solar power devices. Its success, however, in comparison to existing technologies is yet to be determined. Polymeric photovoltaic's are inexpensive and inefficient at this stage. They are made of organic or polymer material which suffer high degradation effects in short periods of time. Reported efficiencies range between 8 and 12% [1.11]. The advantage is that it can be applied on plastic sheets which make it light, flexible and cheap [1.12]. Dye sensitized solar cells on the other hand is based on photo-electrochemical sciences. The interesting theme to this type of thin film solar cells is that it mimics natural photosynthesis. It has reported efficiencies of 12%, and the major obstacle facing this technology is the limited number of dyes able to absorb different spectral ranges [1.13, 1.14]. Nanocrystalline semiconductors can however allow dye sensitized solar cells to have a broader spectral coverage and is attracting many researchers attention. Nanocrystalline semiconductors are not only an interesting topic for dye sensitized solar cells but also thin film solar cells as a whole.

In the ever continuing stride to not only increase solar cell efficiency but also reduce manufacturing cost such that photovoltaic technologies can be accessible to all, we aim to push the frontiers of science with innovative and efficient new ideas. To do so we will first investigate the current state of research for second generation silicon thin films.

1.2 Amorphous silicon

1.2.1 Structural properties

Crystalline silicon (c-Si) has an atomic mass of 28.08 amu and is part of the diamond lattice group. The covalent bonding of each silicon (Si) atom to four neighbouring silicon atoms bring about the periodic nature and long range order observed for c-Si. The angle between two Si-Si bonds are exactly 109.5° and the bond length is fixed at 0.235 nm.

Contrary to the perfectly ordered structure presented above, amorphous silicon (a-Si) tells a whole different story. A periodic nature is not maintained throughout the material, though short range order is still present. The variations in the bond length and the bond angle result in the bonds between neighbouring Si atoms to break. When these bonds break, defects are created in the atomic structure of the material. Dangling bonds, or uncoordinated silicon atoms, form and this then gives a-Si a continuous random network structure [1.15]. The figure below is a graphical representation of atomic structure of a- and c-Si.

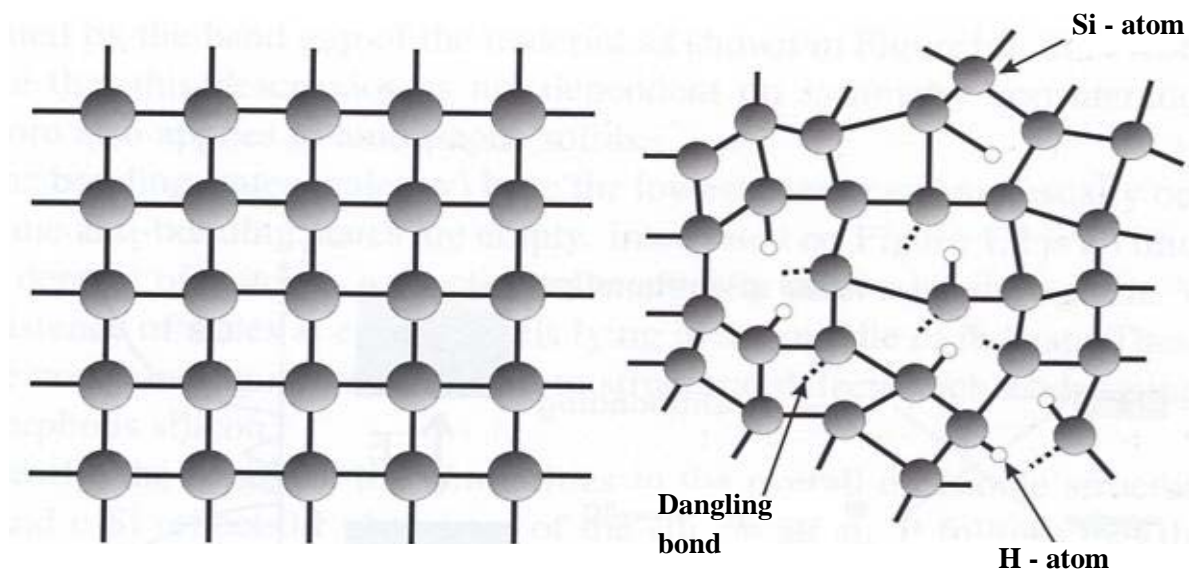
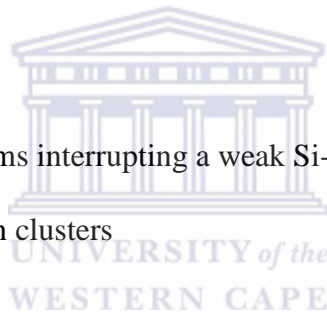


Figure 1.2 2D representation of a) crystalline silicon and b) amorphous silicon where the closed circles are silicon atoms and the open circles are hydrogen atoms [1.16]

The absorption of photons in a-Si is extremely low compared to c-Si due to the lack of long range order and increase defect density in the material. It was soon realized that the absorption of a-Si could be increased by the saturation of dangling bonds through atomic hydrogen [1.17]. This was done by the dilution of silane (SiH_4) gas with hydrogen (H_2) gas during plasma-enhanced chemical vapour deposition (PECVD) of a-Si. The alloying of a-Si with H_2 results in what is known as hydrogenated amorphous silicon (a-Si:H) [1.18]. The amount of hydrogen incorporated in the deposited thin film depends on the deposition process and the dilution ratio of precursor gas. H_2 incorporation has a large impact on the thin film properties and plays an important role in the passivation of defects in a-Si:H.

Hydrogen can be incorporated into a-Si:H as:

- i) Isolated Si-H bonds
- ii) A pair of hydrogen atoms interrupting a weak Si-Si bond (Si-H H-Si)
- iii) In the form of hydrogen clusters



Hydrogen incorporation as i) and ii) are considered useful for device quality devices, as it passivate dangling bonds in the amorphous network. The latter is considered harmful.

The effects of hydrogen dilution during deposition of a-Si:H results in some changes in the chemistry of the thin film growth surface. This enhances abstraction reactions of hydrogen and SiH_4 groups and etching of weak Si bonds, which results in denser films being produced. Furthermore, the gas phase reactions of the precursor gas leads to large radicals inhibited by the hydrogen dilution. This has a positive effect on the microstructure of the films and often results in a decrease of hydrogen content, with the increase in dilution [1.19]. The influence of hydrogen dilution on the optical band gap was observed to be a linear relationship [1.20]. At very high dilution percentages hydrogenated nanocrystalline silicon (nc-Si:H) can be formed.

In the visible range of the electromagnetic spectrum a-Si:H absorbs ~100 times more light than c-Si. Due to these distortion of the atomic structure in a:Si:H, the energies of the electronic states are perturbed, which results in a broadening of both the conduction band and valence band, and consequently a tailing of the band edges into the band gap. The density of these band tails decrease as it extends deeper into the band gap as seen in figure 1.3, depicting the c- and a-Si band structure [1.21]. Band tails introduce new trap states and recombination centres in the band gap which decreases the photoconductivity of the material. Though electrons and holes can by thermal excitation be re-emitted from these trap states.

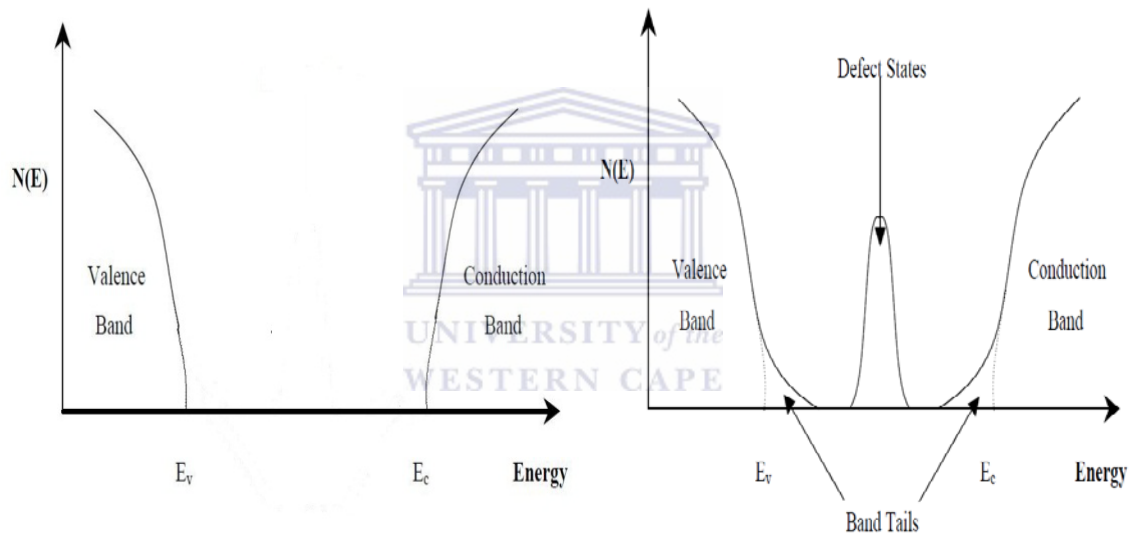


Figure 1.2 Distribution of densities of state in a) crystalline and b) amorphous silicon [1.22]

The band gap energy (E_g) refers to the energy difference between the lowest energy level of the conduction band (CB) and the highest energy level of the valence band (VB). For c-Si this E_g is ~1.2eV and for a-Si it is ~1.75eV [1.23]. Since a-Si:H has a direct band gap and therefore absorbs more light than its crystalline counterpart which has an indirect band gap [1.24].

1.2.2 Doping

Hydrogenated amorphous silicon material can be doped, by the addition of specific amounts of donor (n type) or acceptor (p type) impurities. Doping varies the electrical conductivity of the material to suit a specific need. The most common doping element used on a-Si:H for p-type doping is boron (B) and for n-type doping is phosphorus (P). In 1975, Spear and LeComber [1.25] first showed that a-Si:H could be doped by mixing silicon source gas; SiH₄, phosphine (PH₃) and diborane (B₂H₆) during PECVD [1.8]. The activation energy of the doped a-Si:H decreases drastically from 0.7 eV-0.8 eV to 0.15 eV with phosphorus doping and to 0.3 eV with boron doping. The doping efficiency was extremely low for a-Si:H, ranging from 0.01 – 1 %, depending on the deposition conditions employed. With c-Si, which has excellent long range order, the dopant atoms are required to assume the coordination of the atoms in the structured network. The continuous random network of a-Si:H, in contrast, does not enforced specific coordination, but the coordination of the dopant atoms can be predicted. This prediction was first brought forth Mott *et al.* [1.26] and is known as the “8 – N rule”. This rule states;

$$Z = 8 - N \text{ for } N \geq 4 \text{ and} \quad (1.1)$$

$$Z = N \text{ for } N < 4 \quad (1.2)$$

where Z is the coordination of an atom with N valence electrons.

Furthermore the Street *et al.* showed that doping of a-Si:H, increase the amount of dangling bonds, which leads to an increase in defect density which result in a shorter diffusion length for charge carriers. This is an undesired consequence to doping therefore an intrinsic layer was introduced to be sandwich between the p-n junctions to form a p-i-n junction [1.27].

1.2.3 Metastability: The Staebler-Wronski Effect

Amorphous silicon semiconductors do have a downfall, the light induced degradation effects that were first observed by D.L Staebler and C.R. Wronski in 1977 [1.29]. They observed that the dark-conductivity and photoconductivity was significantly reduced when exposed to prolonged illumination periods. This ultimately reduces the efficiency of the solar cell and is known as the Staebler-Wronski Effect (SWE). The origin of this effect still remains debatable, though experimentally it has been shown without a doubt that illumination of a-Si:H correlates to an increase in defect density of dangling bonds. The main factors that contribute to SWE are [1.30, 1.31]

- Disorder in the silicon network
- Bonding structure of hydrogen
- Concentration of hydrogen and impurities

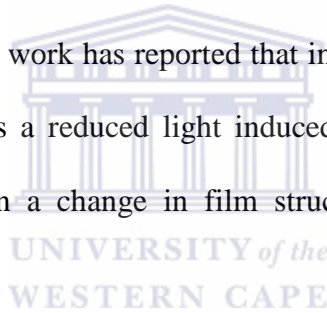
The defect density of a thin film has been shown by Stutzmann *et al.* [1.32], to be relates to the illumination intensity and the exposure time according to;

$$N_d(t) = AG^{\frac{2}{3}}t^{\frac{1}{3}} \quad (1.3)$$

The most favoured model for the origin of SWE is the hydrogen bond switching model. This model proposes that the non-radiative energy release from electron-hole recombination causes weak Si-Si bonds to break creating dangling bonds in the process. Hydrogen atoms then play a key role, as it moves through the network it can either create more dangling bonds by breaking weaker bonds or can prevent neighbouring atoms from recombining through passivation of their dangling bonds [1.28].

The SWE is not observed in high defect density material such as a-Si since its network is in such an extremely disordered state, recombination events are eliminated. The influence of impurities in the SWE has been disregarded since this effect was also observed in un-hydrogenated a-Si which indicates that it is an intrinsic effect of the material [1.33]. The changes that occur to the thin film as a result of the SWE were found to be reversible by annealing of the thin film at temperatures exceeding 150 °C. The annealing process results in the passivation of the newly created dangling bonds due to high temperatures. There is however, an equilibrium point that is reached after ~1000 hours of exposure to light. This equilibrium occurs when the amount of dangling bonds created is equal to the amount of passivation of dangling bonds [1.21].

The downfall of a-Si:H has led to the increase efforts to deposit a material that is more stable and less affected by the SWE. Recent work has reported that increasing dilution of SiH₄ with H₂ gas results in a film that experiences a reduced light induced degradation effect. The increase in hydrogen dilution also results in a change in film structure, leading to a more ordered Si network.



1.3 Nanocrystalline Silicon

A clear distinction can be made between a- and c-Si, by their atomic configurations. Nanocrystalline silicon (nc-Si) is commonly defined as a porous material consisting of two phases, amorphous and crystalline, with crystal sizes usually < 20 nm [1.34]. The crystallites present make the material more electrically stable and the ever present amorphous nature, results in the good absorption characteristics still being retained [1.35]. Due to its bi-phase nature when hydrogenated, nanocrystalline silicon (nc-Si) excels further by showing reduced degradation issues compared to a-Si:H and are used in tandem solar cells because of its tuneable band gap

and high photoluminescence stability [1.36, 1.37]. For these reasons the interest in nc-Si:H has been on an exponential increase over the past several years.

The transformation from a- to nc-Si:H is readily achieved through varying H₂ dilution during deposition of Si thin films. The effects of H₂ dilution during deposition of a-Si:H results in some changes in the chemistry of the thin film growth surface. Enhanced abstraction reactions of hydrogen and SiH₄ groups, and the etching of weak Si bonds occur. This has a positive effect on the thin film microstructure and often results in a decrease of hydrogen content, with the increase in H₂ dilution [1.38, 1.19]. Intuitively one would expect nanocrystalline material to have a band gap between that of an a- and c-Si thin film, though literature shows that for this material the band gap ranges between 1.9 – 2.1 eV [1.39]. This high band gap is considered to be a result of quantum size effects due to the presence of nanocrystals. The high band gap implies a low absorption from the thin film which could be due to a change in the density with the incorporation of nanocrystals. Many other researchers have a number of possible explanations for this, some of them being due to quantum confinement effects, improvement in short and medium range order and the presence of oxygen and nanocrystallites [1.39, 1.40].

1.3.1 Growth Models for silicon thin films

The nanocrystallites within nc-Si, hydrogenated or unhydrogenated, introduce ordered regions of silicon and grain boundaries into the structural nature of the thin film. Many exertions have been made to explain how nc-Si growth and the deposition parameter that affects it. There are three major models that can describe the growth of nc-Si, each to its own extent.

1.3.1.1 Selective Etching

The PECVD process for nc-Si films formation is the deposition method that led to the model of hydrogen radical etching. It has been strongly believed that the mechanism for PECVD grown

nc-Si films is a balance between film formation and etching [1.41-1.43] and is described by the reaction equation:



Under normal conditions this reaction is not in equilibrium and deposition only occurs once the reaction is balanced. Van Oort *et al.* later showed that the hydrogen radical etching model is insufficient to describe the growth of nc-Si films [1.44]. Fang *et al.* and Solomon *et al.* then offered a refined version of the etching model, called the selective etching model [1.43, 1.46]. A preferential etching of the amorphous matrix over the nanocrystalline material during the growth was observed. Furthermore, nc-Si:H also contained a higher fraction of voids, after the exposure to H₂. A change in the growth rate upon phase transformation from amorphous to crystalline was not seen in this model as predicted by the prior etching model. In the initial growth stage, silicon atoms will be adsorbed onto the substrate in all orientations. However, where atoms are arranged with a (112) plane surface, they will be more resistant to hydrogen radicals etching, which then forms a crystallite seed. More silicon atoms will bond to these seeds in the same orientation and crystallite growth forms with film thickness in a conical structure, resulting in a lateral expansion of the crystalline region with film thickness [1.47].

1.3.1.2 Chemical Annealing

It is generally known that nc-Si starts to grow with an initial amorphous layer, which slowly transformed into a crystalline structure during growth. This is the basis for the selective etching model. However, Abelson *et al.* [1.48] found evidence that the subsurface annealing model [1.49] used to describe a-Si:H growth can also describe nc-Si:H growth in DC sputtering experiments. The chemical annealing model clarified that both the surface and the subsurface volume of the film are in a liquid-like state [1.50]. This allows silicon atoms to reconfigure their bonds and change their sites. Exothermic reactions occurring at the surface of the growing thin

film increase the effective surface temperature. The rise in surface temperature provides sufficient energy to allow the silicon atoms to rearrange to an energetically, favourable crystalline structure. The transformation to nc-Si from within the bulk a-Si was then observed by ellipsometry and provided further support for the chemical annealing model [1.51].

1.3.1.3 Surface Diffusion

Surface diffusion model is another interpretation of the growth of nc-Si in CVD at lower temperatures ($< 400\text{ }^{\circ}\text{C}$) [1.52], which considers the strong dependence on substrate temperature and ion contribution. Surface diffusion is less active at lower temperatures, which results in the reduction in the formation of nc-Si nuclei. This is related to less diffusion of SiH_n radicals into stable sites. The SiH_n radicals are attached primarily to hydrogen on the surface. When the surface is covered less with hydrogen, at high substrate temperatures, less diffusion will occur, since the activation energy for thermal diffusion is increased and more reactions take place on the surface. When the number of hydrogen ions impinging the substrate surface exceeds a critical value the grain size decreases. A limitation within the model is the inability to explain why crystalline growth occurs at higher substrate temperatures when hydrogen is completely effused from the surface above $500\text{ }^{\circ}\text{C}$. Okada *et al.* performed diffusion experiments which suggest that hydrogen diffusion on the surface is irrelevant during crystalline growth [1.53].

The three major growth models for nc-Si films were developed from results obtained by different deposition techniques. Each model addresses some aspect of film growth extremely well but fails in another aspect. One could postulate that the growth is a combination of the growth models mentioned above occurring during film growth, as a possible model for the growth of nc-Si [1.54].

1.4 Application: Solar Cells

The first practical photovoltaic device, in which an efficiency of 2.4 % was achieved, was demonstrated using a-Si as a photovoltaic material. Thereafter, interest in silicon solar cells grew rapidly, prompted by its many possible applications.

Based on the photovoltaic effect a-Si:H is often used in solar cells and optical sensors, whereby exploiting the possibility of large area deposition. The following section will focus on the application of thin films in solar cells and its design. It should be noted that thin film silicon can have various applications ranging from solar cells and thin film transistors to light and chemical sensors and even electrostatic speakers.

1.4.1 Operating Principles

A solar cell is a device that converts light directly into electricity and works on the basis of the photoelectric effect. Its principle operation is to separate the photo-generated electron and holes to drive a current. This separation of charge is achieved through an internal electric field, via the creation of a p-n junction. Though recombination still occurs and is still an important energy loss factor in a solar cell, with the presence of the internal electric field, it is reduced. The current generated from this process is then passed through a circuit and utilised to power other electronic devices.

For an amorphous semiconductor, the high defect density of the p-type and n-type doped material, hinders the diffusion of the electrons and holes. This downfall led to the introduction of a new junction design in which an intrinsic layer is sandwiched between the p- and n-doped layers. The intrinsic layer aids in the collection of light and separation of charge in the circuit. This resulted in the, now more commonly known, p-i-n junction solar cell structure seen in figure 1.4.

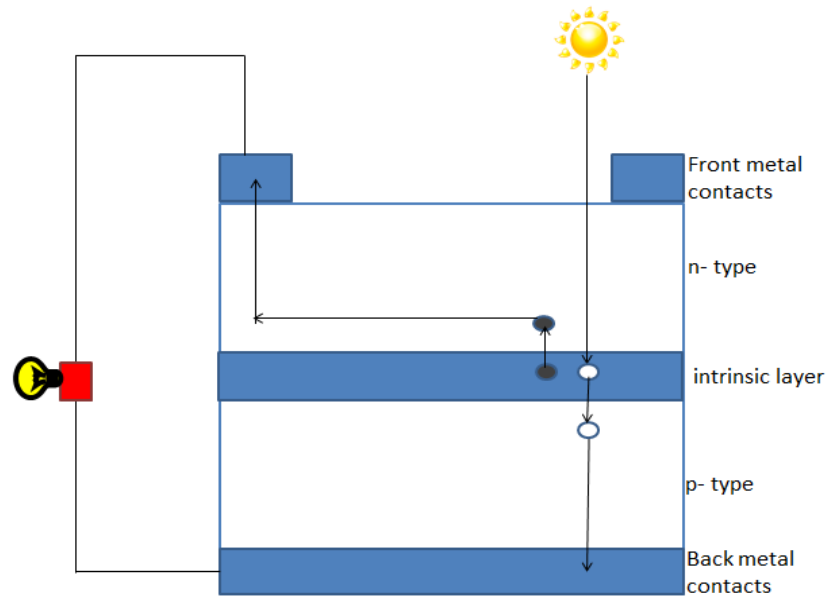


Figure 3.4 Superstrate configuration of basic operation of solar cell. The open circles represent holes and the close circle represents electrons. [1.56]

Light incident on the solar cell, with sufficient energy, will be used to generate an electron-hole pair. An electron-hole pair refers to the excitation of an electron in the intrinsic layer which results in the lingering of a hole. These charge carriers are inseparable and drive the photoelectric process. The excited electron diffuses toward the n-type layer, whilst the subsequent hole moves toward the p-type layer. Metal contacts then feed these carriers to an external circuit to generate electricity.

In the presence of the electric field, the drift length of the charge carriers are given by [1.55]

$$\lambda_{\text{mfp}} = \mu\tau E \quad (1.4)$$

This λ_{mfp} largely exceeds the thickness of a typical solar cell, ensuring that all the carriers which diffuse across are collected. The intrinsic layer thickness must however be smaller than the mean free path (mfp) of the slowest charge carrier, which are the holes generated. Furthermore, an

unnecessary increase in these layer thicknesses will result in a decrease in collection efficiency, due to photon absorption. The intrinsic layer should then be as thick as possible to absorb the maximum amount of photons [1.56, 1.57].

1.4.2 Single Junction solar cells

The single junction solar cell is most commonly used in the form of a transparent substrate design. This design consists of a glass substrate coated with a transparent electrode consisting of a transparent conductive oxide (TCO), usually indium-Tin Oxide (ITO). The TCO layer is followed by the p-type layer, whose role is to act as a window. After the p-type layer an intrinsic layer follows and thereafter the n-type layer and lastly a back metal contact as seen in figure 1.5.

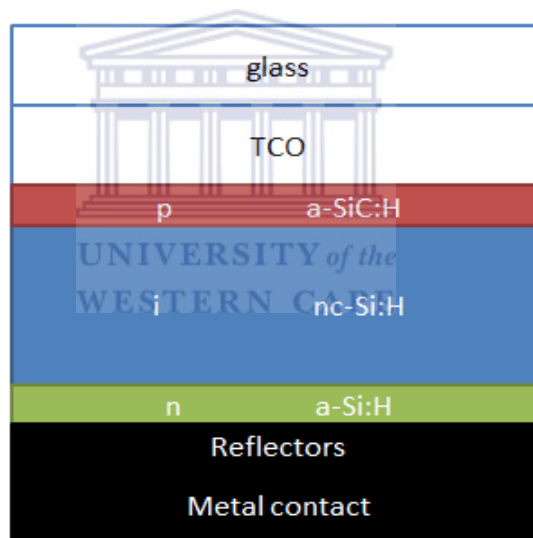


Figure 1.5 Schematic single junction solar cell – transparent substrate design

Each component has a role to play and specific task to execute. Texturing of the TCO surface is usually implemented as a means to reduce optical reflection and improve light scattering within the solar cell [1.58, 1.59]. TCO materials need to have a high band gap and transparency.

Light is required to pass through the TCO, and p-type layer to be absorbed in the i-layer.

Reduction in absorption in the p-type layer is achieved by using a hydrogenated amorphous

silicon carbide (a-SiC:H) alloy with a band gap of about 2 eV [1.60]. Absorption is mainly enhanced in the long wavelength region [1.61]. To further increase the percentage of light absorbed, back reflectors are added to allow the light that has been transversed by the active i-layer to be reflected back and given a second opportunity to be absorbed. Introducing a TCO layer between the n-layer and metal back contact further enhances the light trapping.

The two main factors of power loss in single junction solar cells are:

1. The restriction to absorbing only photons of energy equal to or of greater energy than the band gap and
2. The thermalisation effect due to absorbed photons of energy higher than the band gap.

1.4.3 Multi junction solar cells



A great deal of work has been done to increase the solar cell efficiency. The most effective of these advances has been the multi-junction solar cells. This device uses two or more p-i-n junctions, stacked on one another and connected in series.

The success with this device is due to the band gap of each junction which differs such that the junction with the highest energy gap is positioned first and the lowest energy gap is last. This allows light of higher energy to be absorbed in the junction above and the lower energy photons are transmitted and can be absorbed by the junctions below. This is known as spectrum splitting which results in a more effective absorption of the entire spectral range instead of just one energy range as in a single junction solar cell. Other benefits of the multi-junction solar cell are that the thickness of each junction is now less than that of a single junction therefore reducing the recombination losses. A schematic representation of spectrum splitting and the multi-junction solar cells design structure is displayed in figure 1.6.

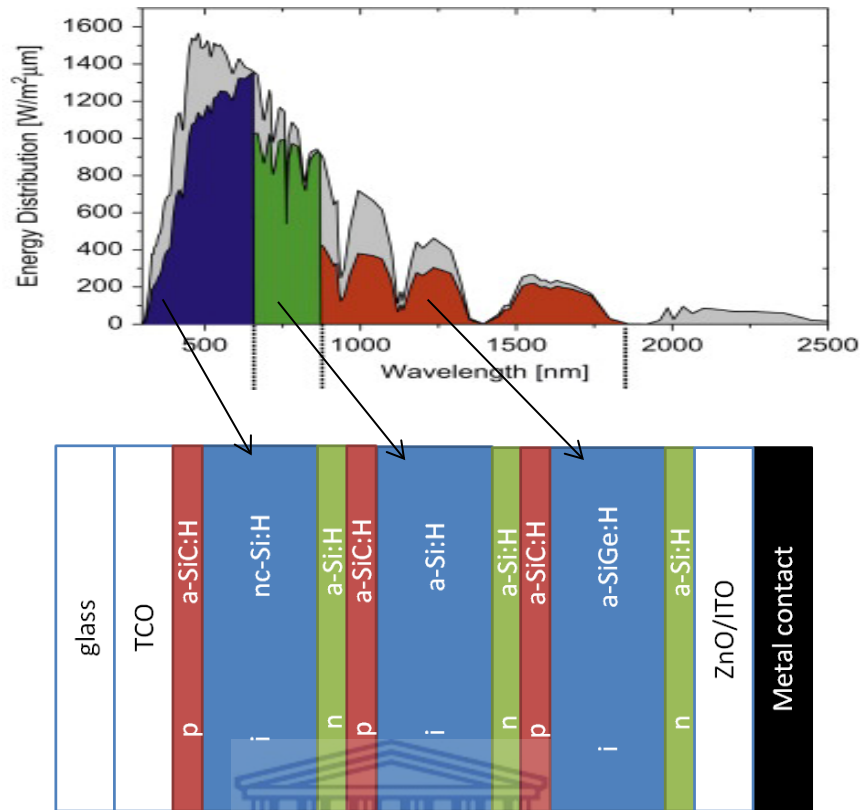


Figure 1.6 Schematic of a multi-junction solar cell [1.62]

A critical part in the structure of multi-junction solar cells is the n-p junction that divides the individual cells. At this point, electrons that are generated in the top cell flow to the n-p junction, where they should recombine with holes from the bottom cell. This recombination occurs via a tunnelling process, due to the high doping levels used for the layers involved. When the rate of recombination is not balanced with the supply of carriers, the electric field in the adjacent cell will be influenced negatively due to space charge accumulation [1.55]. Often one of the layers of the tunnel junction is microcrystalline [1.63]. Current matching also brings forth further hindrance for the optimization of multi-junction solar cells. The individual currents, must balance exactly; otherwise a loss in efficiency will occur [1.64]. If the currents are matched, then the quantum efficiency is constant over a wide range of wavelengths. If one of the cells limits the current, then the observed quantum efficiency will be that current-limiting cell.

1.5 Aims and Outlines

Current research has proven the potential of a-Si:H and nc-Si:H for solar cell applications. The latter (nc-Si:H) has recently found to be more stable under illumination and have low degradation effects, making it an ideal candidate for photovoltaic application and opto-electronic devices.

In this study we propose a new deposition procedure involving six sequential variations of the hydrogen gas flow rate, whilst the flow rate of silane remained constant, during deposition. The objective in this contribution is to eliminate the tunnelling issues at the junction between the two solar cells in a tandem structured solar cell by depositing a single intrinsic layer thin film which achieves structural and optical variation with depth. Prior to this attempt, an investigation is carried out into the characteristics of these specific deposition regimes. Each of the six gas flow rate variation steps are used to deposit separate thin films and investigated their individual properties. These results then serve as a stepping stone to understanding the effects of hydrogen dilution and the properties of the thin films produced during this dynamic deposition procedure.

The main methods of structural characterisation are high-resolution transmission and scanning electron microscopy, elastic recoil detection (ERD), X-ray diffraction (XRD), Raman spectroscopy and Fourier transform infra-red (FTIR) spectroscopy. The optical properties will be extracted from UV-VIS reflection spectra, using the effective medium approximation approach.

The thesis outline is as follow:

Chapter 1 gives an introduction and overview of the history and current state of research on second generation silicon thin films and its growth models by HWCVD.

Chapter 2 provides insight into the working and operation of HWCVD system used for this study

Chapter 3 describes the analytical techniques used to investigate the properties of the deposited thin films.

Chapter 4 focuses on the analysis and results of six separately deposited silicon thin films. Crystallinity, bond structure, hydrogen content, surface morphology and optical properties will be analysed by the techniques mentioned above.

Chapter 5 delves into the structural and optical characterisation of 2 dynamically deposited silicon thin films. Cross-sectional interrogation and surface analysis is revealed along with film crystallinity, bond structure, hydrogen content, and optical properties.

General concluding remarks will follow in the Summary.



References

- [1.1] S. Morgan (2009) *Alternative Energy Sources*. Heinemann Library.
- [1.2] I. Atkinson (2007) *Totu (Thoughts on the universe)* Lulu.com. p35-37.
- [1.3] International Energy Agency (2010) *Technology roadmap-solar photovoltaic energy*.
- [1.4] SolarGIS © 2013 GeoModel Solar s.r.o. <http://solargis.info/free-solar-maps>.
- [1.5] Joseph A. Angelo (2009) *Satellites: Frontiers in Space Series, Facts on File science library*. Infobase Publishing, ISBN:1438108958. p77-78.
- [1.6] R. Brendal (2011) *Thin-film crystalline silicon solar cells*. John Wiley & Sons. p4-7.
- [1.7] Prof Denish, Dr. V Shrivastava (2009) *Fundamentals of electronic devices, first edition*. Krishna Media Ltd. p229.
- [1.8] J. Poortmans, V. Arkhipov (2006) *Thin film solar cells: Fabrication, Characterization and Application*. John Wiley & Sons. p174-176.
- [1.9] D.E. Carlson, C.R. Wronski (1976) *Appl. Phys. Lett.* **28**, 671.
- [1.10] M.A.Green (2005) Third generation photovoltaics: advanced solar energy conversion. **12**, p1-3.
- [1.11] Mcconnell, R., & Fthenakis, V. (2011). Concentrated Photovoltaics.
- [1.12] Yella, A; Lee, HW; Tsao, HN; Yi, C; Chandiran, AK; Nazeeruddin, MK; Diau, EWD; Yeh, C-Y; Zakeeruddin, SM; Grätzel, M (2011) *Science*. **6056**, 629.
- [1.13] J. Meier, E. Vallat-sauvain, S. Dubail, U. Knoll, S. Dubail, S. Golay, A. Shah (2001) *Solar Energy Materials and Solar Cells*. **66**,73.
- [1.14] H. Hoppe and N. S. Sariciftci (2004) *Journal of Materials Research*. **19**,1924.
- [1.15] A.B.C. Lopez, A.M. Vega, A.L. Lopez. (2012) Next generation of photovoltaics: New concepts. **165**, p200-202.

- [1.16] C.J. Arendse (2004) *Thermal stability and structure of hot – wire deposited amorphous silicon*. PhD Thesis, South Africa: University of the Western Cape.
- [1.17] B. O'Regan, M. Grätzel (1991) *Nature*. **353**,737.
- [1.18] A. Shah (2010) *Thin film silicon solar cells*. Italy CRC Press. p17-19.
- [1.19] W Beyer (1999) *Introduction to Hydrogen in Semiconductors II*. **61**. Academic Press, San Diego.
- [1.20] W Beyer (1985) *Tetrahedrally Bonded Amorphous Semiconductors*. Plenum Press, New York. p129-146.
- [1.21] M.F. Thorpe, M.I. Mitkova (1997) *Amorphous insulators and semiconductors*. Kluwer academic publishers. p437-441.
- [1.22] R. Hull (1999) *Properties of crystalline silicon*, Short Run Press Ltd. 90-95 pages.
- [1.23] I. Yang, I.F. Chen (1994) *Mater.Res.Proc.* **336**,669.
- [1.24] R. Dewan, S. Fischer, V.B. Meyer-rochow, S. Hamraz, & D. Knipp (2012) *IOP Science*. **7**,016003.
- [1.25] N. Spear and P. LeComber (1975) *Solid state Comm.* **17**, 1193.
- [1.26] N. F. Mott (1969) *Philos. Mag.* **19**, 835.
- [1.27] R.A. Street (1987) *Journal of Applied Physics*. **66**,1367.
- [1.28] S. Halindintwali (2005). *A study of hydrogenated nanocrystalline silicon thin films deposited by hot wire chemical vapour deposition (HWCVD)*. *Thin Films* (September).PhD thesis. South Africa: University of the Western Cape.
- [1.29] D.L.Staebler, C.R. Wronski (1977) *Appl. Phys. Lett.* **31**,292.
- [1.30] R.E.I. Schropp, M Zeman (1998) *Amorphous and microcrystalline silicon solar cells:modelling, materials and device technology*. Springer. p3-55.
- [1.31] K. Winer (1990) *Phys. Rev. B*. **41**,12150.

- [1.32] M. Stutzmann (1992) *Amorphous and microcrystalline semiconductor devices: Materials and device physics*. Artech House Norwood. p129.
- [1.33] T. Kamei, N. Hata, A. Matsuda, T. Uchiyama, S. Amano, K. Tsukamoto, Y. Yoshioka and T. Hirao (1996) *Appl. Phys. Lett.* **68**, 2380.
- [1.34] J. Nelson (2003) *The Physics of Solar Cells*. Imperial College Press, ISBN: 9781860943492.
- [1.35] L. M Fraas, L.D Partain (2010) *Solar Cells and Their Applications*. John Wiley & Sons. ISBN: 9780470446331.
- [1.36] V. Shah, J. Meier, E. Vallat-Sauvain, N. Wyrsh, U. Kroll, C. Droz, U. Graf (2003) *Sol. Energy Mater. Sol. Cells.* **78**, 469.
- [1.37] R. Saleh, N.H. Nickel (2003) *Thin Solid Films* 427, 266.
- [1.38] R.E.I. Schropp, H. Li, R.H. Franken, J.K. Rath, C.H.M. van der Werf, J.W.A. Schüttauf, R.L. Stolk (2008) *Thin Solid Films.* 516, 6818.
- [1.39] K.L. Chopra. P.D. Paulsen, V. Dutta (2004) *Thin film solar cells: an overview, Progress in photovoltaics: Research and application.* **12**, p69-92.
- [1.40] J. Poortmans, V. Arkhipov (2006). *Thin film solar cells fabrication, characterization and application*. John Wiley & Sons Ltd. Pages 175-196.
- [1.41] N. Layadi, P. Roca, I Cabarrocas, B. Drévillon and I. Solomon (1995) *Phys. Rev.B.***52**, 5136.
- [1.42] C.C. Tsai, Thompson, C. Doland, F.A. Ponce, G.B. Anderson and B. Wacker (1988) *Mater. Res. Soc. Symp. Proc.* **118**.
- [1.43] S. Veprek (1981) *Chimia* **34**, 489.
- [1.44] R.C. van Oort, M.J. Geerts, J.C. van den Heuvel and J.W. Metselaar (1987) *Electron. Lett.* **23**, 969.
- [1.45] M. Fang, J.B. Chevrier and B. Drevillon (1991) *J. Non-Cryst. Solids.* 791, 137.

- [1.46] I. Solomon, B. Drevillon, H. Shirai and N. Layadi (1996) *J. Non-Cryst. Solids.* 989, 166.
- [1.47] M. Heintze, W. Westlake and P.V. Santos (1993) *J. Non-Cryst. Solids.* 985, 164.
- [1.48] J.R. Abelson, N. Maley, J.R. Doyle, G.F. Feng, M. Fitzner, M. Katiyar, L. Mandrell, A.M. Myers, A. Nuruddin, D.N. Ruzic and S. Yang (1991) *Mat. Res. Soc. Symp. Proc.* **219**.
- [1.49] A. Gallagher and J. Scott (1987) *Sol. Cells.* **21**, 147.
- [1.50] Y.H. Yang, M. Katiyar, G.F. Feng, N. Maley and J.R. Abelson (1994) *Appl. Phys. Lett.* **65**, 1769.
- [1.51] T. Akasaka and I. Shimizu (1995) *Appl. Phys. Lett.* **66**, 3441.
- [1.52] A. Matsuda (1983) *J. Non-Cryst. Solids.* **59**, 767.
- [1.53] Y. Okada, J. Chen, H. Campbell, P.M. Fauchet and S. Wagner (1990) *J. Appl. Phys.* **67**, 1757.
- [1.54] M. Luysenberg, P. Hapke, R. Carius and F. Finger (1997) *Phil. Mag. A.* **75**, 31.
- [1.55] M. Hack and M. Shur (1985) *J. Appl. Phys.* 58, 997.
- [1.56] R. E. I. Schropp and M. Zeman (1998) *Amorphous and Microcrystalline Silicon Solar Cells Modeling, Materials and Device Technology.* Kluwer Academic Publishers, Boston, U.S.A.
- [1.57] A. Catalano (1991) *Amorphous and Microcrystalline Semiconductor Devices; Optoelectronic devices*, edited by J. Kanicki. Artech House, Norwood, U.S.A. Chap. 2, p9.
- [1.58] E. Yablonovitch and G. D. Cody (1982) *IEEE Trans. Elec. Dev.* **29**, 300.
- [1.59] H. W. Deckman, C. R. Wronski, H. Witzke, and E. Yablonovitch (1983) *Appl. Phys. Lett.* 42, 968.
- [1.60] Y. Tawada, H. Okamoto, and Y. Hamakawa (1981) *Appl. Phys. Lett.* 39, 237.

- [1.61] C. Beneking, B. Rech, T. Eickho_, Y. G. Michael, N. Schultz, and H. Wagner (1994) *Proceedings of the Twelfth E.C. Photovoltaic Solar Energy Conference, Amsterdam, the Netherlands*. edited by R. Hill, W. Palz, and P. Helm. H.S. Stephens & Associates, Bedford, U.K. p683.
- [1.62] Adrian Kitai (2011) *Principles of Solar Cells, LEDs and Diodes: The Role of the PN Junction illustrated edition*. **30**, John Wiley & Sons. ISBN: 1444318349.
- [1.63] J. K. Rath, R. E. I. Schropp, and W. Beyer (1998) *J. Non-Cryst. Solids*. 1282, 227.
- [1.64] J. Bruns, M. Choudhury, and H. G. Wagemann (1995) *Proceedings of the Thirteenth European Photovoltaic Solar Energy Conference, Nice, France*. edited by W. Freiesleben, W. Palz, H. A. Ossenbrink, and P. Helm. H.S. Stephens & Associates, Bedford, U.K. p230.



CHAPTER TWO

HOT-WIRE CHEMICAL VAPOUR DEPOSITION

2.1 Introduction

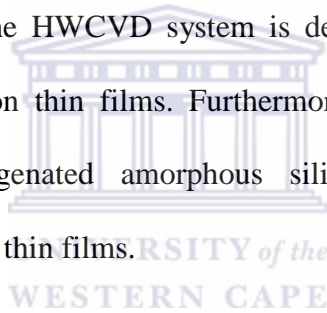
Silicon thin films can be grown in a number of different methods, which are usually some variant form of chemical vapour deposition techniques (CVD). The most commonly used CVD techniques for thin film deposition are plasma-enhanced CVD (PECVD) and hot-wire CVD (HWCVD). Weismann *et al.* first deposited hydrogenated amorphous silicon (a-Si:H) using silane (SiH_4) and a hot tungsten filament in 1979 [2.1] using HWCVD. At this stage this method did not attract many researchers, as the quality of thin film was poor. In 1986 Matsumura *et al.* deposited a-Si:H using HWCVD and obtained film properties similar to those obtained by PECVD [2.2]. Soon thereafter device quality silicon thin films was reported by Mahan *et al.* [2.3], which required lower hydrogen content to obtain lower density of states and void density than that compared to PECVD.

PECVD involves the gas phase reactions of a silicon containing gas by maintaining a gas discharge. These gas phase reactions result in the formation of neutral radicals, positive and negative ions, electrons and molecules. With HWCVD there is no ion production, as the

silicon containing gas is dissociated catalytically by the heated filament and thus the growing film does not suffer from ion bombardment as it would in PECVD.

The HWCVD process is ideal for the demand of industries seeking a passivation material for applications that are sensitive to defect creation by energetic ions. It involves the flow of precursor gases into a chamber that contains a heated filament and a substrate. Chemical reactions take place on and near the heated filament and result in the dissociation of the precursor gas into unique radicals. These radicals diffuse toward the substrate, located a few centimetres below the filament, and undergo secondary gas phase reactions. This results in the growth and nucleation of the molecules, dissociated at the filament and from the gas phase reactions, onto a substrate.

In this chapter the design of the HWCVD system is described, including the gas supply system, for deposition of silicon thin films. Furthermore, the chapter will report on the growth mechanism of hydrogenated amorphous silicon (a-Si:H) and hydrogenated nanocrystalline silicon (nc-Si:H) thin films.



2.2 Hot-wire chemical vapour deposition system

The MVSYSTSTEMS HWCVD system [2.4 – 2.5] under inspection in this chapter is set up at the University of the Western Cape. This system is ideal for cost effective deposition of high quality thin film semiconductor materials.

The deposition occurs within an ultra-high vacuum reaction chamber that has the capability to achieve a pressure of 10^{-7} Pa. The reaction chamber is made of a welded 304 stainless steel, along with CF flanges and copper gaskets, which connect the pumps, heater well, gate valve, gas supply, exhausts, view ports and instrumentation.

A 125 W substrate heater is mounted to the well on the top flange of the system. A type K thermocouple, belonging to a panel mounted controller, is attached to the bottom of the heater well. This controls the temperature of the substrate which is set by the user. Furthermore a stainless steel backing plate is utilised to achieve a homogeneous substrate temperature.

A shutter is used as substrate protection, which can be manoeuvred in and out the chamber, until the wanted deposition conditions are reached. The shutter is also used to control deposition exposure time. The motion of the shutter is controlled by sliding magnet manipulators between the inner and outer magnet stops. Several tantalum (Ta) filaments are woven in a parallel fashion and are supported on a removable base plate. An alternating current (AC) power supply is used to heat the filament. The filament temperatures are measured using a Raytek Marathon Series™ MRS1 two colour pyrometer. The base plate includes a power feedthrough and a type K thermocouple for reference. The filaments are separated 15 mm apart, of diameter amounting to 0.25 mm and situated a distance of 18 mm from the substrate holder. An image of the actual system along with a graphical representation on the system setup can be seen in figure 2.1 and 2.2 respectively.



Figure 2.1 MVSYTSEMS HWCVD system at the University of the Western Cape

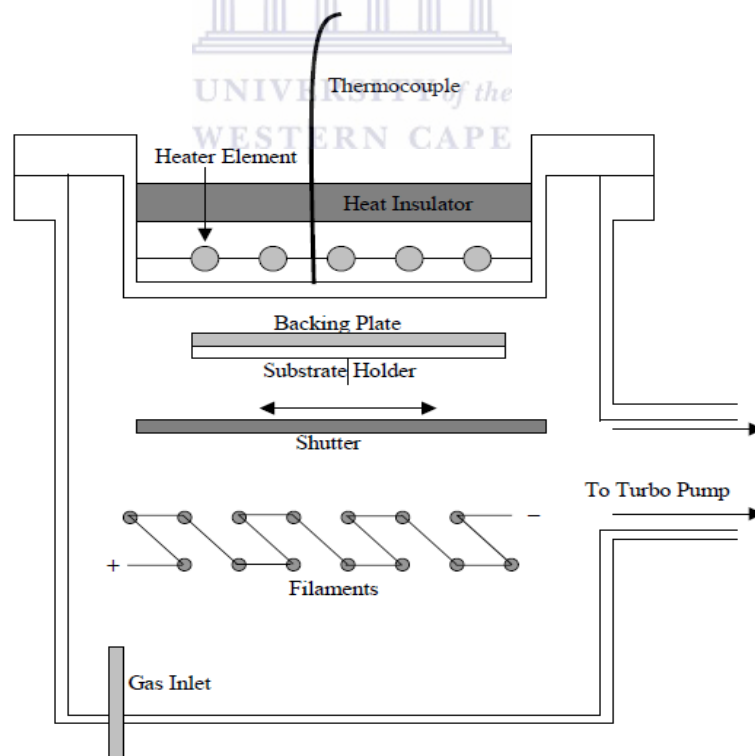


Figure 2.2 Cross-sectional view of the HWCVD reaction chamber [2.5].

2.3 Gas supply system

The gas supply system consists of a gas supply, exhaust, solenoid valves, manual valves and mass flow controllers. Figure 2.3 shows a schematic of the gas inlet system to the reaction chamber. Numerous gases can be supplied to the reaction chamber, labelled in figure 2.2.

A Matherson pressure regulator connects the gas supply unit to the different gas cylinders. The gas flow is controlled by the mass flow controller as it travels toward the reaction chamber and out via the exhaust. The high vacuum pneumatic valves are controlled from a separate, elevated, set of solenoid air pressure valves. These valves control the gas line connection to the reaction chamber. The exhausts are pumped with a Leybold Trivac B rotary-vane pump, which pumps at a speed of 40 m³/h.

Argon (Ar) and Nitrogen (N₂) are the purge gases used in the gas line and reaction chamber, before and after each deposition run and when a gas cylinder is changed.

The MVHWCVD system can deposit both doped and undoped thin films. To deposit undoped, pure and diluted, a-Si:H films, SiH₄ and H₂ is used. Phosphine (PH₃) and Diborine (B₂H₆) are used for n – and p- type doping respectively. A maximum flow rate of 100 sccm can be achieved by the mass flow controllers, for all gases except PH₃ and B₂H₆, which has a maximum flow rate of 10 sccm.

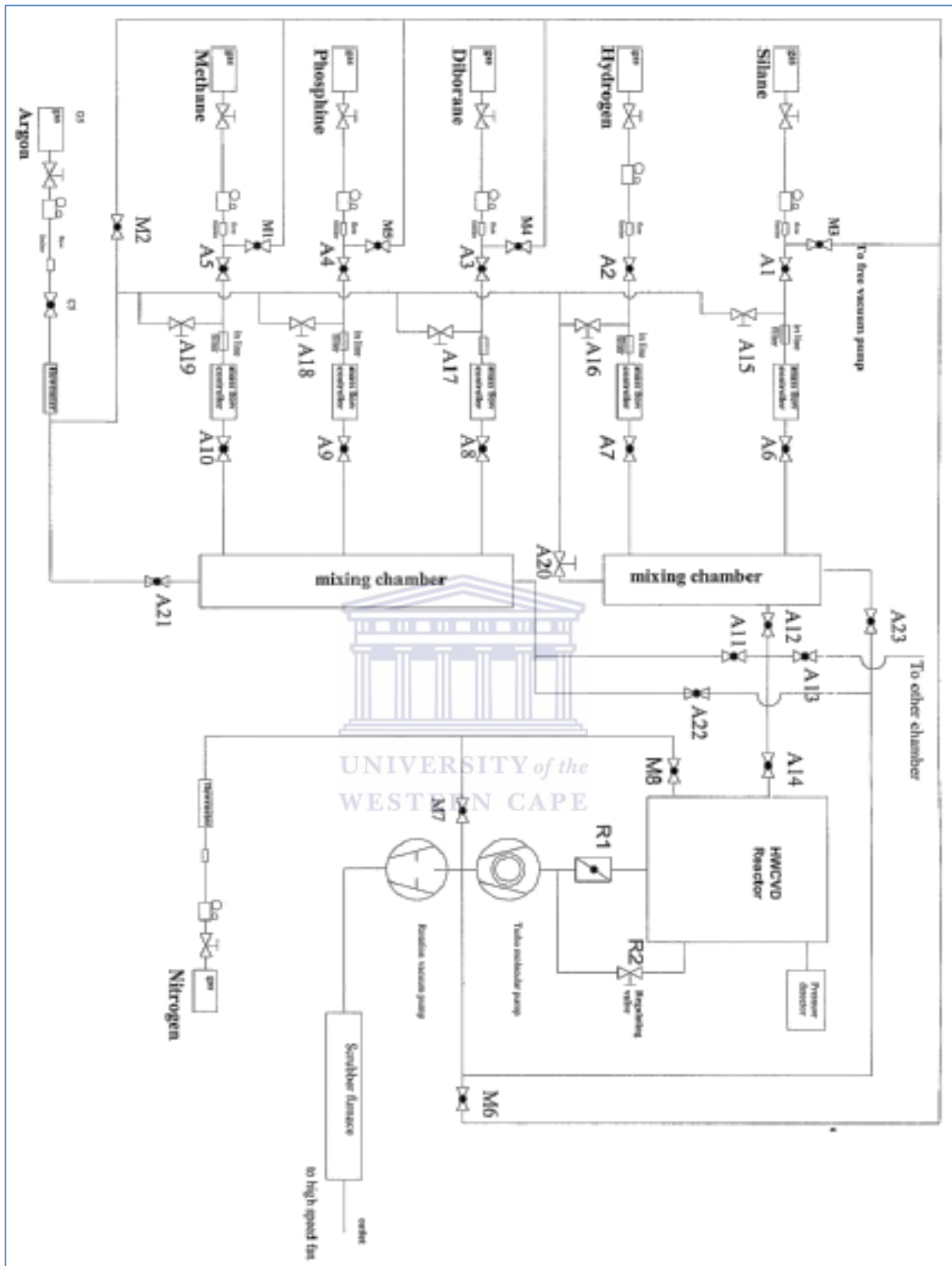


Figure 2.3 Representative diagram of gas inlet system [2.5]

2.4 Growth mechanism for a-Si:H and nc-Si:H

The growth of silicon thin films is largely studied by mass spectroscopy in an attempt to understand the reaction kinetics, the radicals that dominate film growth and parametrical effects on the deposition. Though this process is complex and vary somewhat in different studies, the growth mechanism for silicon thin films deposited by HWCVD can be categorized into three general stages.

2.4.1) Dissociation at the filament

2.4.2) Secondary gas phase reaction

2.4.3) Film growth

The explanation for each category might alter to an extent for growth of different thin films, though the overall process remains the same. In this section a detailed exploration into these categorized is taken.

2.4.1 Dissociation at the filament

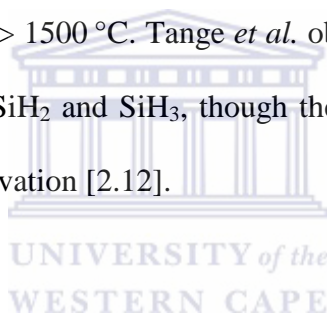
The temperature of a filament will govern the dissociation of molecules and the radicals produced from the catalytic dissociation. In 1988 J. Doyle [2.6] reported that at a filament temperature (T_f) of ~ 1800 °C the decomposition of SiH_4 gas results mostly into atomic hydrogen (H) and Si atoms. This research also revealed a linear relationship between the film growth rate and decomposition efficiency. Tonokura *et al.* [2.7] studied the dissociation of SiH_4 on the surface of a hot tungsten filament and confirmed the results of Doyle *et al.* The catalytic dissociation reactions on the filament surface revealed by Heintze *et al.* [2.8] indicate that for $T_f > 1500$ °C the main decomposition reactions taking place are;



Brogueira *et al.* [2.9] claimed another significant dissociation reaction occurs at the surface of the filament;



Mass spectrometry has played a vital role in the detection of radicals dissociated by the filament. Doyle *et al.* reported large detection of H, Si and SiH₃ whereas Holt *et al.* reported SiH₂ as the dominant radical. With the introduction of hydrogen gas (H₂) to dilute the SiH₄, it is dissociated by the filament into atomic hydrogen as has been observed in many studies [2.10]. Starobinski *et al.* [2.11] showed that H₂ is completely dissociated at pressures of $5 \times 10^{-3} - 1 \times 10^{-2}$ mbar with a $T_f > 1500$ °C. Tange *et al.* observed that the H₂ dilution did not vary the signal intensity of Si, SiH₂ and SiH₃, though the low percentage of dilution could have been a reason for this observation [2.12].



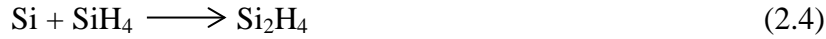
2.4.2 Gas phase reactions

Of the H and Si atoms formed by catalytic dissociation of SiH₄ and H₂, some of these atoms meet the film substrate without undergoing further reaction on its path to the substrate. The others will part take in secondary gas phase reactions on its way to the substrate. Typical gas phase reaction species can be seen in table 2.1 below.

Table 2.1 Gas phase reaction species in HWCVD [2.13].

Reactions	
$H + SiH_4$	$\longrightarrow SiH_3 + H_2$
$H + SiH_3$	$\longrightarrow SiH_2 + H_2$
$SiH_3 + SiH_3$	$\longrightarrow SiH_2 + SiH_4$
$Si + SiH_4$	$\longrightarrow Si_2H_2 + H_2$
	$\longrightarrow Si(H_2) Si + H_2$
$Si + SiH_4$	$\longrightarrow Si_2H_2 + H_2$
	$\longrightarrow Si(H_2) Si + H_2$
$Si_2H_2 + SiH_4$	$\longrightarrow Si_3H_4 + H_2$

In HWCVD the filament-substrate distance and the process pressure are significant factors that affect the degree to which the secondary reactions occur. O'Hanlon *et al.* identified the transition from a low secondary reaction regime to a high secondary reaction regime as a product of factors mentioned above. These secondary reactions are presumed to take place between the filament and the substrate [2.14]. Furthermore, at low pressures, the molecules produced by the dissociation at the filament are more likely to diffuse toward the substrate without further interaction on its path. Although at high pressures (> 0.1 mbar) a large number of secondary reactions take place, as the Si atoms diffusing from the filament become highly reactive at high pressures. Abstraction and insertion reactions are the dominant reactions occurring during secondary gas phase regime [2.15]. Atomic hydrogen plays a role in the abstraction of hydrogen from SiH₄ to forms SiH, SiH₃, SiH₂ and H₂. The dominant insertion reaction is experimentally believed to be;



The greater the distance between the filament and substrate the higher the probability of a secondary reaction occurring depending on the process pressure. These factors can be set based on the desired thin film properties for a particular application.

2.4.3 Film growth

The radicals produced by the secondary reaction and those that diffusing from the filament without secondary interactions now reach the substrate surface. Depending on the sticking coefficient of the radicals produced, they will attach themselves to the substrate surface [2.16]. The flux of radicals at the surface of the substrate, interact with the growing thin film layer via the diffusion of radicals and atoms into sub-layers of the film. The passivation of dangling bonds and the etching away of weaker bonds on the surface of the thin film occur as a result of surface interaction of hydrogen atoms [2.17]. The reactions occurring at the surface of the growing silicon thin film have been investigated by Molenbroek *et al.* and are given in the table below;

Table 2.2 Reactions of Si, H and SiH₃ on the surface of thin films (s refers to radicals bonded to Si atoms in the film) [2.18]

Reactions	
$\text{Si} + \text{SiH}_s$	$\longrightarrow \text{SiSiH}_s = \text{SiH}_s + 2 \text{ dangling bonds}$
$\text{H} + \text{SiH}_s$	$\longrightarrow \text{H}_2 + \text{dangling bonds}$
$\text{SiH}_3 + \text{dangling bond}$	$\longrightarrow \text{SiH}_{3s}$
$\text{H} + \text{dangling bond}$	$\longrightarrow \text{SiH}_s$
$\text{Si} + \text{dangling bond}$	$\longrightarrow \text{Si}_s + 3 \text{ dangling bonds}$

Molenbroek *et al.* also showed that Si atoms, desorbed from the filament, were a major cause in the reduction of device quality of thin films [2.18].

With the addition of H₂ dilution, the increase of atomic hydrogen is observed, allowing for the above mentioned reactions to take place. The abstraction of a hydrogen atom from SiH₄ also occurs more readily with H₂ dilution. The excellent etching properties of atomic hydrogen results in the recrystallization of the silicon thin film. Maroudas *et al.* established that hydrogen atoms rearrange the atoms in a-Si:H into the lattice structure found in nc-Si:H. It is proposed that the hydrogen get trapped between loosely bound atoms in a-Si to establish a Si-H-Si configuration of higher energy [2.19]. When these trapped hydrogen atoms are released, through diffusion or etching, the Si atoms are thought to be left in an ordered array.

The benefits of H₂ dilution concluded by many researchers are [2.20];

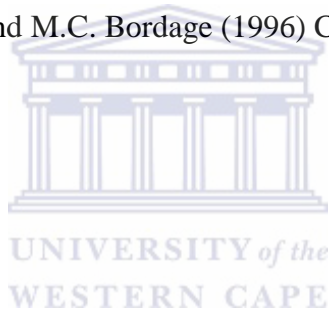
- Increase in surface passivation which provides a more homogeneous film growth
- Increase in abstraction thus more SiH₃ which is good for a-Si film growth
- Etching effect of atomic hydrogen, to remove weak Si-Si bonds

The key radical in the film growth of a-Si:H by PECVD are found to be SiH₃, H and Si. The principle radicals for film growth via HWCVD are H, SiH₃, SiH₂, Si₂H₂ [2.21].

References

- [2.1] H. Wiesmann, A. K. Ghosh, T. McMahon and M. Strongin (1979) *J. Appl. Phys.* 50, 3752.
- [2.2] H. Matsumura (1986) *Jpn. J. Appl. Phys.* 25, L949.
- [2.3] A. H. Mahan, J. Carapella, B. P. Nelson, R. S. Crandall and I. Balberg (1991) *J. Appl. Phys.* 69, 6728.
- [2.4] MVSystems Inc. (1997) "Operating Manual for the Hot-Wire CVD System, Version 1.0", Physics Department, University of the Western Cape, Bellville, South Africa.
- [2.5] C. J. Arendse (1999) "*Hydrogenated Amorphous Silicon: Optical Properties and Hydrogen Concentration*", M.Sc. thesis, University of the Western Cape, Bellville, South Africa.
- [2.6] J. Doyle, R. Robertson, G. H. Lin, M. Z. He, A. Gallagher (1988) *J. Appl. Phys.* 64, 3215.
- [2.7] K. Tonokura and M. Koshi (2002) *Current Opinion Sol. State Mat. Sci.* 6, 5, 479.
- [2.8] M. Heintze, R. Zedlitz, H. N. Wanka, M. B. Schubert (1996) *J. Appl. Phys.* 79, 2699.
- [2.9] P. Brogueira, J. P. Conde, S. Arekat, V. Chu (1996) *J. Appl. Phys.* 79, 8748.
- [2.10] H. Matsumura (1998) *Jpn. J. Appl. Phys.* 1, 37(6A), 3175.
- [2.11] L. Starobinski, R. Dus (1995) *Vacuum.* 46, 433.
- [2.12] S. Tange, K. Inoue, K. Tonokura, M. Koshi, (2001) *Thin Solid Films* 395, 42.
- [2.13] J. Perrin, O. Leroy and M. C. Brodage (1996) *Contrib. Plasma Phys.* 363.
- [2.14] J.F. O'Hanlon (1989) *A User's Guide to Vacuum Technology.* Wiley, New York.

- [2.15] R.E.I. Schropp, M Zeman (1998) *Amorphous and microcrystalline silicon solar cells: modelling, materials and device technology*, Kluwer Academy, Dordrecht p3-55.
- [2.16] C. Horbach, W. Beyer, H. Wagner (1991) *J. Non-Cryst. Solids.* 661, p137–138.
- [2.17] W. Zheng, & A. Gallagher (2008) *Thin Solid Films.* 516, 6, p929-939.
- [2.18] E. C. Molenbroek, A. H.Mahan and A. Gallagher (1997) *J. Appl. Phys.* 821909.
- [2.19] D. Maroudas, S. Agarwal, E. S. Aydil and S. Sriraman (2002) *Nature.* 418, p62-65.
- [2.20] K. F. Feenstra (1998) *Hot-wire chemical vapour deposition of amorphous silicon and the application in solar cells*, Ph.D. thesis, Utrecht University.
- [2.21] J. Perrin, O. Leroy and M.C. Bordage (1996) *Contrib. Plasma Phys.* 36, 3.



CHAPTER THREE

ANALYTICAL METHODS

3.1 Introduction

This chapter will discuss the theoretical background and experimental setup for the various analysis techniques that have been employed to investigate the thin film samples. The techniques used are given in the table below:

Table 3.1 Characterization techniques the type of information obtained

Experimental technique	Information
UV-Visible Spectroscopy	Determine optical properties such as refractive index, absorption coefficient and optical band gap
X-ray Diffraction	Crystallinity of the samples
Raman Spectroscopy	Short range order and crystallinity
Fourier Transform Infra-red Spectroscopy	Bonding configuration, bonded hydrogen content
Electron Recoil Detection Analysis	Total hydrogen concentration
Atomic Force Microscopy	Surface morphology and roughness
Transmission Electron Microscopy	Cross sectional analysis, structural and elemental information and imaging
Scanning Electron Microscopy	Surface imaging analysis, elemental composition, structural information

3.2 Ultraviolet -Visible Spectroscopy

3.2.1 Introduction

UV-Visible spectroscopy is an essential, non-destructive technique used to determine optical properties of a thin film. Thickness, optical band gap, refractive index and absorption coefficient are the key optical properties investigated. These properties can be determined using either reflected or transmitted light from and through a target sample respectively. For this study we will rely on reflectance measurements to obtain optical characterization of the samples.

3.2.2 Theory

For solar cell application the absorption coefficient is a vital characteristic of an a-Si:H thin film. The optical absorption merely pertains to the probability of absorbing a photon and transferring that photon energy to an electron. For an intrinsic layer this becomes important as it directly relates to the amount of energy produced by the solar cell.

Thus understanding light's interaction with matter becomes pertinent to determining the optical parameters. If an ideal thin film is assumed, which is isotropic and is homogeneously deposited on a thick absorbing substrate such as crystalline silicon (c-Si) and immersed in air, the optical reflectance is given by ;

$$R = \frac{A+Bx+Cx^2}{D+Ex+Fx^2} \quad (3.1)$$

Where $x = e^{-\alpha d}$ is the absorbance, $\Phi = (4\pi n_1 d)/\lambda$ and $\alpha = (4\pi k_1)/\lambda$ is the absorption coefficient,

$$A = [(1 - n_1)^2 + k_1^2][(n_1 + n_2)^2 + (k_1 + k_2)^2] \quad (3.2)$$

$$C = [(1 + n_1)^2 + k_1^2][(n_1 - n_2)^2 + (k_1 - k_2)^2] \quad (3.3)$$

$$D = A, F = C$$

$$B = 2[A' \cos \Phi + B' \sin \Phi] \quad (3.4)$$

$$E = 2[C' \cos \Phi + D' \sin \Phi] \quad (3.5)$$

$$A' = C' = (1 - n_1^2 - k_1^2)(n_1^2 - n_2^2 + k_1^2 - k_2^2) + 4k_1(n_1k_2 - n_2k_1) \quad (3.6)$$

$$B' = D' = 2(1 - n_1^2 - k_1^2)(n_1k_2 - n_2k_1) - 2k_1(n_1^2 - n_2^2 + k_1^2 - k_2^2) \quad (3.7)$$

Based on the assumption an ideal film with average thickness, d , will be characterized by its complex refractive index [3.1]

$$n_1 = n_1 - ik_1 \quad (3.8)$$

$$n_2 = n_2 - ik_2 \quad (3.9)$$

Using equation 2.1 above, the optical constants can be obtained from the non-linear equation;

$$R(\lambda_i, n_1, k_1, d) - R_{\text{exp}} = 0 \quad (3.10)$$

A typical curve for the absorption coefficient as a function of energy (Figure 3.1) can be segregated into three regions, A, B and C [3.2]. For this study, attention will be paid to region B which is present in the absorption coefficient curve due to the transitions between the conduction band, valence band and band tails.

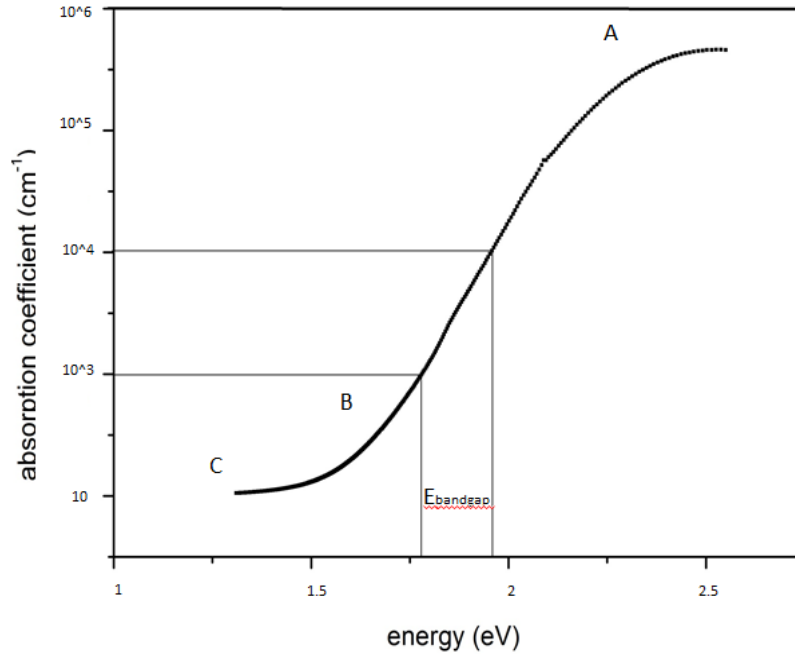


Figure 3.1 Typical absorption coefficient curve as a function of photon energy [3.2]

With the transition of an electron from the conduction band to the valence band and assuming the density of states of both bands are constant, the absorption coefficient is given by;

$$\alpha(E) = C_1 e^{\frac{E-E_g}{E_v^0}} + C_2 e^{\frac{E-E_g}{E_c^0}} \quad (3.11)$$

Where E_g is the optical band gap and E refers to a particular energy level. The terms E_v^0 and E_c^0 are the energy constants characterizing the exponential functions of the density of states for the conduction and valence band tails.

Furthermore figure 3.1 can be used to obtain a good estimate of the optical band gap (E_g). Setting the absorption coefficient at a certain value, $\alpha = 10^3$ or 10^4 cm^{-1} , and determine the corresponding energy. An improved method of determining an estimate for the optical band gap is via extrapolation of the α versus energy plot. The most common extrapolation procedure was introduced by Tauc [3.3] given by the equation below, which is based on the assumption that the density of state follows a parabolic function.

$$(\alpha\hbar\nu)^{\frac{1}{2}} = B (\hbar\nu - E_g) \quad (3.12)$$

Klazes *et al* [3.4] proposed a similar relation (cubic), assuming a linear density of state function

$$(\alpha\hbar\nu)^{\frac{1}{3}} = B' (\hbar\nu - E_g) \quad (3.13)$$

The cubic E_g value is usually ~0.2 eV lower than the Tauc prediction. In this work we will use the Tauc convention.

The thickness of the film is determined by an iterative procedure. The refractive index at zero energy n_0 is determined through the extrapolation of $1/[n^2(E)-1]$ versus E^2 to $E = 0$.

3.2.3 Experimental Setup

Reflection measurements of thin films deposited on single crystalline silicon were performed using a Semiconsoft mProbe UV-Visible photo-spectrometer F4 with a Si 3600 pixel detector and a tungsten-halogen light source. When the beam comes into contact with the sample it can either be reflected, transmitted, diffuse, absorbed or refracted, depending on the angle of incidence of the beam with respect to the sample surface as shown in figure 3.2. For this measurement the setup was adjusted to detect specular reflected photons only. Using a monochromatic light in a spectral range of 200 – 1000 nm, with a 1 nm spectral resolution, light is reflected from the sample surface is captured by the detector.

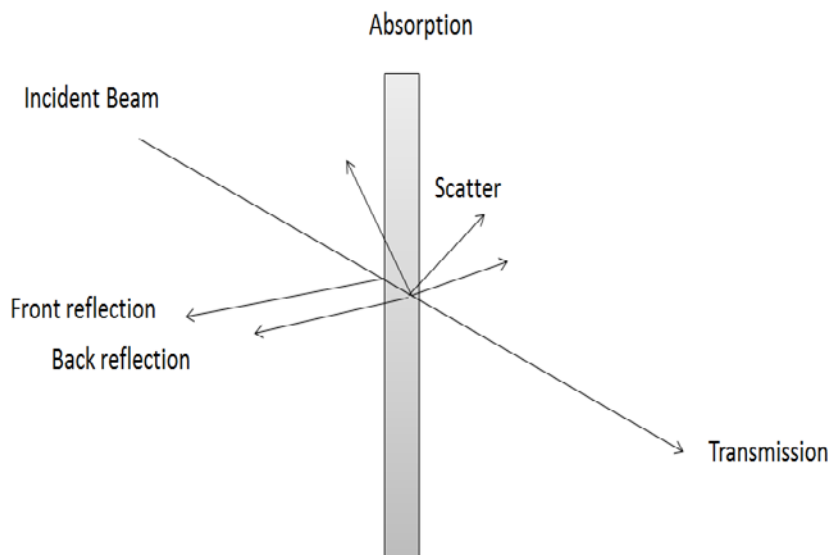


Figure 3.2 Interaction of light with a solid

3.2.4 Optical Modelling

A fitting procedure is now required to calculate the optical constants of the films. To extract the optical data from the reflection measurements obtained by UV-Vis spectroscopy a software package named Scout® has been used, where a 3 pseudo - layer semiconductor model was postulated. The scout model was setup with a surface, bulk and a substrate-interface pseudo layer. The surface and substrate-interface layers were limited to small thicknesses compared to the bulk layer, while the program was allowed to alter the thickness of each of the three layers independently and simultaneously adjust all other parameters for each layer to best describe the regions. The bulk layer influences the largest sway on the overall optical properties of the material such as refractive index, band gap and absorption coefficient.

The film was virtually split into the three afore-mentioned layers, each containing the dielectric functions of a-Si, polycrystallites and voids. The final results were drawn from a close match between a calculated spectrum and the measured spectrum, obtained from samples deposited on a silicon substrate. A schematic of the three layers is shown below.

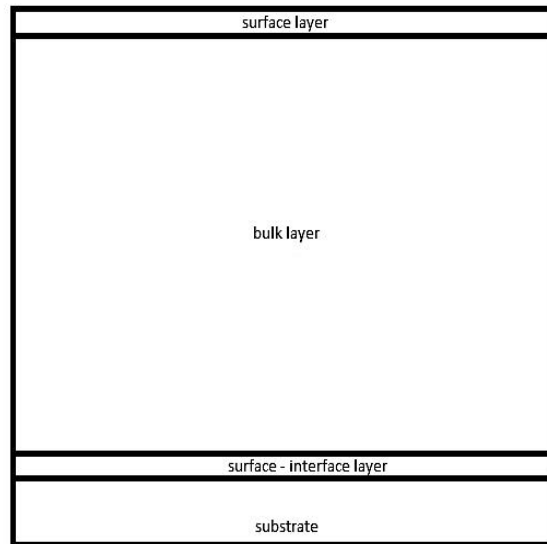


Figure 3.3 Schematic representation of thin film optical model.

Effective Medium Approximations (EMA) combines the dielectric functions of various materials as a matrix and particles, which allows for the calculation of a theoretical spectrum. Customarily the Bruggeman effective medium approximation (EMA) [3.5] is the theoretical model of choice, in this work the Looyenga EMA theoretical model was used. For high porosities it is advisable to use the Looyenga formula [3.6, 3.7]. This model, derived from the Bruggeman formulation, allows for percolation in a material to weigh a more dominant role in the determination of the optical properties. It can maintain a connected network for arbitrary porosities, whereas the Bruggeman formula switches off percolation and does not describe a network, but rather a system of isolated particles. A theoretical amorphous semiconductor, the O’Leary, Johnson and Lim (OJL) construct [3.8], was used for a-Si:H modelling.

3.3 X-ray Diffraction

3.3.1 Introduction

X-ray diffraction (XRD) analysis involves the scattering on x-rays from the atoms within a sample. The way in which these x-rays scatter provides insight into the atomic structure of the material. It allows for the quantification of whether a material is amorphous or crystalline.

3.3.2 Theory

X-ray radiation is generated by means of accelerating electrons, using a potential difference, towards a target element, in an x-ray tube. The electrons then put the target element in an excited state. Since all atoms long to be in a neutral state, the target atom will emit x-rays in all directions in its attempt to de-excite. These x-rays then escape the x-ray tube through a narrow incision in the tube, which are collimated to hit the sample material. The scattering x-rays from the sample are collected by a detector and interpreted electronically to produce a spectrum.

The spectrum produced is completely dependent on the scattering of the x-rays. The scattering can be either constructive or destructive. For diffraction to occur constructive scattering must take place and the wavelength of the x-ray to be less than the interatomic distance of the material. For constructive interference to take place Bragg's Law must be satisfied. Bragg's Law states that if two x-rays interact with two atoms in parallel planes then the difference in the path travelled by the x-ray must be equal to $2d\sin\theta$ and must be an integral number of the wavelength and is schematically depicted in the figure 3.4 below.

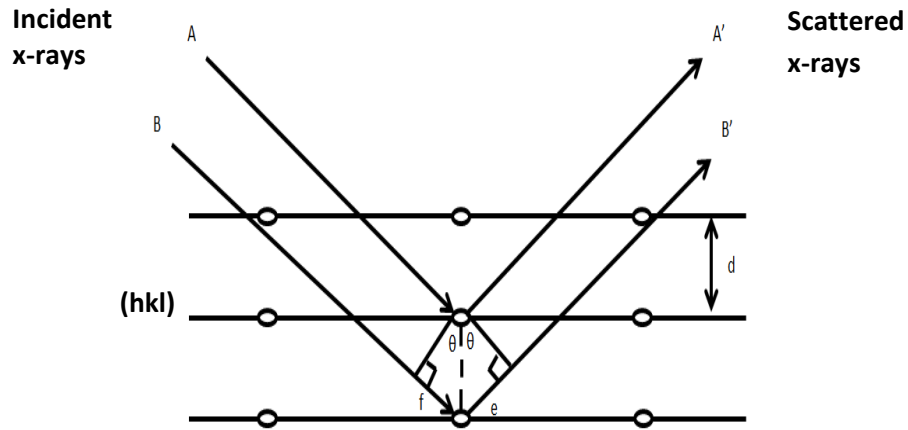


Figure 3.4 Conditions for Bragg's Law [3.9]

The path difference (PD) between the two incoming x-rays is;

$$PD = f + e \tag{3.14}$$

$$= d \sin \theta + d \sin \theta \tag{3.15}$$

$$= 2d \sin \theta \tag{3.16}$$



which satisfy the Bragg condition for constructive interference must be an integer number of the wavelength. Therefore

$$n\lambda = 2d \sin \theta \tag{3.17}$$

In 1912 Van Laue [3.9] introduced a different approach to diffraction. It imposed no constraints such as specular reflection, as is done with Bragg's Law. The crystal structure of a material consists of a lattice and a basis. Laue regarded a crystal as composed of identical basis positioned at sites R in the lattice. Incident radiation will then be reradiated in all directions and an intense peak will be observed in the generated spectrum. This peak will be observed at the wavelength in which x-rays scattered from all basis in the lattice interfere constructively.

The scattering vector, Δk , is the change in wave vector upon scattering and when added to the incident wave vector, k ($k = 2\pi/\lambda$), yields the scattered wave vector, k' ($k' = 2\pi/\lambda'$), as shown in Figure 3.5 [3.10]. This vector lies in reciprocal space, an abstract mathematical concept where distances are reciprocal to real space [3.10].

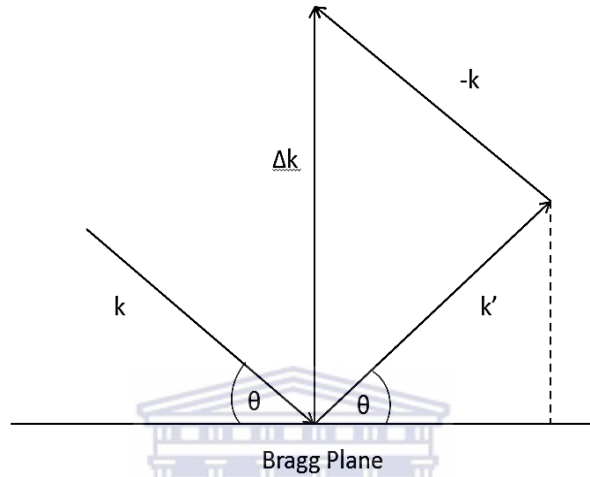


Figure 3.5 Schematic of diffraction occurring within a crystal postulated by Laue [3.9]

Utilizing the orthogonal relationship between the scattering vector and the crystal lattice vectors as well as the condition that the resultant of the incident and diffracted waves must be a point in reciprocal space, one arrives at the Laue equations [3.11]:

From the figure 3.5 above we know that;

$$\Delta k = k + k' \tag{3.18}$$

$$\Delta k = 2k \sin \theta \tag{3.19}$$

For Bragg's law to be satisfied;

$$2k \sin \theta = 2\pi \frac{n}{d} \tag{3.20}$$

With simple mathematical manipulation, the equation above can be rewritten as

$$n\lambda = 2d \sin \theta \quad \dots \text{Bragg's Law} \tag{3.21}$$

Depending on the crystallographic structure of the material, the diffracting planes can be predicted.

3.3.3 Crystal Geometry and Bravais Lattice

A point lattice can be defined by three translational unit vectors a , b and c , such that each point is isotropic. The figure 3.6 below depicts a point lattice and a unit cell. The units cells may be describes in terms of its lengths (a , b , c) and the angles between them (α , β , γ). The lengths and angles are defined as the lattice parameters of the unit cell. The vectors describing the unit cell are also shown in figure 3.6.

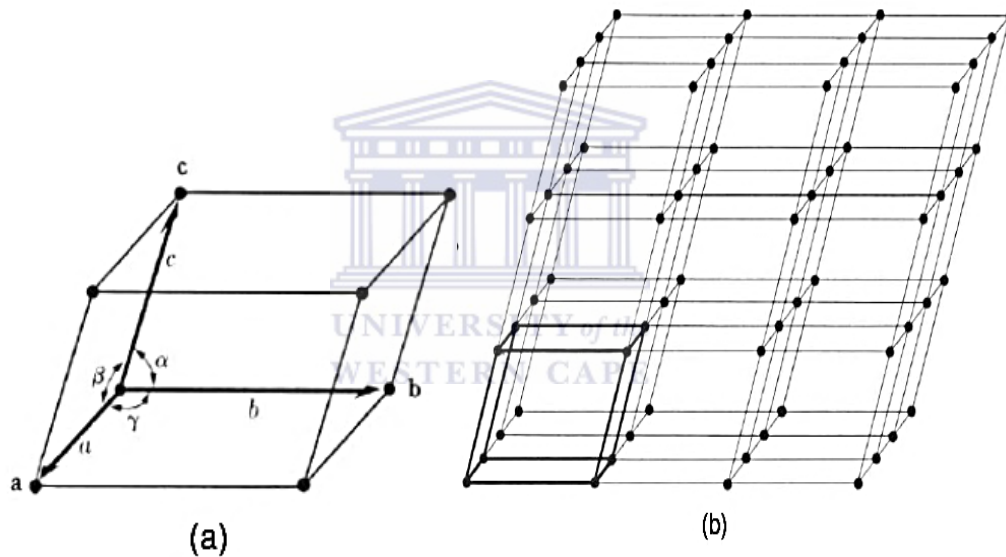


Figure 3.6 The periodic point lattice with its unit cell [3.10].

The position in a lattice can be determined by the integral multiple of the translational vectors expressed in equation 3.22.

$$\bar{r} = u\bar{a} + v\bar{b} + w\bar{c} \quad (3.22)$$

In which a , b , and c are the translational unit vectors and u , v and w are the integers. These integers are simply expressed as $[u,v,w]$. Negative indices are denoted with a bar index $[\bar{u}\bar{v}\bar{w}]$.

Figure 3.7 illustrates the direction indices for a unit cell.

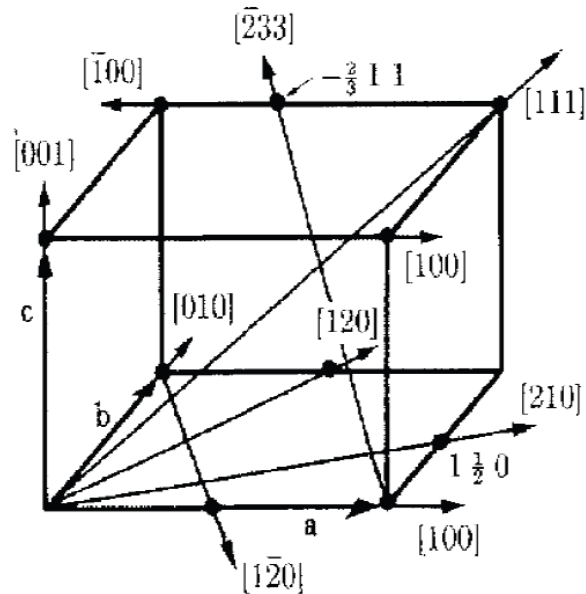
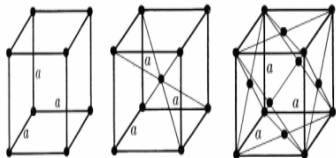
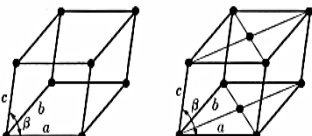
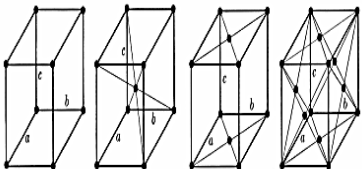
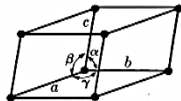
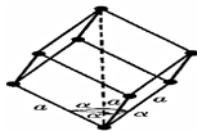
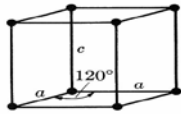
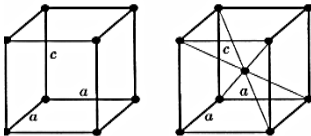


Figure 3.7 Schematic diagram of a unit cell showing all the indices of directions [3.10].

A lattice point group is the collection of symmetry operations (e.g. rotation and mirror reflection) that maintain a fixed point. There are fourteen different lattice types that, when certain symmetry operations are performed, remain invariant. These are known as Bravais lattices, are grouped under seven types of cells, which are divided into systems according to axial relations describing the cells [3.11]. Tabulated in table 3.2 are the descriptions of the 14 Bravais lattices [3.10].

Table 3.2 Crystallographic structure of various Bravais lattice [3.10]

System	Centering	Bravais Lattice
Cubic	Simple cubic	
	Body centred	
	Face centred	
Monoclinic	Simple cubic	
	Base centred	
Orthorhombic	Simple cubic	
	Body centred	
	Face centred	
	Base centred	
Triclinic	Simple cubic	
Rhombohedra/ Trigonal	Simple cubic	
Hexagonal	Simple cubic	
Tetragonal	Simple cubic	
	Body centred	

The symmetry of crystals results in crystal planes labelled as (h k l), which are an important aspect of diffraction. Planes related by symmetry are called planes of a form denoted by {h k l}. Planes of a form have the same spacing but different indices. Directions related by symmetry are called directions of a form denoted by $\langle u v w \rangle$.

3.3.4 Experimental Setup

X-ray diffraction analysis has been performed on an x-ray θ - 2θ diffractometer, figure 3.8. It consists of a sample stage, a detector and x-ray generation. In this setup the x-ray tube is kept stationary and the sample moves by an amount θ and the detector moves simultaneously by an amount 2θ .

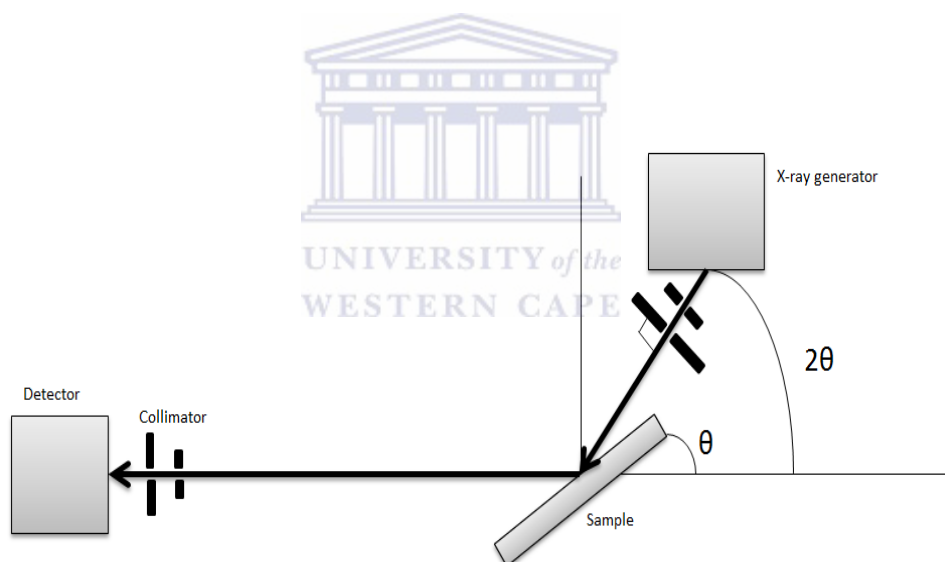


Figure 3.8 Setup X-ray Diffractometer θ - 2θ .

X-ray diffraction (XRD) was performed, on samples deposited on corning 7059 glass substrates, using a PANalytical Xpert diffractometer at 2θ -values ranging from $5 - 90^\circ$, with a step size of 0.02° . Copper $K\alpha_1$ radiation was used as the x-ray source with a wavelength of 1.5406 \AA .

3.4 Raman Spectroscopy

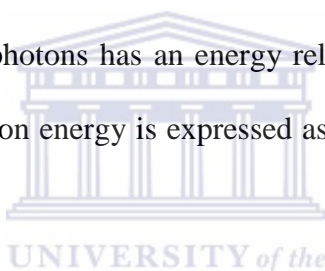
3.4.1 Introduction

Raman spectroscopy is a non-destructive technique that involves the inelastic scattering of incident light on a sample. This type of analysis provides qualitative and quantitative information on material crystallinity and insight into the electronic and structural properties of a material.

3.4.2 Theory

Approximately 99.9% of all incident photons undergo elastic Rayleigh scattering and the rest will scatter inelastically. These inelastic scattered photons are what produce the Raman signal.

The energy of Raman scattered photons has an energy related to the characteristic vibration of the scattering molecule. The photon energy is expressed as the difference between the incoming and scattered photon frequency.



A monochromatic light impinges on a sample and distorts the electron cloud that surrounds the molecules. The distortion of the electron cloud induces an electric dipole moment, which has an electric field. The induced dipole moment accompanied by the electric field results in an oscillating induced dipole moment. The resulting oscillating induced dipole moment will emit radiation in all directions.

The distortion of the electron cloud puts the molecule in an excited state. These molecules can then return to their original state via one of three methods;

- 1) Rayleigh scattering: When elastic interaction occurs between the incident photon and the material, but no energy is transferred.
- 2) Raman scattering/ Stokes Scattering: Inelastic interaction of the incident photon results in energy transfer from the photon to the molecule. Inelastic scattering may also result in the

production of a photon. This is also known as Stokes scattering. When a molecule de-excites, but to energy state higher than its original state, before excitation occurred.

- 3) Anti-Stokes Scattering: This scattering method involves the de excitation of a molecule to a state lower than the state at which it was excited from as seen in figure 3.9. illustrating the electron de excitation paths in Raman spectroscopy.

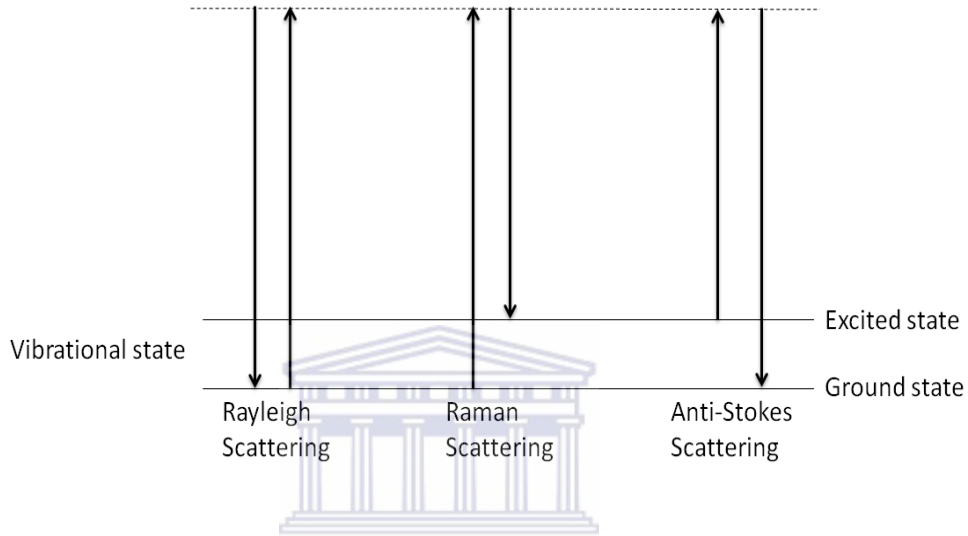


Figure 3.9 schematic of electron de-excitation in Raman spectroscopy [3.12]

In c-Si a sharp narrow peak is observed at 520 cm^{-1} in the resulting Raman spectra. The absence of this peak indicates no crystallinity in the thin film [3.13]. The root mean square bond angle variation, $\Delta\theta_b$ given by

$$\frac{\Gamma}{2} \cong 7.4 + (3.2 * \Delta\theta_b) \quad (3.22)$$

Where Γ is the full-width-half-maximum (FWHM) of the transverse-optical peak [3.14]. The value of $\Delta\theta_b$ varies between 7.0° and 14.1° for a-Si:H films and indicates the order within a sample [3.15].

2.4.3 Experimental Setup

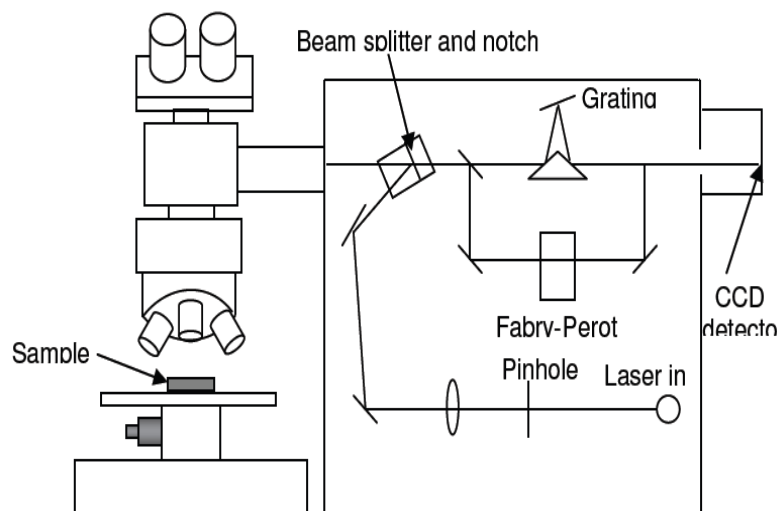


Figure 3.10 Schematic diagram of Raman spectrometer [3.12]

The Raman measurements were performed in a range of 100 to 700 cm^{-1} . The measurements were performed using 532.06 nm argon (Ar) green laser line with an excitation power of 1.2 mW. The signal was recorded by a CCD detector, cooled at $-135\text{ }^{\circ}\text{C}$. A schematic of the Horiba Jobin Yvon HR800 micro-Raman spectrometer is shown in figure 3.10 above.

3.5 Fourier Transform Infrared Spectroscopy

3.5.1 Introduction

Fourier transform infra-red (FTIR) spectroscopy involves interaction of a large wavelength infra-red beam with a thin film. The substrate for the deposited film must be transparent to IR light such that the diffracted light can be detected. FTIR provides information into the bonding configuration, bonded hydrogen content and bond density of the material under investigation.

3.5.2 Theory

FTIR is a non-destructive and easy to perform technique. An IR beam is passed through the thin film. The unique chemical bonds in the material will absorb the IR radiation when the frequency of that radiation is equal to the vibrational frequency of the bond. The rest of the radiation passes through the thin film toward the detector and the intensity of the transmitted signal through a depth l is given by [3.16]

$$T = \frac{I_0}{I_t} = e^{-kcl} \quad (3.23)$$

A background spectrum is measured to eliminate the absorption from the c-Si substrate from the measured transmission spectrum of the sample.

Table 3.3 The assignments of the Si-H_x vibrational modes [3.17]

Energy (cm ⁻¹)	Bonding Configuration	Vibrational mode
630	≡Si-H, (=Si=H ₂) _n for n ≥ 1, -Si≡H ₃	Rocking
845	(=Si=H ₂) _n for n ≥ 2	Bending
880	=Si=H ₂	Bending
890	(=Si=H ₂) _n for n ≥ 2	Bending
2000	≡Si-H (isolated)	Stretching
2070 – 2100	≡Si-H (on voids), (=Si=H ₂) _n for n ≥ 1	Stretching
2130	-Si≡H ₃	Stretching

Different vibrational modes can be observed and is described in table 3.3. A rocking mode centred at 640 cm⁻¹, bending mode around 800 – 900 cm⁻¹ and the stretching mode in the 2000 –

2100 cm^{-1} wavenumber range. These modes are attributed to Si-H_x ($x = 1, 2, 3$) bond vibrational mode. Figure 3.11 illustrates a typical FTIR spectrum for hydrogenated amorphous silicon thin films.

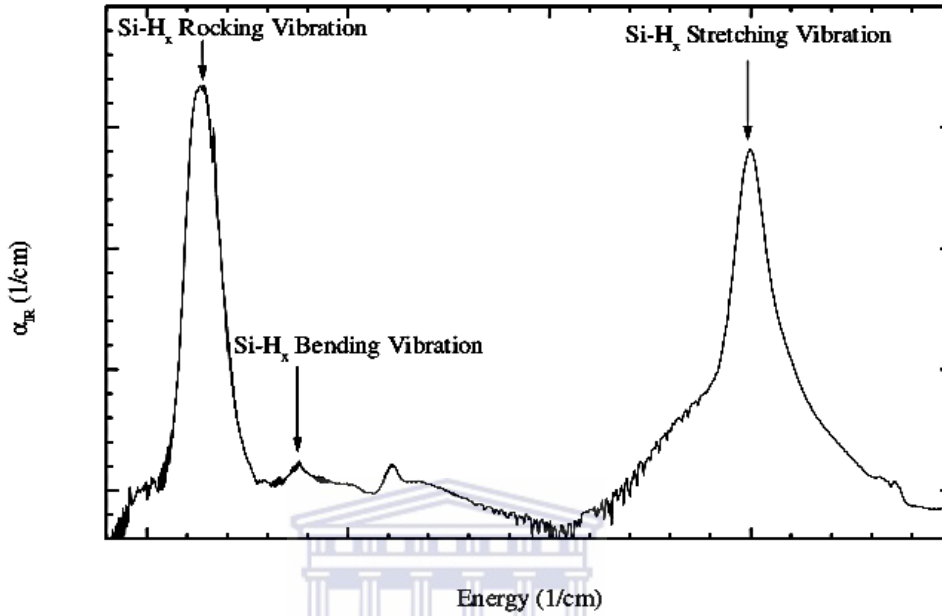


Figure 3.11 Example of an a-Si:H film FTIR spectrum [3.18]

The integrated absorption I_w is given as a function of the absorption coefficient $\alpha(w)$ by:

$$I_w = \int \frac{\alpha(w)}{w} dw \quad (3.24)$$

Where w is the frequency in cm^{-1} and the integral is over the absorption band of interest [3.19]. The hydrogen concentration (N_H) is related to the integrated absorption I_w via:

$$N_H = A_w I_w \quad (3.25)$$

A_w is the proportionality constant that is dependent on the hydrogen concentration of the different vibrational modes [3.20]. The exact value of this constant varies somewhat in literature, for this purpose $A_{640} = 1.6 \times 10^{19} \text{ cm}^{-2}$ as determined by Shank *et al.* [3.21] and $A_{2000-2130} = 2.2 \times 10^{20} \text{ cm}^{-2}$ as proposed by Langford *et al* [2.22] will be used. The proportionality constants has been calculated for

a-Si:H, thus its application to another material will introduce a measure of error. FTIR analysis estimates the integrated strength along with a typical error < 15 %. Therefore the concentration of bonded hydrogen determined by FTIR is given by:

$$[\text{H}]_{\text{rocking}} = \frac{I_{630}A_{630}}{n_{\text{Si}}} 100 \text{ at\%} \quad (3.26)$$

Information on the microstructure of the thin film can also be obtained by the ratio:

$$R^* = \frac{I_{2100}}{I_{2000}+I_{2100}} \quad (3.27)$$

R^* is thus an indication of the structural inhomogeneity of the a-Si:H thin films, such as microvoids in the material. When the $R^* < 0.1$ the thin film is usual of a good opto-electronic standard. With an increase the 2100 cm^{-1} mode contribution, the microstructure parameter increases, indicative of poor quality material [3.23]

3.5.3 Experimental Setup

FTIR spectrometer consist of three major components; a radiation source, an interferometer and a detector. The radiation source produces continuous radiation, with an energy profile characteristic to the source. To measure and differentiate the absorption of component frequencies an interferometer is used. Its function is to divide radiant beams and generate and optical path difference between the beams. To produce a repetitive interference signals as a function of the optical path difference, by the detector, the beams are then again recombined. The most commonly used interferometer used is the Michelson interferometer and a typical FTIR spectrometer is displayed below in figure 3.12:

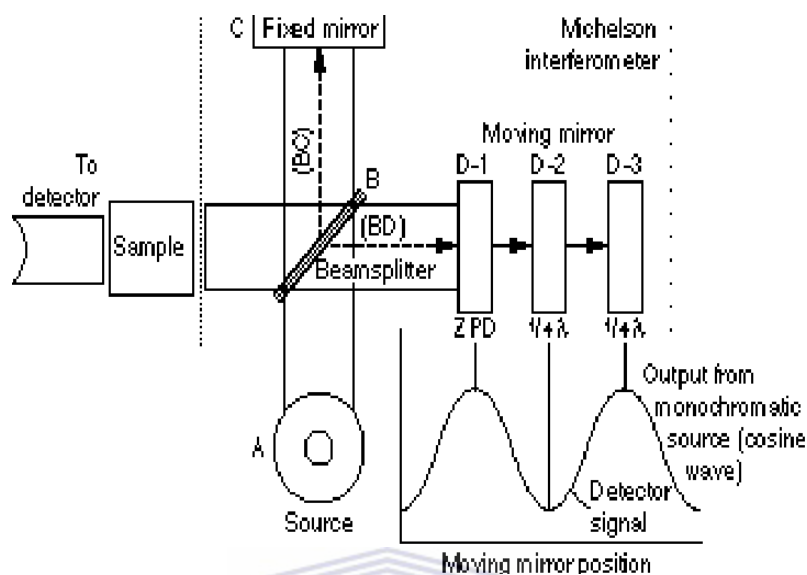


Figure 3.12 Simplified schematic of a typical FTIR spectrometer [3.24]

(FTIR) absorption spectra were analysed in transmission geometry from $400 - 4000 \text{ cm}^{-1}$ with a spectral resolution of 1 cm^{-1} , using a Perkin-Elmer Spectrum 100 FTIR spectrophotometer.

3.6 Elastic Recoil Detection

3.6.1 Introduction

Electron recoil detection (ERD) analysis uses MeV ion bombardment, usually of H^+ or He^+ ions, impinged on a target material. The number and energy of the ions scattered in the direction of the detector are then determined through this process. The detector captures information from the atoms that are ejected from the surface from the target. This technique is highly efficient in detecting lighter elements such as hydrogen with the target material.

3.6.2 Theory

The simple operation behind an ERD measurement is the irradiation of a target sample by a high energy ion beam. The energy distribution from the different atoms ejected from the target sample at a certain angle, θ , is then recorded [3.25]

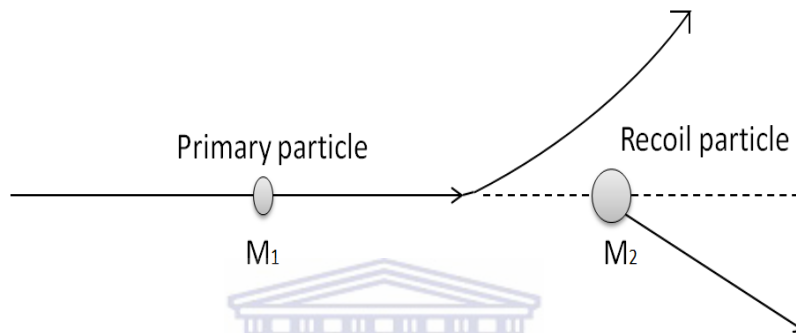


Figure 3.13 interaction of ion beam with the target [3.25]

The transfer of energy from the primary particle to the recoil particle during scattering will determine the amount of energy the recoil atom will possess. The energy loss by both participating particles will also determine the deviation from the energy of the recoil particle with depth. The interaction of the ion beam with the target atom is illustrated in figure 3.13.

The governing equation for this collision is described in terms of Coulombs repulsion force between two nuclei. The energy transferred to the recoil particle is given by the Kinematic factor derived from the conservation of momentum and energy laws [3.26];

$$K = \frac{4M_1M_2\cos^2\theta}{(M_1 + M_2)^2} \quad (3.28)$$

The probability that one particle from the ion beam will eject a recoil element for the target and that it projects in the direction of the detector is an important characteristic in this collision

process. This probability is proportional to the areal density of the target and the solid angle of the detector, which is described by Rutherford's differential cross section [3.27];

$$\frac{d\sigma}{d\Omega} = \left(\frac{Z_1 Z_2 e^2 (1 + \frac{M_1}{M_2})}{2E_0} \right)^2 \frac{1}{\cos^3\theta} \quad (3.29)$$

Another useful additive result from ERD is the ability to obtain a correlation form between sample depth and energy, by evaluating the stopping power (energy required to stop an ion moving within the target material). Thus for a good depth resolution a good detector energy resolution and also a well-defined energy of particles recoiling from the target is required. An Ideal sample for optimum depth resolution is one that is laterally uniform on the surface. The depth resolution is further affected by energy straggling, increasing so with increasing depth [3.28].



3.6.3 Experimental setup

The ERD data has been collected at the Material Research group of iThemba Labs. $^4\text{He}^+$ particles in the energy range 2 – 3 MeV were accelerated by a van der Graaf accelerator through a 1 nm collimator toward the sample located in a high vacuum chamber, $<10^{-4}$ mbar. The sample was tilted at an angle of 15° with respect to the incident beam. The silicon detector was positioned at a recoil angle of 30° . An aluminium foil is placed in front of the detector to act as the stopper foil, which collects the heavier ions such that it does not interfere with the detection of hydrogen ions. The schematic setup of ERD system is shown below.

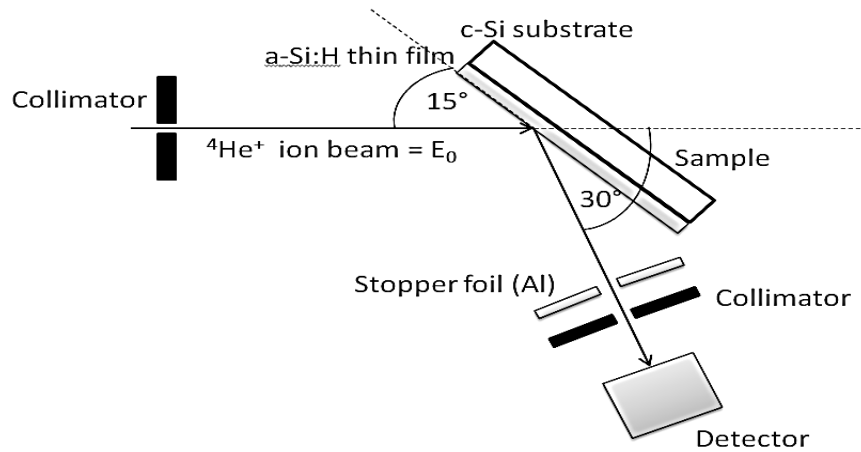


Figure 3.14 Schematic setup for ERD in conventional geometry [3.26]

Since an ERD spectrum displays the different energy channels for various photon energies, prior to analysis of ERD spectra, an energy-channel calibration must be completed. A aluminised mylar ($\text{C}_{10}\text{H}_8\text{O}_4$) foil, $\sim 15 \mu\text{m}$ thick, is bombarded with three ion beams of energies, 2, 2.5 and 3 MeV. Three ERD spectra are obtained from this and the energy and channel is then correlated using the linear relation;

$$E [\text{keV}] = A + (B \times \text{channel}) \quad (3.30)$$

where A is the calibration offset and B the energy per channel factor.

3.7 Atomic Force Microscopy

3.7.1 Introduction

Atomic force microscopy (AFM) analysis is a powerful tool used to image and measure properties of a material. It has been employed to investigate the surface morphology of the

material. This analysis technique involves the scanning of the thin film surface, with a SiN_x tip, of the samples deposited on single crystalline silicon substrates.

3.7.2 Theory

AFM was first developed in 1986 by Binnig, Quate and Gerber [3.29, 3.30]. It is part of a larger group of instruments called scanning tunnelling microscopes. The AFM instrument consists of a cantilever with a sharp tip (SiN_x probe). When this tip comes into close proximity to the sample surface, it measures the forces between them. The cantilever will bend in a direction dependant on the attractive or repulsive forces that result from the interaction. The bending of the cantilever is detected by means of a laser that is shone on the back of the cantilever behind the tip. The laser gets reflected off the cantilever and into a photo detector that tracks the position of the probe across the surface [3.31]. Diagrammatical illustration of an AFM is shown in figure 3.15 below.

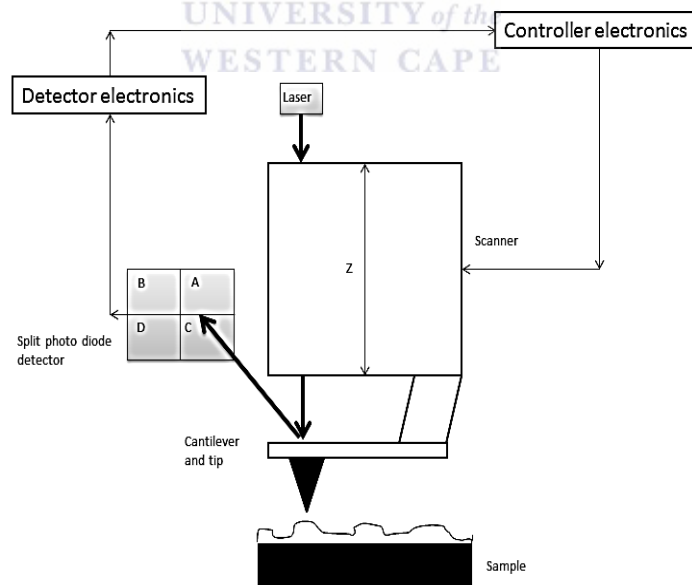


Figure 3.15 Atomic force microscope operation and setup [3.30]

The images obtained are a measure of the interactive forces between the SiN_x tip and the sample surface. The AFM has three main operating modes;

- 1) Contact Mode
- 2) Tapping Mode

These operation modes are exactly as they read. The contact mode is an operation mode by which the tip makes physical contact with sample surface. Whereas with the tapping mode, which is more commonly used, the tip intermittently taps the surface of the sample. Within the tapping mode the cantilever oscillates close to its resonance frequency, at fixed amplitude, to ensure constant interaction between the tip and sample during analysis.

The Van de Waal forces between the tip and the samples cause a change in the oscillation amplitude and resonant frequency. The variation in the amplitude coincides with the adjustment of the piezoelectric material, to maintain a constant interaction. When a tunnelling current is established between the sample and the tip, a voltage gradient can be formed. This voltage gradient results in the expansion or contraction of the piezocrystal and in turn the movement in the x, y and z direction. This information is then recorded as a height image. The tapping mode is advantageous since it eliminates a large portion of the shear forces experienced between the tip and the sample surface, as when in the contact mode. The consequences are less surface damage to the sample.

3.7.3 Experimental Setup

AFM imaging and roughness analysis were obtained with a Nanoman Veeco AFM 3100 scanner, used in the tapping mode. Images were collected on a 5 × 5 and 3 × 3 scale.

3.8 Scanning Electron Microscopy

3.8.1 Introduction

Scanning electron microscopy (SEM) is a technique that can be used to obtain material structural information, elemental composition and imaging. It entails the emission of electrons from a heated cathode, commonly a tungsten filament, which is scattered off a specimen.

3.8.2 Theory

A filament is heated to generate electron. These electrons are accelerated toward the specimen by a potential difference. The specimen acts as the anode in this setup. Electromagnetic lenses are used to keep the electron beam focused along the focal length. Condenser electromagnetic lenses focus the electron beam onto a focal point. The location of the various components can be seen in figure 5.16. Furthermore objective electromagnetic lenses are used to further focus the beam onto a focal point on the specimen, through an objective aperture. The objective aperture controls the beam spot size on the specimen [3.32].

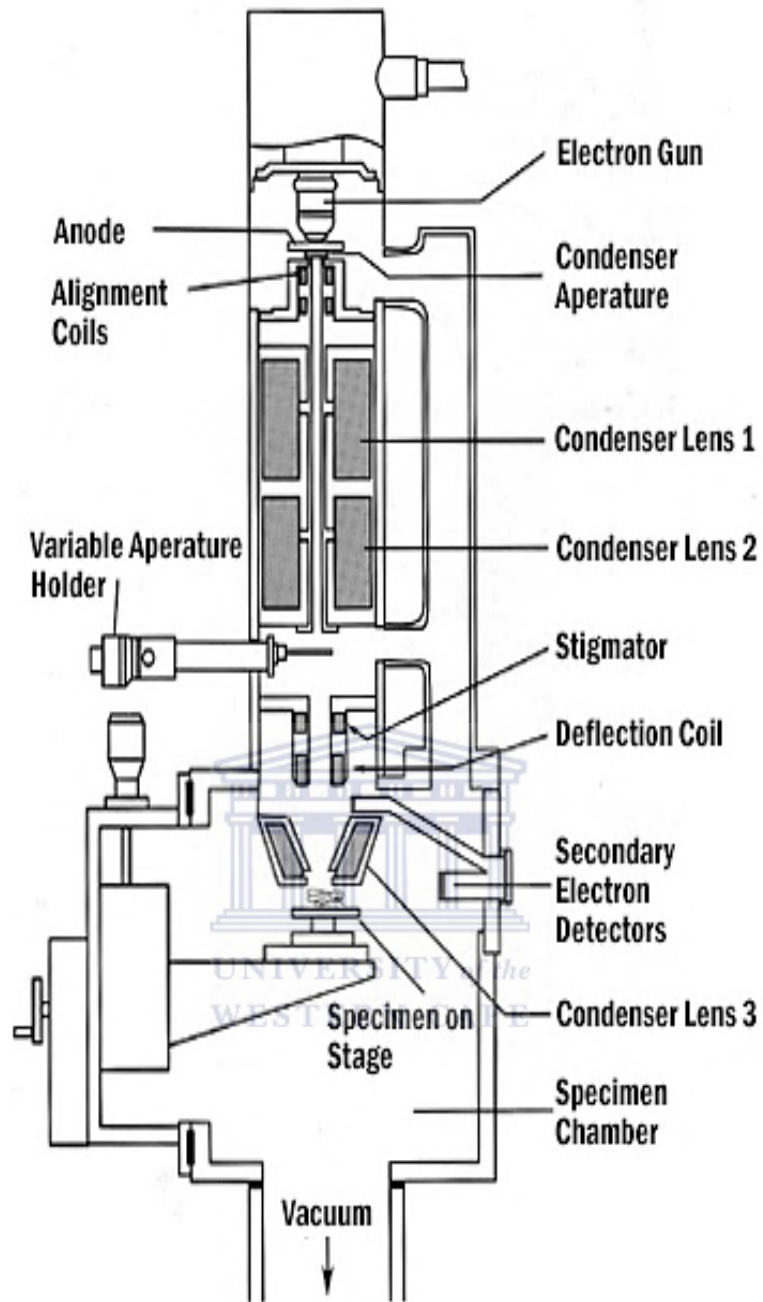


Figure 3.16 Scanning electron microscope system setup [3.33]

The focused beam is then scanned across the specimen by scanning coils. The interaction of the scanning electron beam produces signals that are detected and used to form an image of the scanned specimen area.

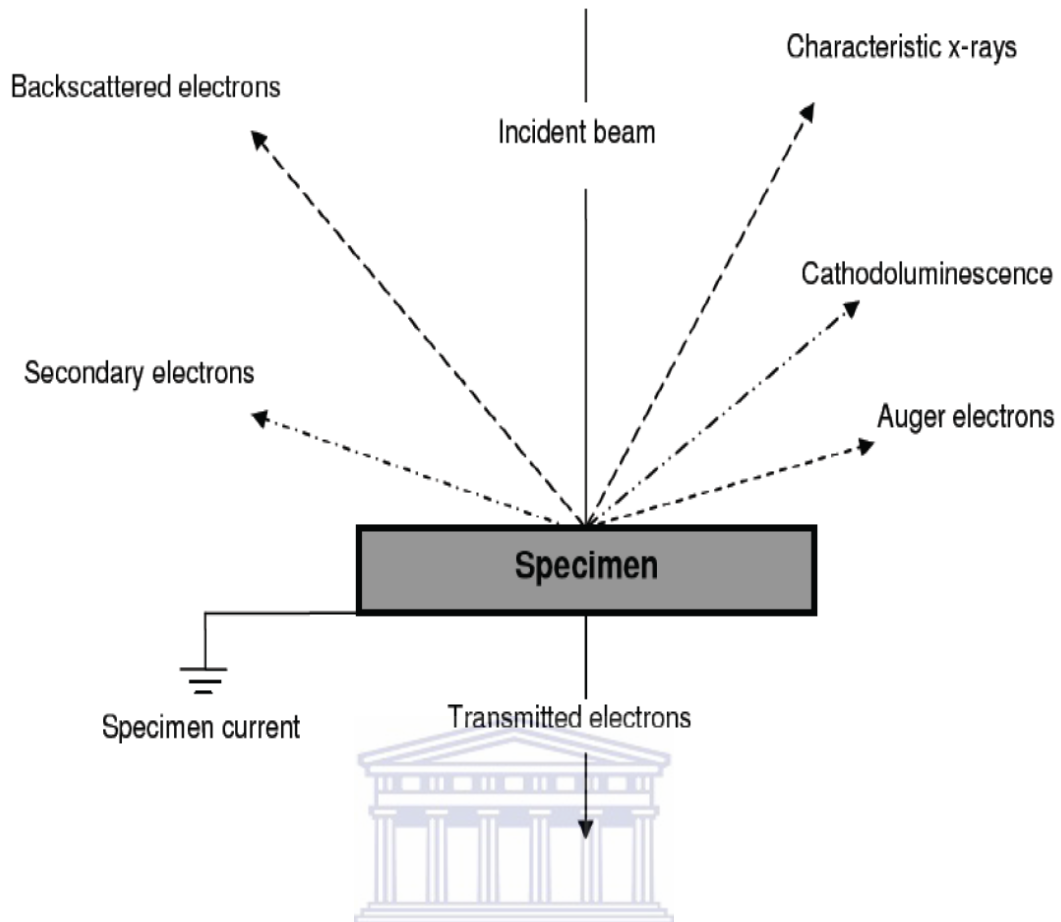


Figure 3.17 Representation of possible signals generated from SEM analysis [3.34]

A number of signals are generated from this interaction between the beam and specimen. Each signal can unveil different information about the specimen. The various signals generated can be seen in figure 3.17. The information provided by these signals generated are summarized in table 3.4.

Table 3.4 Signal generation within the SEM and information gathered [3.35]

Event	Between	Signal	Resolution	Use
Elastic Scattering	Beam electron/ specimen nuclei or electrons	Backscatter electron	>1000 nm	Atomic number and Topographical contrast
Inelastic Scattering	Beam electrons or backscatter electrons/ specimen electrons	Secondary electron	10 nm or better	Surface structure
	Beam electrons or backscatter electrons/ specimen nuclei	Continuum X- rays		Not a useful signal
Recombination	Free electrons generated/ positive holes	Cathodlumiescen ce	< 80 nm	Inpurity concentration
		Characteristic X-ray	Measured in eV	Elemental composition
		Auger electrons	Measured in eV	Surface composition
Transmission	Electrons through specimen	Transmitted electrons	5 nm or better	Internal ultra- structure
Energy transfer	Specimen/ ground	Specimen current	Poorer than 2 ° image	Atomic number constast

3.8.3 Interaction volume and Resolution

An 'interaction volume' is created when the electron beam interacts with the specimen, whereby the electrons undergo various scattering events. Atoms residing in the interaction volume are excited and emit signals from various depths of the interaction volume, depending on the energy of each signal, see figure 3.18. Elemental or surface analysis can be performed, depending on the nature and origin of the emitted signal. Image formation of the surface of a specimen depends mainly on the production of secondary electrons. Secondary electrons are low-energy electrons and therefore are absorbed by the sample, when produced deep within the interaction volume. Only those close to the surface usually have sufficient energy to escape from the sample surface, therefore the secondary electrons provides a surface profile image of the sample.

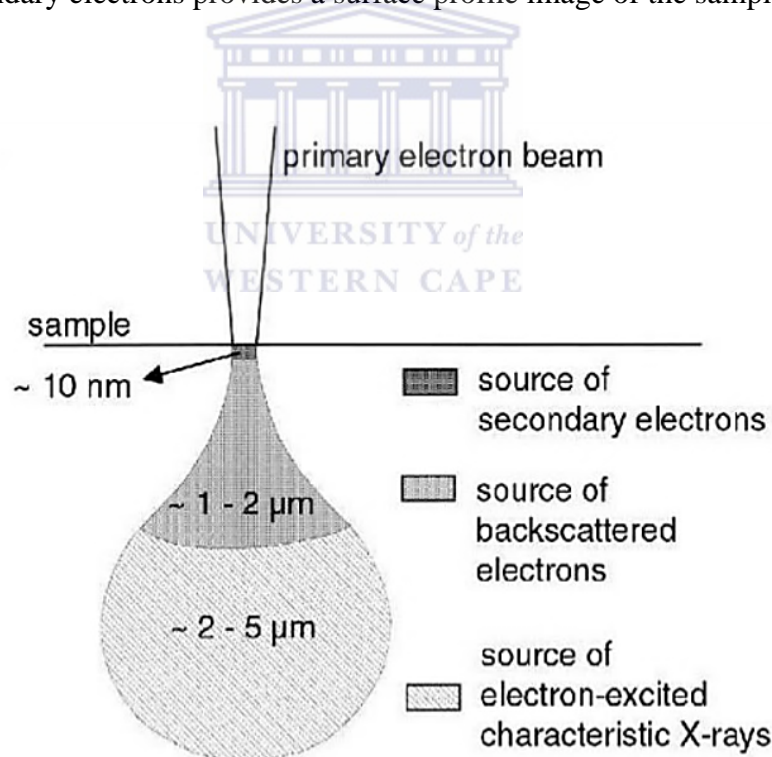


Figure 3.18 Interaction volumes between the electron beam and the specimen [3.35]

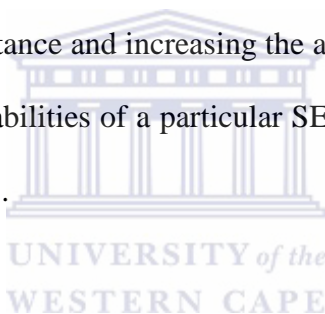
The secondary electron image is the most common image used as it offers greater resolution compared to the other scanning signals. Features down to 10 nm and better can be resolved by

the secondary electron signal. Furthermore this signal is used to control the brightness of an image and allows for the distinction in contrast of the sample surface.

The resolution of a microscope is defined as the closest distance between two entities such that it can still be differentiated separately. The resolution of a SEM is governed by ABBE's equation, given by;

$$d = \frac{0.612 \lambda}{\mu \sin \alpha} \quad (3.31)$$

The wavelength of the electron and semi-angle of represented by λ and α respectively and μ is a constant in this equation. The resolution (d) can however be improved by decreasing the semi-angle, decreasing the working distance and increasing the accelerating voltage. These parameters can be varied and depend on capabilities of a particular SEM, the specimen investigated and the desired information wanted [3.35].



3.8.4 Energy Dispersive Spectroscopy (EDS)

Energy dispersive x-ray spectroscopy (EDS) is a widely used technique, during electron microscopy, for quantification of elemental composition. The EDS procedure consists of the generation, detection and quantification of characteristic x-rays emitted from the sample.

During SEM analysis, electrons are removed from the sample at different energy levels of the atoms within the sample, by the incident beam. The loss of an electron leaves the atom in an excited state. Figure 3.19 shows a schematic representation of an atom and is the basis of EDS. The energy levels surrounding the nucleus of the atom are labelled K, L, M... which correspond to the principle quantum number, $n = 1, 2, 3, \dots$. To return to its more favoured, ground state, an electron from one of the outer shells, such as the L or M shell, should fill the vacancy left behind. A discrete

amount of energy, characteristic of the atom, is emitted as the difference in energy of the excited electron energy level and the de-excited energy level. This energy is emitted as a characteristic x-rays and allows for the identification of an element. In practice only elements with an atomic number $Z > 4$ can be detected.

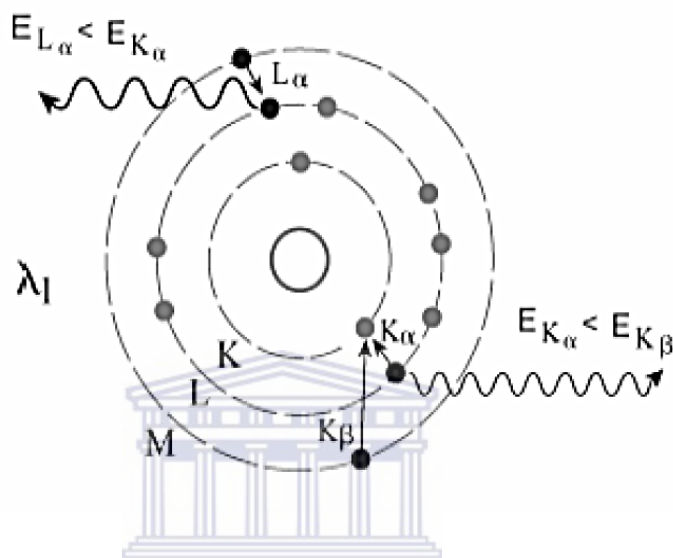


Figure 3.19 Characteristic x-ray emission by an atom [3.35]

The technique employs the separation of characteristic x-rays according to their energies, and is achieved with the assistance of a semiconductor detector. This absorbed energy, from the x-ray, is then converted to an electronic signal, which is emitted and amplified. The amplified electrical pulses from the semiconductor are converted to digital form and fed into a multi-channel analyzer (MCA). The function of the MCA is to sort the signals and counts the number of x-rays received such that this information can be used to generate a spectrum.

3.8.5 Experimental Setup

An Zeiss Auriga FEG scanning electron microscope was used to investigate samples deposited on single crystalline silicon substrates. An accelerating voltage of 1 kV was used at a working

distance of 3 nm. EDS analysis was performed using a Si solid state drift detector attached to the Zeiss Auriga FEG SEM. The peak position was determined using OXFORD Instrument K Man software.

3.9 Transmission Electron Microscopy

3.9.1 Introduction

The highly influential and sought after technique for insight into specimen surface, composition and atomic imaging of a sample is Transmission Electron Microscopy (TEM). It is used across a vast number of disciplines of science.

3.9.2 Theory

TEM involves the penetration of an electron beam through a samples specimen. Therefore the specimen in question needs to be extremely thin such that electrons being studies can pass through to produce the image.

The electron beam can interact with the specimen in three manners. It can be undeflected by the target and transmit straight through. The electron beam could also be deflected and either lose no energy through the interaction with the target or lose a significant amount of energy. These electrons contribute to the image that is produced on the fluorescent screen, and the extent of its contribution will depend on the path it followed and the nature of the target material itself.

In the figure below, the interaction of the electron beam with different specimens of varying thickness and crystal structure is illustrated. For a 10 nm thick amorphous carbon specimen, assuming an incident beam consisting of 100 electrons, 9 electrons are scattered. Since carbon is

a light element it scatters electrons weakly. If an amorphous carbon specimen is now considered with twice the thickness of (a), a more significant deflection of electron will be achieved.

From (a) and (b) the role of thickness can be seen but the type of specimen also has an effect on how the electron beam interacts. Region (c) is amorphous lead (Pb) and (d) is crystalline Pb both of the same thickness, 20 nm. Amorphous Pb is a heavier element compared to carbon so naturally this will result in a larger deflection of electron but through smaller deflection angles. When Pb is in a crystalline form, diffraction will occur along a specific diffraction plane within the specimen crystal structure. In this case either all the electrons will be deflected, at a Bragg angle to the unscattered beam, or none at all or the entire beam, 100 electrons, will transmit through the sample as seen in the figure below.

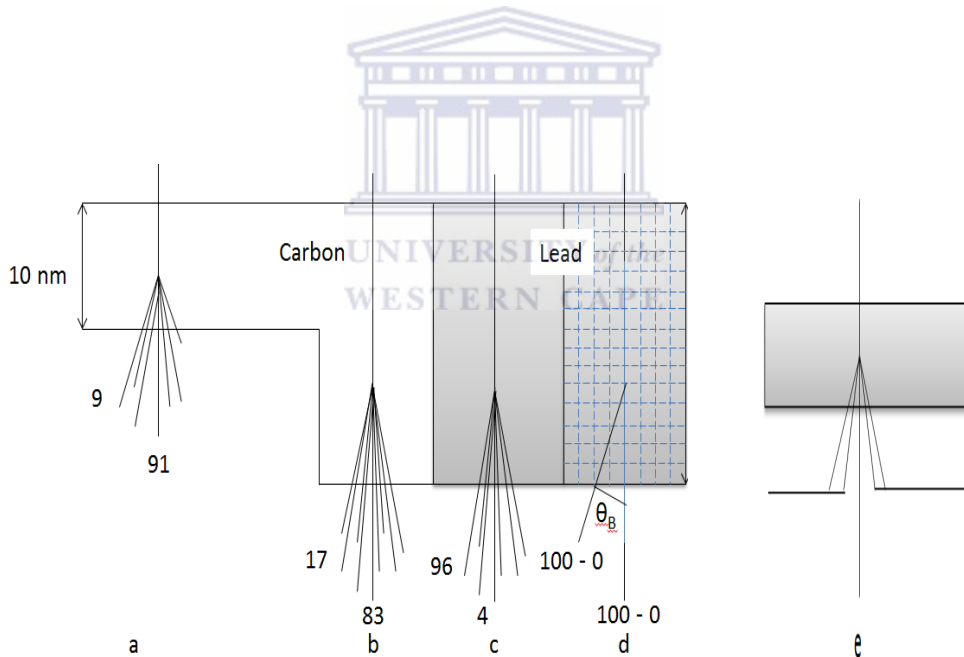


Figure 3.20 (a-d) interaction of 100 electrons accelerated toward carbon and lead of either varying thickness or material phase and (e) the operation of the objective aperture [3.35].

The brightness is determined by the number of unscattered electrons. In region (e), figure 3.20, the effects of the objective aperture can be seen. Therefore the brightness of each image will be in the following order; a, b and c. [3.34].

To get a more concise understanding on the electron optics a simple projection microscope can be examined and is illustrated below.

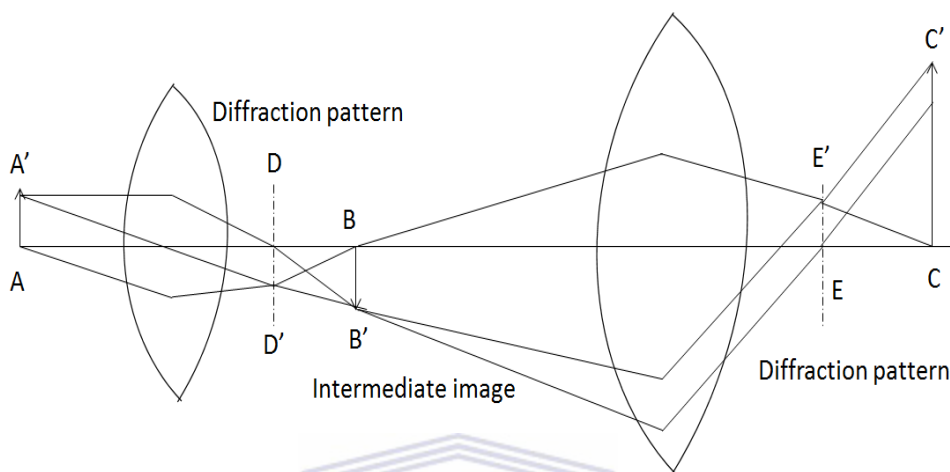
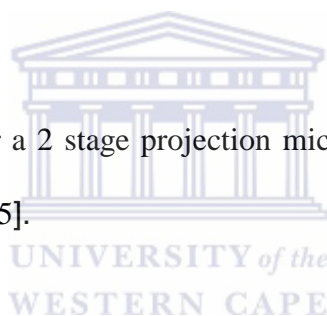


Figure 3.21 The ray diagram for a 2 stage projection microscope showing the positions of the diffraction pattern and image [3.35].



Two sets of parallel rays emerge from the specimen (AA'). The two sets of parallel pass through an objective lens and are diffracted depending on the distance of the ray from the focal plane. Each set of the parallel rays will meet at points D and D' on the back of the focal plane of the objective lens. On the plane BB' an intermediate image of the specimen can be viewed. When the viewing screen is placed at the planes DD' or EE' a diffraction pattern can be seen. The second objective lens further magnifies the image of the specimen.

As mentioned before diffraction can only occur if the Bragg relation is satisfied. This occurs when a crystal is orientated such that the incident beam is parallel to a specific diffraction plane, diffracting at Bragg's angle. Since diffracted electrons are mainly focused in the Bragg condition range, a crystal appears brighter if the beam passes the objective aperture and dark if stopped by

it. Depending on the phase of the material, if a specimen is polycrystalline the orientation of the various grains with respect the electron beam will govern the brightness and darkness of an image.

In the figure 3.22, above, a single crystalline material (a) will give rise to a diffraction pattern consisting of a regular array of spots. With a polycrystalline material (b) in which there is several crystal orientations the diffraction pattern will be a summation of the individual diffraction patterns. For a sample with several crystals (c) which are randomly orientated to one another, the diffraction pattern will be seen as concentric rings. These concentric circles arise as a result of the diffraction spots of all the crystals being so close together they appear continuous.

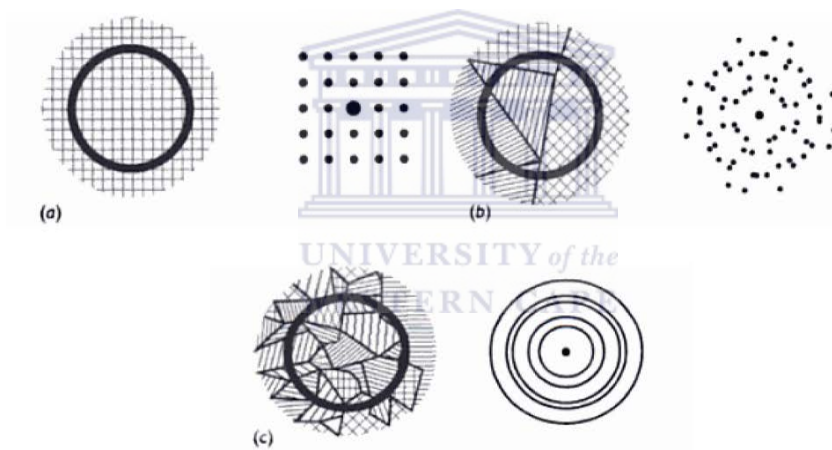


Figure 3.22 Diffraction pattern arising from different specimen microstructures [3.35]

3.8.3 Experimental setup

The general assembly of a TEM is shown in figure 3.23. The Tem experimental setup consists of an electron gun, serving as the electron source. A series of electromagnetic lenses used to magnify the specimen image, a viewing screen and a camera. All these components are incorporated into a single vertical column and are depicted in figure 3.23 below.

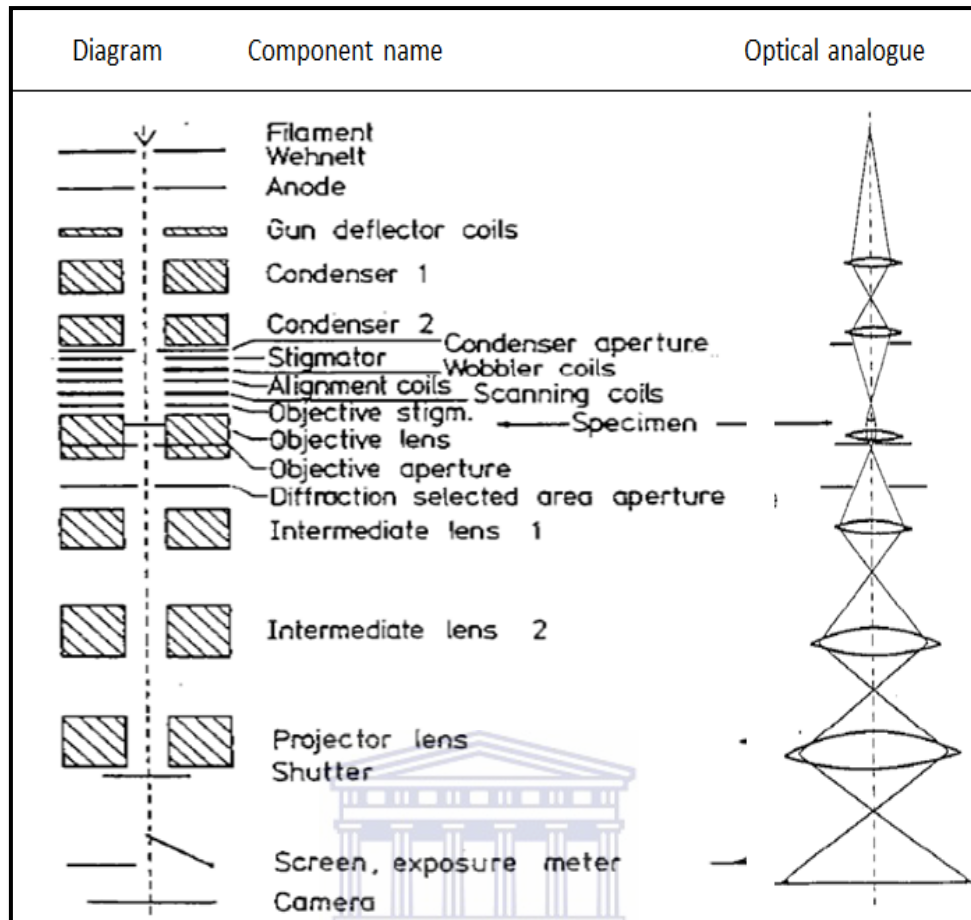


Figure 3.23 A cross-section of the basic components and an optical analogue of the TEM [3.34]

Electrons are produced through the heating of a filament. The electrons are accelerated toward an anode and get deflected by gun deflector coils onto the optical axis and enter the condenser system of the microscope. The first condenser lens focuses the beam to a spot. Once focused the second condenser lens projects the beam spot onto the specimen. The condenser aperture then determines the intensity and illumination of the beam by controlling the inlet of electrons. The condenser stigmator compensates for the beam profile deviating from a circular beam path, known as stigmation. The role of the wobbler coils and alignment coils are to aid with beam focusing and to keep the beam along the optical axis respectively.

In the objective system of the microscope, an objective stigmator and objective lens are located. The objective lens forms the first intermediate lens and the objective stigmator compensates for astigmatism. An objective aperture then allows one to control the number of electrons that get to the intermediate lens. The roles of the intermediate lenses are to magnify the image further. The projector lenses then finally magnifies the central part of an image that will be projected onto the fluorescent screen in which the image is displayed. The shutter exposes the screen and the camera records the image on a sheet of white photographic film.

A FEI Tecnai F20 FEGTEM was used to obtain atomic images, at an accelerating voltage of 200 kV.

3.9.4 Sample Preparation

Cross section of the films was prepared by use of a FEI Helios NanoLab 650 Dual Beam focused-ion beam SEM for TEM analysis [3.36]. The sample prepared must be extremely thin such that it is transparent to electrons for TEM analysis.

The first step of preparation is loading the sample and the omniprobe grid in its specified holder. This process is extremely time consuming, lasting for more than four hours in some cases for preparation of one sample. The benefits attained from FIB prepared samples for TEM are that there is an absence of mechanical damage, location specific accuracy and the ability to isolate small regions within a bulk material, of a few nanometres in size [3.36].

The preparation of a TEM sample using FIBSEM is as follows [3.37];

Once the sample is loaded a rectangular shape of Carbon (C) is deposited on the region of interest on the surface of the sample. The sample is inserted at a 52° angle. A cross section pattern is then milled, using a Gallium (Ga) ion beam along either side of the length of the rectangular C deposited region. The patterned cross section is cleaned and removed from the

bulk by a U-cut incision made by the Ga ion-beam. Once the cross section has been cut it must now be lifted out. C is deposited on the edge of the cross section; using the omniprobe the cross section is raised. The omniprobe is moved back to eucentric height. The cross section now needs to be transported to the grid holder. The grid holder is brought to eucentric height and the cross section is positioned in the demarcated region (A, B, C, D) on the grid holder. Once the sample cross section is secured on the grid holder it then undergoes a process of thinning. The three step thinning process reducing the width of the cross section on either side of the rectangular shaped cross section. The final step prior to imaging of the prepared sample is cleaning. The sample is cleaned using a low current ion beam < 350 pA.

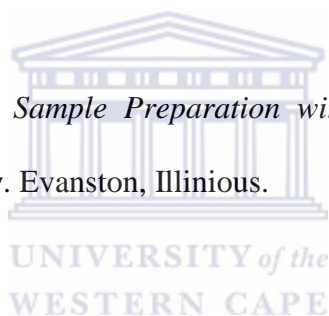


References

- [3.1] J. Mullerova, J Mudron (2000) *Acta. Physica. Slovaca.* 40, 4, p477.
- [3.2] A. Shah (2010) *Thin film silicon solar cells.* CRC Press. Italy. p35-43.
- [3.3] J. Tauc, A. Grigorovici, A. Vancu (1966) *Phys. Status Solidi.*15, 627.
- [3.4] R.H Klazes, MHL. Van der Broek, JB. Bezemer and Radelaar (1982) *Philos. Mag. B.* 45, 377.
- [3.5] D. A. G Bruggeman (1935) *Ann. Phys.* 24,385.
- [3.6] W. Theiss and S Hilbrich (1997) *Properties in porous silicon, edited by Leigh Canham,* INSPEC, The Institute of Electrical Engineers.
- [3.7] S.K O'Leary, S.R. Johnson, and P.K Lim (1997) *J. Appl. Phys.* 82, 3334.
- [3.8] A. M. Brockhoff (2001) *Hydrogen-Related Modifications of Amorphous Silicon and Silicon Nitride.* Ph.D. thesis, Utrecht University, The Netherlands.
- [3.9] William H. Zachariasen (2004) *Theory of X-ray Diffraction in Crystals, Dover phoenix editions.* Courier Dover Publications, ISBN: 0486495671.
- [3.10] B. D. Cullity (1978) *Elements of X-ray Diffraction, 2nd edition,* Addison-Wesley Publishing Company Inc., USA.
- [3.11] C. Kittel (2005) *Introduction to Solid State Physics, 8th edition.* John Wiley & Sons, USA.
- [3.12] G. Dent and E. Smith (2005) *Modern Raman Spectroscopy: A Practical Approach.* John Wiley & Sons Ltd., England.
- [3.13] P.A. Temple and C.E. Hathaway (1973) *Phys.Rev.B.*7, 3685.
- [3.14] D. Beeman, R. Tsu and M.F. Thorpe (1973) *Phy. Rev. B.* 32, 874.
- [3.15] A.J.M Bersten (1993) *Structural Disorder of Pure and Amorphous Silicon.* Ph.D. Thesis. University of Utrecht, The Netherlands.

- [3.16] W.S. Lau (1999) *Infrared characterisation of microelectronics*. World Scientific, Singapore.
- [3.17] C.J. Arendse (2002) *Hydrogenated Amorphous Silicon Thin Films*. PhD Thesis. University of the Western Cape, South Africa.
- [3.18] T.F.G. Muller (2009) *Optical model of amorphous and Metal Induced Crystallized silicon with an effective medium approximation*. PhD thesis. University of the Western Cape.
- [3.19] A.A Langford, M.L Fleet and B.P Nelson (1992). The American physical society.45, 23, 367.
- [3.20] H.R Shank, F.R Jeffrey and M.E Lowry (1981) Journal de Physique.4, 77.
- [3.21] H.R Shank (1980) Phys. Status. Solidi B. 110,43.
- [3.22] A.A Langford, M.L Fleet and B.P Nelson (1992) Phys. Rev. B. 45, 23, p367–377.
- [3.23] C.L. Fang *et al* (1980) Journal Non-Cryst. Solids.35.
- [3.24] Sherman Hsu (1997) *Handbook of Instrumental Techniques for Analytical Chemistry*, edited by F. Settle. Prentice Hall PTR. New Jersey.
- [3.25] W.M Arnold and F. H. P. M. Habrakon (1993) Rep. Prog. Phys.65, 859.
- [3.26] L. C. Feldman and J. W. Mayer (1986) *Fundamentals of Surface and Thin Film Analysis*. North-Holland Publ., Amsterdam.
- [3.27] J. R. Tesmer, M. Nastasi, J. C. Barbour, C. J. Maggiore and J. W. Mayer (1995) *Handbook of Modern Ion Beam Materials Analysis*. Pittsburgh, Pennsylvania.
- [3.28] H. Geissel *et al* (1983) Nucl. Instrum. Methods. 215, 329.
- [3.29] G. Binnig, H. Rohrer, C. Gerber, E. Weibel (1982) Phys. Rev. Lett. 49, 57.
- [3.30] P. Eaton, P. West (2010) *Atomic force Microscopy*. OUP Oxford ISBN: 0131576670.
- [3.31] N. Yao, Z.L Wang (2005) *Handbook of microscopy for Nanotechnology*.

- [3.32] M.T. Postek, K.S. Howard, A H. Johnson and K.L. McMichael (2001) *Scanning electron microscopy-a student handbook*. Ladd Research Industries, Vermont.
- [3.33] University of Iowa state (2013) Scanning electron microscopy <http://cmrf.research.uiowa.edu/scanning-electron-microscopy>. 16 May 2013.
- [3.34] D. Chescoe, P. J. Goodhew (1984) *The Operation of the Transmission Electron Microscopy*, Royal Microscopical Society and Oxford University Press, New York.
- [3.35] P. J. Goodhew, J. Humphrey, R. Beanland (2001) *Electron Microscopy and Analysis – Third Edition*, Taylor and Francis, London.
- [3.36] L.A Giannuzzi and F.A. Stevie (2005) *Introduction to focused ion beams; instrumentation, theory, technique and practice*. Springer. ISBN: 9780387231167. p173-228.
- [3.37] B. Myers (2009) *TEM Sample Preparation with the FIB/SEM*. NUANCE Centre, Northwestern University. Evanston, Illinois.



CHAPTER FOUR

STRUCTURAL AND OPTICAL PROPERTIES OF SILICON THIN FILMS

4.1 Introduction

The capability of depositing device quality thin films at low operation temperatures are sought after, as this would largely reduce production costs of semi-conductor materials. Hot-wire chemical vapour deposition (HWCVD) is one of the most promising techniques for the manufacturing of device-quality silicon thin films. This technique shows promise as a low cost, repeatable route to thin film production [4.1]. With this technique; the substrate temperature and hydrogen dilution are the two crucial deposition parameters to consider for the deposition of hydrogenated nanocrystalline silicon (nc-Si:H) thin films [4.2, 4.3]. These parameters will play a pivotal role towards controlling the properties of thin films. Hydrogen dilution has been found to have positive effects on the structural order within thin films [4.4], as described by the selective etching growth model [4.5, 4.6]. Furthermore C. Das *et al.* showed that the increase in substrate temperature can lead to phase transitions from amorphous to microcrystalline Si[4.7]. Moreover, the effects of temperature on thin film growth are brought forth by the chemical annealing growth model [4.8, 4.9].

Silicon thin films, obtained by either dynamically increasing or decreasing hydrogen dilution during deposition, were deposited by hot-wire chemical vapour deposition, in the stride to achieve a change in structural and optical properties with thin film depth. However prior to investigating this matter, each deposition regime used in the later study will be investigated independently in this chapter. Therefore, this chapter aims to provide insight into the structural and optical properties of the silicon thin films deposited at specific deposition conditions.

4.2 Experimental Details

4.2.1 Sample preparation

Six (6) thin films were deposited by hot-wire chemical vapour deposition technique with the deposition pressure kept constant at 60 μ bar and the filament temperature set to 1600 $^{\circ}$ C. A 99% pure tantalum (Ta) filament, placed in parallel, was used to catalytically dissociate the silane (SiH_4) and hydrogen (H_2) precursor gas. The flow rate and deposition time varied with each sample (Table 4.1). No substrate heating was applied during deposition in an attempt to obtain nanocrystalline silicon with minimum heat. The samples were deposited simultaneously on Corning 7059 glass and $\langle 100 \rangle$ c-Si substrates to meet the requirements of the various characterisation techniques used. The hydrogen dilution ratio shown in table 4.1 is defined as

$$f = \frac{\Phi_{H_2}}{(\Phi_{H_2} + \Phi_{SiH_4})}, \text{ where } \Phi \text{ denotes the gas flow rate.}$$

Table 4.1 Deposition parameters for the 6 thin films

Deposition Regime	Hydrogen dilution ratio (f)	Deposition time (minutes)	Φ_{SiH_4} (sccm)	Φ_{H_2} (sccm)
1	0	2	3.00	0.00
2	0.50	3	3.00	3.00
3	0.66	5	3.00	6.00
4	0.80	8	3.00	12.00
5	0.90	10	3.00	27.00
6	0.95	5	1.50	28.50

4.2.2 Characterisation Techniques

To obtain detailed information on the bonding structure within these thin films, Fourier transform infrared (FTIR) absorption spectra were collected in transmission geometry from 400 – 4000 cm^{-1} with a spectral resolution of 1 cm^{-1} , using a Perkin-Elmer Spectrum 100 FTIR spectrophotometer. The total bonded hydrogen concentration was estimated from the integrated absorption of the 640 cm^{-1} peak associated with the rocking mode of SiH using procedures reported by Brodsky *et al.* and Shank *et al.* [4.10, 4.11]. Elastic recoil detection (ERD) analysis was piloted using a 3 MeV mono-energetic and collimated beam of $^4\text{He}^+$ ions, with a 30° H recoil detection angle with respect to the incident ion beam. The total hydrogen concentration as a function of depth was obtained from the ERD spectrum. The Raman measurements were performed in a range of 100 to 700 cm^{-1} . The measurements were performed using a 514.5 nm argon (Ar) ion laser line [4.13]. X-ray diffraction (XRD) was performed using a PANalytical Xpert diffractometer at 2 θ -values ranging from 5 – 90°, with a step size of 0.02°. X-Rays emission from the Copper (Cu) $K\alpha_1$ was used as the x-ray source with a wavelength of 1.5406 Å. The surface morphology was investigated using a ZEIS Auriga high resolution scanning electron microscope (SEM) at an accelerating voltage of 1 kV and elemental composition was determined

by energy dispersive spectroscopy (EDS) at an accelerating voltage of 10 keV. Surface morphology studies were investigated using the Nanoman 5 Veeco AFM 3100 atomic force microscope (AFM) in the tapping mode, with a resolution of 1.5 μm , scan rate of 0.96 Hz and a scan angle at 45°.

Optical reflection spectra were measured using a Semiconsoft mProbe UV-Visible photometer in the range 200 – 1000 nm with a spectral resolution of 1 nm. The refractive index, absorption coefficients and optical thickness were calculated by employing the Looyenga effective medium approximation (LEMA) model [4.12].



4.3 Results and Discussion

4.3.1 Structural Properties

The flow rate of precursor gas, the effective dissociation of precursor gas into its atomic species, substrate temperature and the total deposition time are all factors which will affect the deposition rate and ultimately the thin film thickness obtained. The deposition rate (r_d) is defined as the ratio of the total thickness (d) of the deposited film and the deposition time (t) according to:

$$r_d = \frac{d}{t} \quad (4.1)$$

The effects of H₂ dilution ratio (f) on the deposition rate is shown in figure 4.1. The thin film thickness was determined by using optical modelling which will be discussed later.

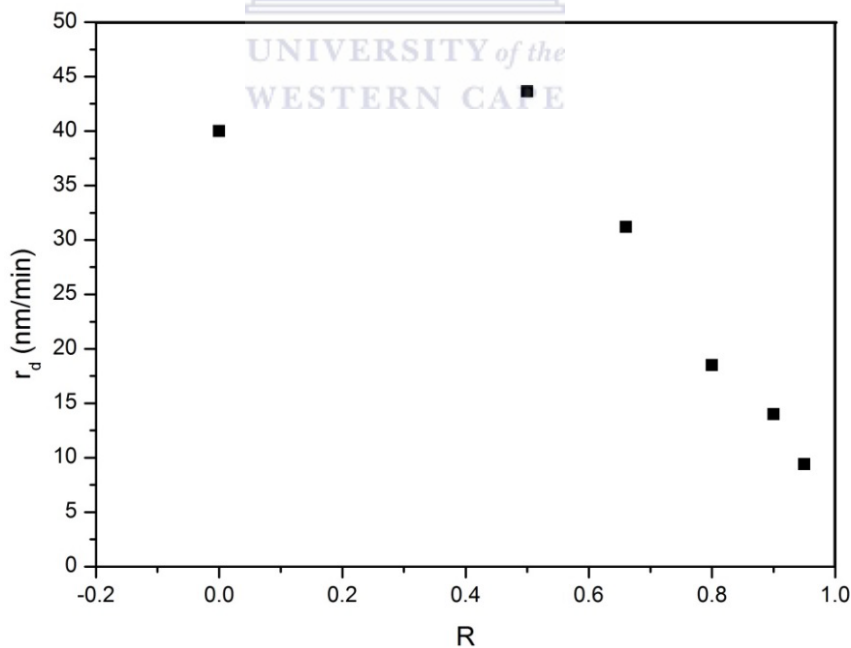


Figure 4.1 Thickness evolutions with H-dilution ratio

Feenstra *et al.* concluded that substrate heating decreases the deposition rate due to the kinetic energy attained by the atoms, which reduce their sticking coefficient [4.2]. Since these samples

were deposited with no substrate heating no hindrance should be posed to the sticking capabilities of the growth material. When H_2 dilution is introduced into the gas mixture a linear decreasing trend was observed with the deposition rate. In this study for each deposition, the ratio of hydrogen (H_2) to silane (SiH_4) increases with deposition time. With the increase in H_2 dilution, more atomic hydrogen, as inferred by the selective etching growth model, results in the etching of the growing thin film surface. We suggest that the change in deposition time and improved sticking coefficient could not compensate for the etching effect of atomic hydrogen. This property competes with the growth of new material, removing and breaking bonds both on the surface and subsurface of the thin film, resulting in the decrease in deposition rate.

Confirmation of thin film crystallinity is pivotal to understanding the nature of the thin films at hand. X-ray diffraction was used to determine the degree of crystallinity of the silicon thin films. [4.14].

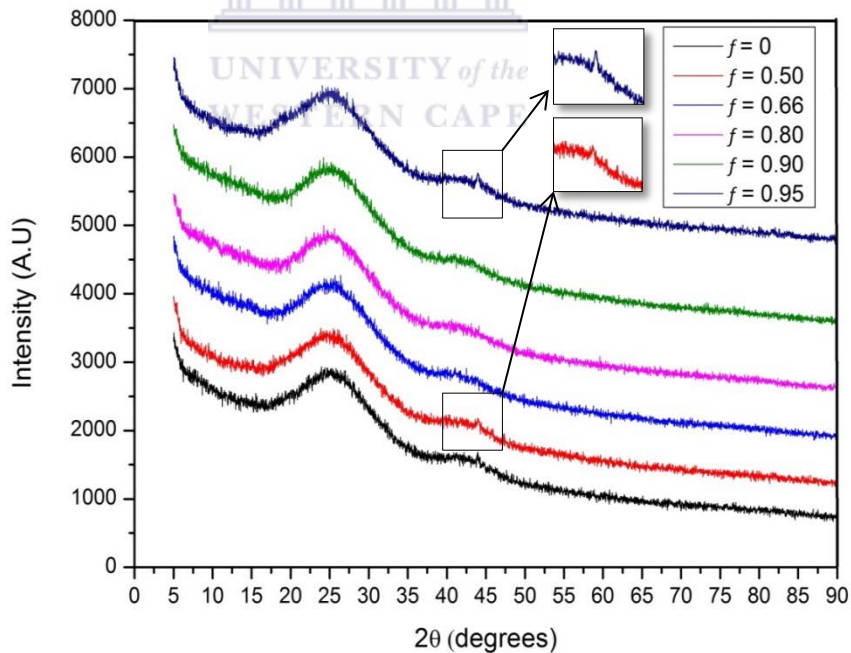


Figure 4.2 XRD spectra for each deposition

An XRD spectrum for each sample is shown in figure 4.2. The XRD spectra show no evolved crystalline silicon (c-Si) peaks, implying an amorphous nature to the thin films. A marginal peak

emerges from samples deposited at $f = 0.5$ and 0.95 at $2\theta \sim 44.03^\circ$. Crystalline silicon has its (002) diffraction plane at 43.55° and a tantalum (Ta) (200) diffraction peak is expected around 44.83° . Ta contamination is usually only seen at operating filament temperatures above 2100°C [4.15, 4.16]. To explore the possibility of Ta contamination during thin film deposition, energy dispersive spectroscopy (EDS) was employed to obtain quantification on the elemental composition of samples deposited at $f = 0.5$ and 0.95 . As can be seen from the EDS spectra in figure 4.3, no Ta contamination was detected.

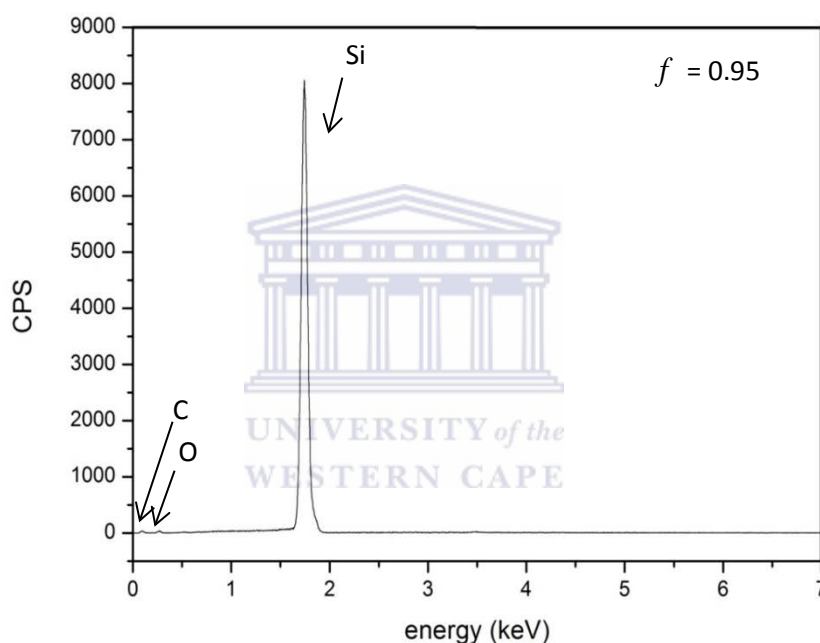


Figure 4.3 EDS elemental composition quantification spectrum for sample $f = 0.95$

Thus the peak seen for $f = 0.5$ and 0.95 is therefore the (002) diffraction peak for Si. The (002) diffraction peaks arises when silicon has a hexagonal phase structure [4.17]. The (111), (220) and (311) diffraction peaks are usually the dominant peak seen in XRD patterns of cubic structured silicon material.

To further investigate the structure and order of these films, Raman spectroscopy was employed to detect crystallites much smaller than the capabilities of XRD, attributable to the extreme

sensitivity by the Raman technique to changes in the short range order. The Raman spectra are shown in figure 4.4.

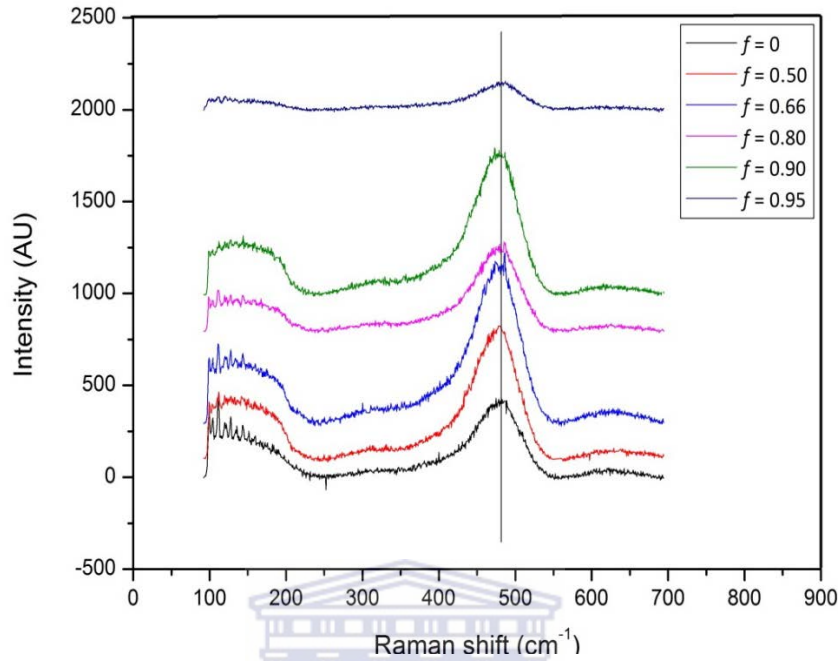


Figure 4.4 Raman spectra of each sample deposited from $f = 0$ to $f = 0.95$

For quantitative analysis, the Raman scattering spectra were deconvoluted by fitting three Gaussians, namely the longitudinal acoustic (LA) mode centred at 330 cm⁻¹, the longitudinal-optic mode (LO) centred at 445 cm⁻¹ and the transverse-optic (TO) mode centred at 480 cm⁻¹. The resultant deconvoluted spectra can be seen in figure 4.5 below. A c-Si TO mode centred at 520 cm⁻¹ will emerge if the samples possess a crystalline nature. The peak observed at 650 cm⁻¹ is assigned to Si-H_x vibrations.

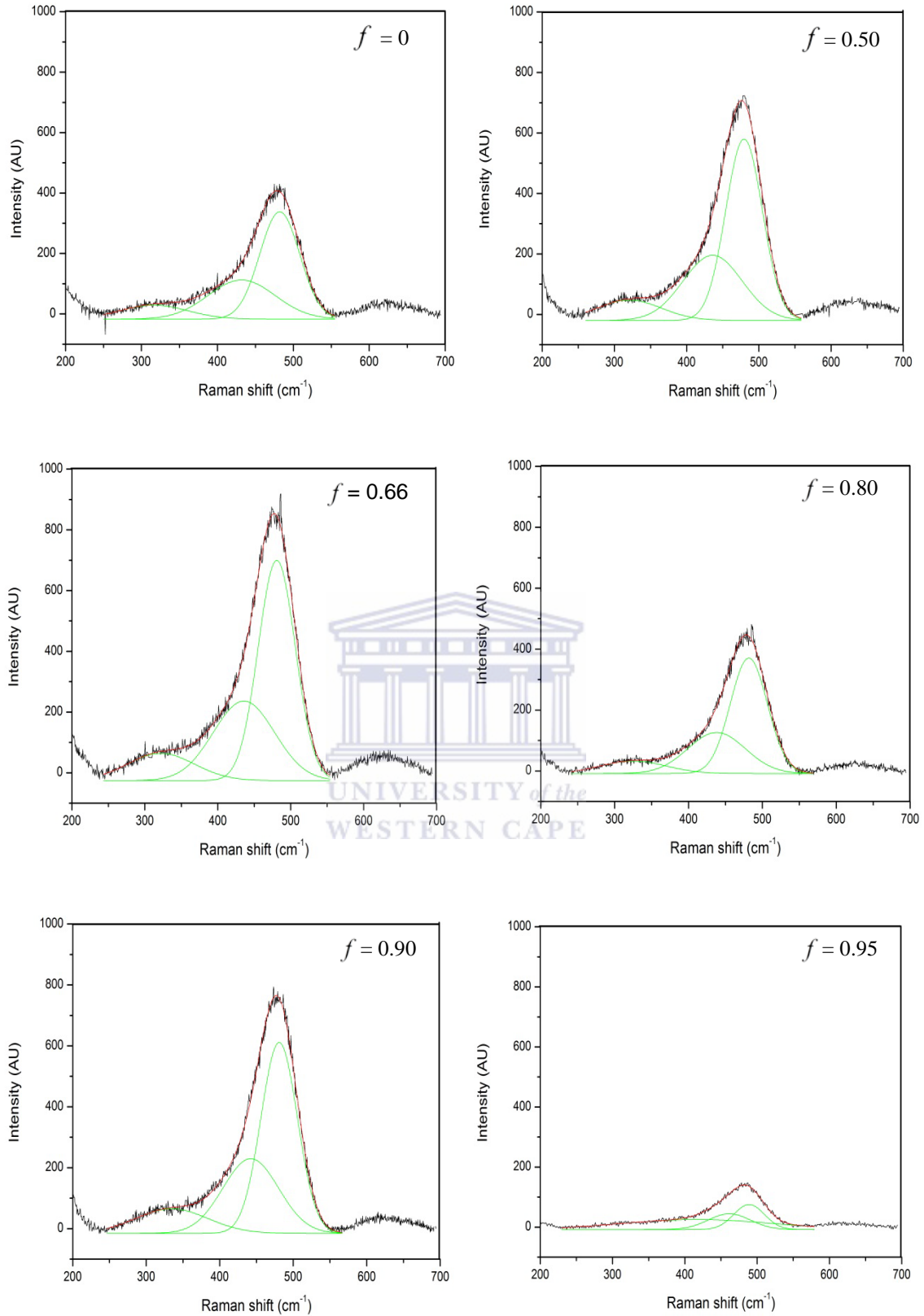


Figure 4.5 Deconvoluted Raman spectra for samples deposited in each regime (Green solid lines are the two fitted Gaussian peaks, Red solid line is the peak sum).

No evident c-Si TO mode is present in any of the deconvoluted Raman spectra for the deposited samples, confirming that the thin films are amorphous. The lack of crystallinity was due to the absence of substrate heating, which prohibits crystalline grain nucleation occurring within the short deposition times as proposed by the chemical annealing growth model [4.18].

Furthermore Raman analysis provides information on the root mean square (rms) bond angle variation ($\Delta\theta_b$) based on the width of the amorphous TO peak centred around 480 cm^{-1} [4.19], by the following relation [4.20] (where $\Gamma/2$ is the half-width-half-maximum):

$$\frac{\Gamma}{2} = 7.4 + 3.2 \Delta\theta_b \quad (4.2)$$

The $\Delta\theta_b$ of a-Si:H thin films are considered to have maximum order within the range $7^\circ - 8.2^\circ$ [4.20]. The thin films become more ordered with the increase in H_2 dilution as can be seen in table 4.2. The $\Delta\theta_b$ of the thin films are within the range of maximum order for $f = 0$ to 0.90 and fascinatingly, at $f = 0.95$, the sample has exceeded the expected maximum structural order seen for a-Si:H.

Table 4.2 Structural properties determined by Raman analysis of the bond angle variation and half-width-half-maximum.

f	$\Delta\theta_b$ ($^\circ$)	$\Gamma/2$ (cm^{-1})
0	7.77	30.81
0.50	7.48	29.94
0.66	7.46	29.89
0.80	7.33	29.49
0.90	7.23	29.21
0.95	5.69	24.58

Previous studies indicate that strain energies in a-Si:H are proportional to $\Delta\theta_b$ [4.21], in that a decreasing $\Delta\theta_b$ allows relaxation of the stored bond angle distortion energy in the amorphous network. The increased presence of atomic hydrogen, due to hydrogen dilution, promote the etching property and removes these strained bonds and passivate dangling bonds, therefore resulting in the relaxation of the bond angle distortions and an highly ordered structure.

4.3.2 Hydrogen Configuration

Since the role played by hydrogen defines factors such as film quality, structural order and hydrogen content, knowing the bonding configuration becomes imperative. Fourier transform infrared spectroscopy (FTIR) is then the perfect tool to investigate the bonding configuration within these thin films.

The FTIR absorption spectra for each sample are displayed in figure 4.6. Three bonding modes are identified from the FTIR absorption spectra; the rocking mode at 640 cm^{-1} , bending mode at the $800 - 1000\text{ cm}^{-1}$ region, and the stretching mode around $2000 - 2100\text{ cm}^{-1}$. The rocking mode is attributed to all Si-H bonding configurations present in the thin film. The bending and the stretching modes are indicative of the presence of the $(\text{Si-H}_2)_n$ bond, where $n = 1,2,3$ [4.22]. Furthermore the stretching mode is also attributed to Si-H bonded on the surface of voids and isolated Si-H bonds. No Si-O vibrational mode is seen at 1100 cm^{-1} in any of the samples, indicative of an un-oxidized sample. These bonding modes were quantitatively analysed by deconvoluting the spectra into five Gaussians.

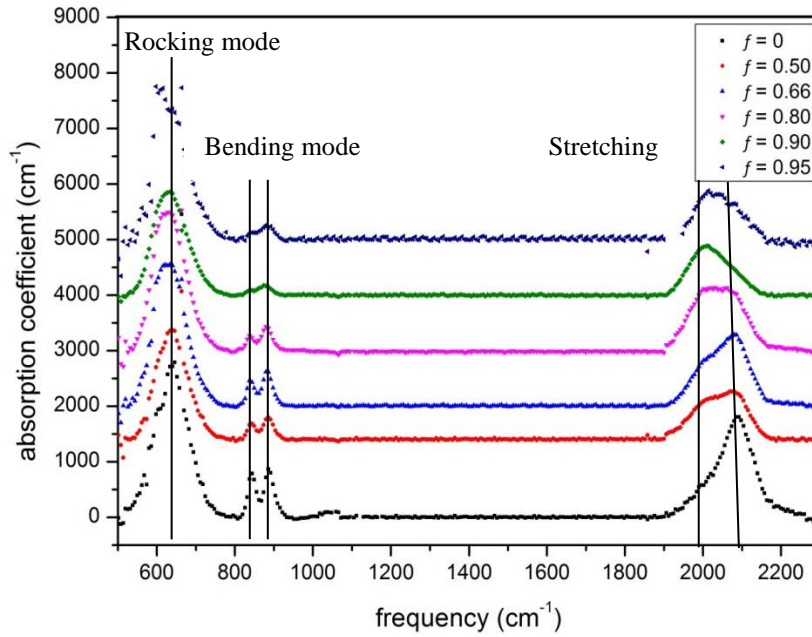
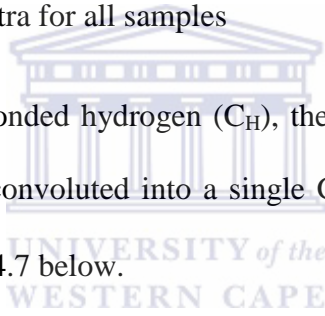


Figure 4.6 FTIR Absorption spectra for all samples

To obtain the concentration of bonded hydrogen (C_H), the integrated absorption of the rocking vibrational mode is used and deconvoluted into a single Gaussian peak centred at a frequency $\sim 630 \text{ cm}^{-1}$ as illustrated in figure 4.7 below.



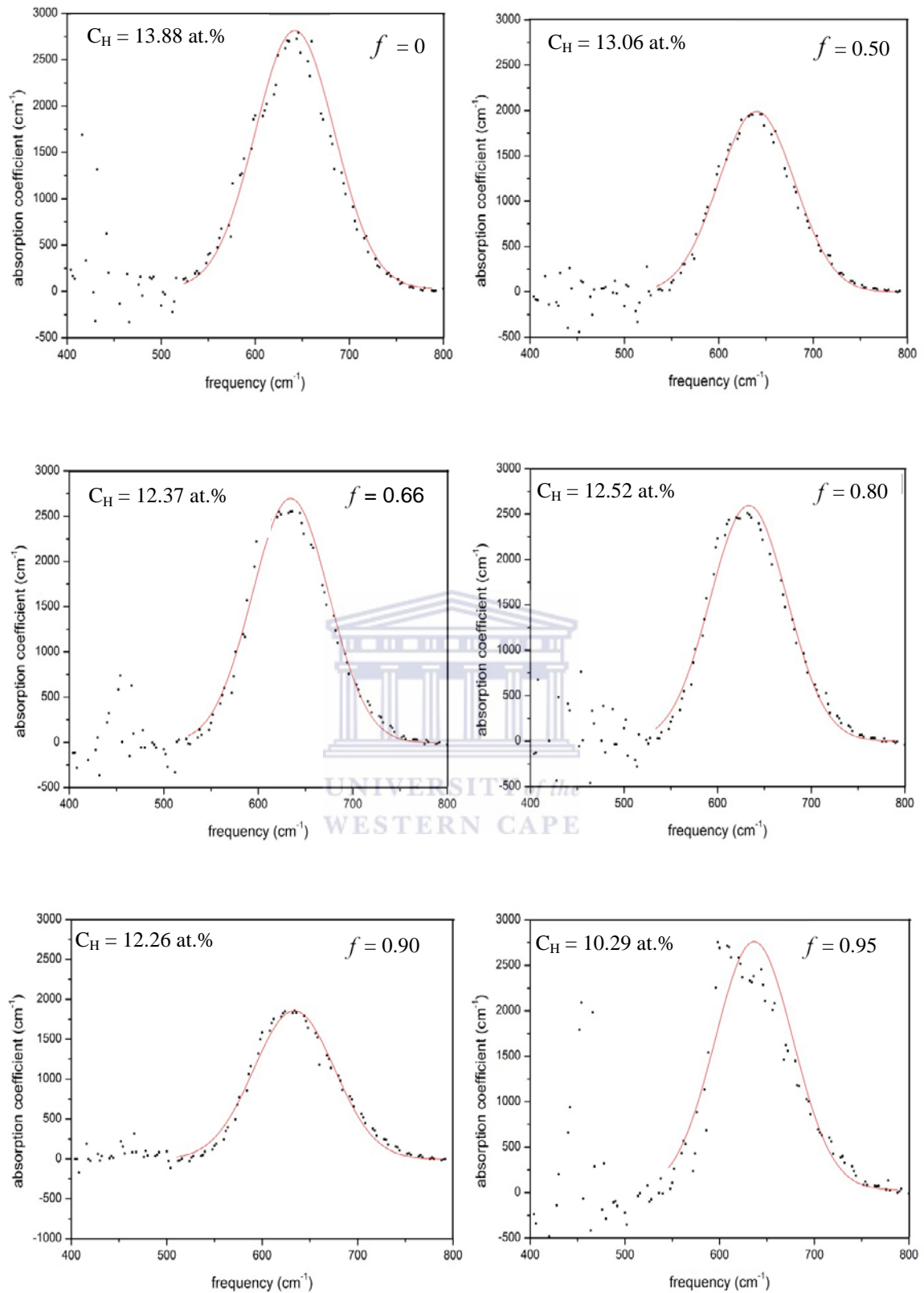


Figure 4.7 Deconvoluted rocking vibrational mode where the red solid line is Gaussian peak fitted.

The C_H was calculated by employing equation (2.26), discussed in chapter 3, using the proportionality constant $A_{640} = 1.6 \times 10^{19} \text{ cm}^{-2}$ as determined by Shank *et al.* and displayed on the insets of figure 4.6. Literature shows that an increase in H_2 dilution leads to a decrease in C_H [4.23]. This trend is observed in this study despite the variation in deposition time that accompanied the change in H_2 dilution. Figure 4.8 demonstrates a correlation between bond angle variation and bonded hydrogen concentration. The linear relation, seen between C_H and $\Delta\theta_b$, infers an improvement in structural order of the thin films with the decrease in C_H .

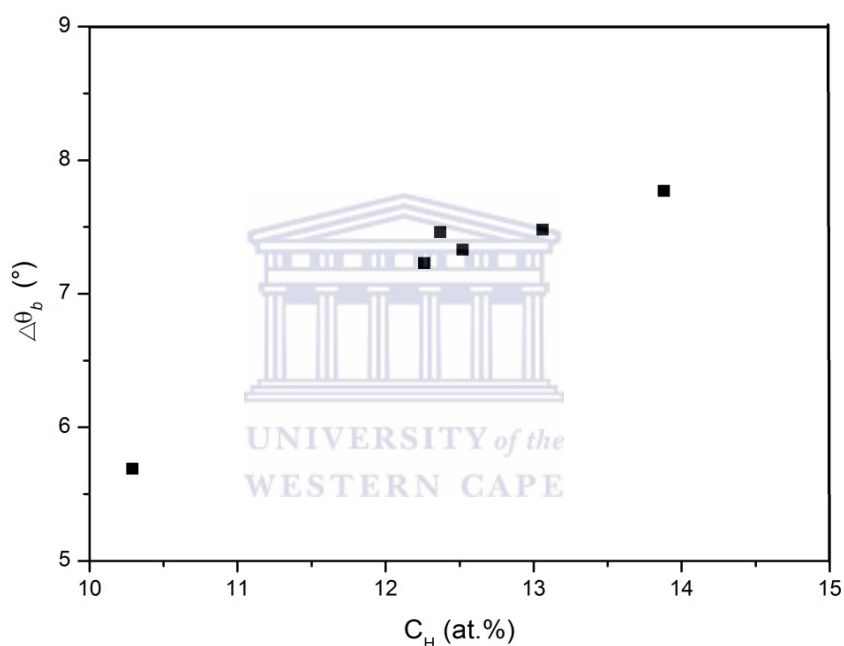


Figure 4.8 Graph of the relation between bond angle variations, determined by Raman analysis, and bonded hydrogen concentration obtained from FTIR.

The stretching mode, seen in figure 4.9, shows the existence of both a 2000 cm^{-1} vibration mode and a $2090 - 2100 \text{ cm}^{-1}$ vibration mode. The stretching mode has been deconvoluted according to these two vibrational modes. These vibrational modes are assigned to isolated Si-H bonds at 2000 cm^{-1} and the $2090 - 2100 \text{ cm}^{-1}$ mode is attributed to $(\text{Si-H}_2)_n$ bonds and Si-H bonded on the surface of voids.

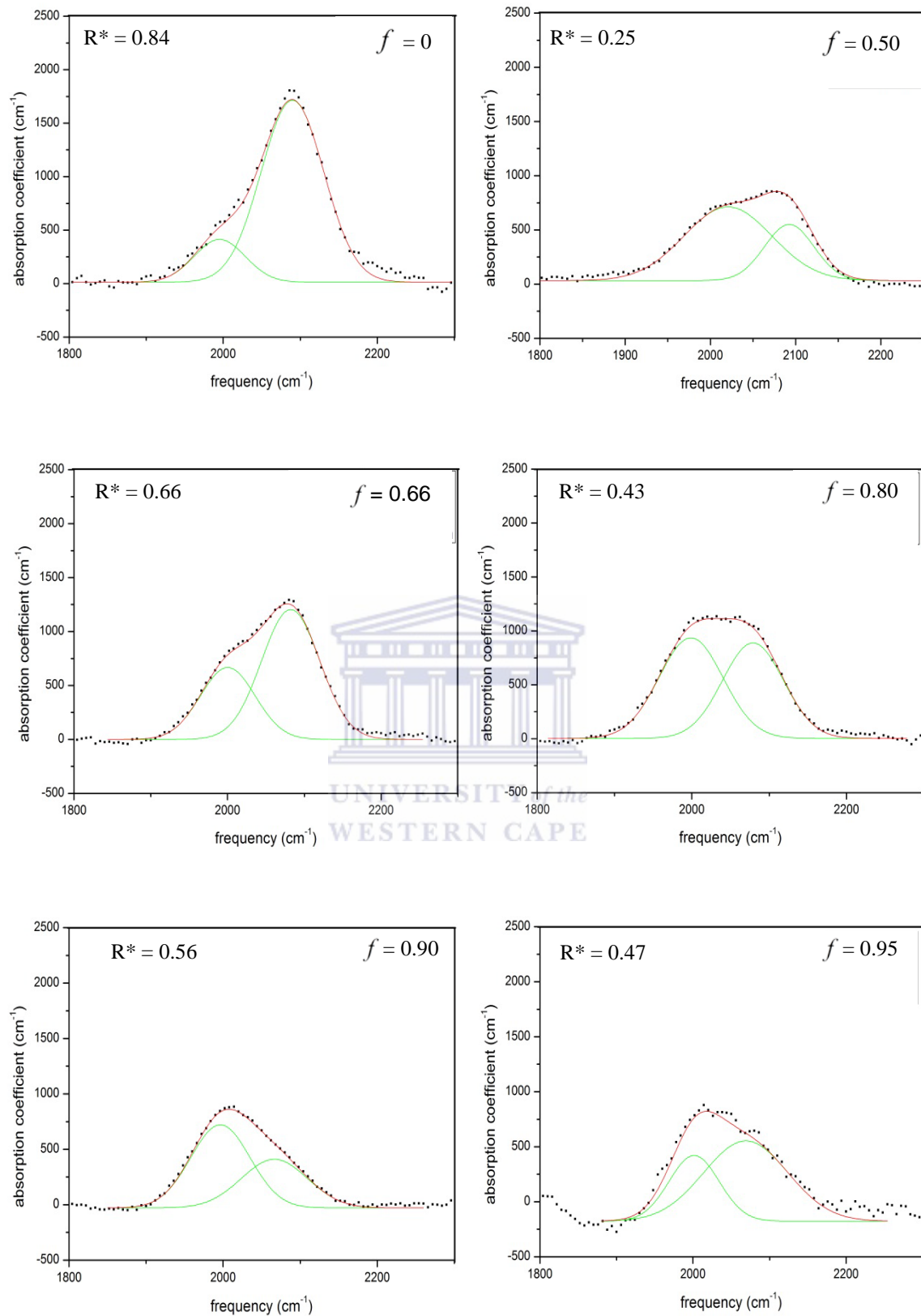


Figure 4.9 Deconvoluted stretching mode into two Gaussians at frequencies 2000 and 2100 cm⁻¹. (Green solid line are two fitted Gaussian peaks, Red solid line is the peak sum).

The two characteristic peaks of the stretching mode provides useful information on the microstructure factor (R^*) of a thin film using the ratio given in chapter 3, equation (2.27). With an increase the 2100 cm^{-1} mode contribution, the microstructure parameter increases which is indicative of poor quality material [4.24]. The microstructure factors for each deposited thin film are given on the inset of each spectrum in figure 4.8 above.

Uncharacteristically large R^* values were determined for the series of thin films, with the largest R^* observed at $f = 0$. With such large R^* values, a highly disordered structure is expected with $\Delta\theta_b$ ranging between 11 and 13° , which is not seen here. The R^* values for all samples exceed 20% , indicative of a porous and relatively inhomogeneous sample structure [4.25, 4.26], which is attributed to the lack of substrate heating during depositions.

Due to the unfavourable microstructure, suggested by the R^* values for these thin films, specific interest is now paid to the possibility of void effects responsible for this behaviour. The existence of voids within the samples leads to an enhancement of the stress inside the a-Si:H layer [4.27, 4.28]. Since thin a-Si:H are layers is more prone to high compressive stress and high concentrations of strained Si-Si bonds, it results in an increase formation of SiH_n complexes, [4.29, 4.30]. The presences of these SiH_n complexes are immediately identifiable by the manifestation of the bending mode in the FTIR absorption spectra, seen in figure 4.10 below.

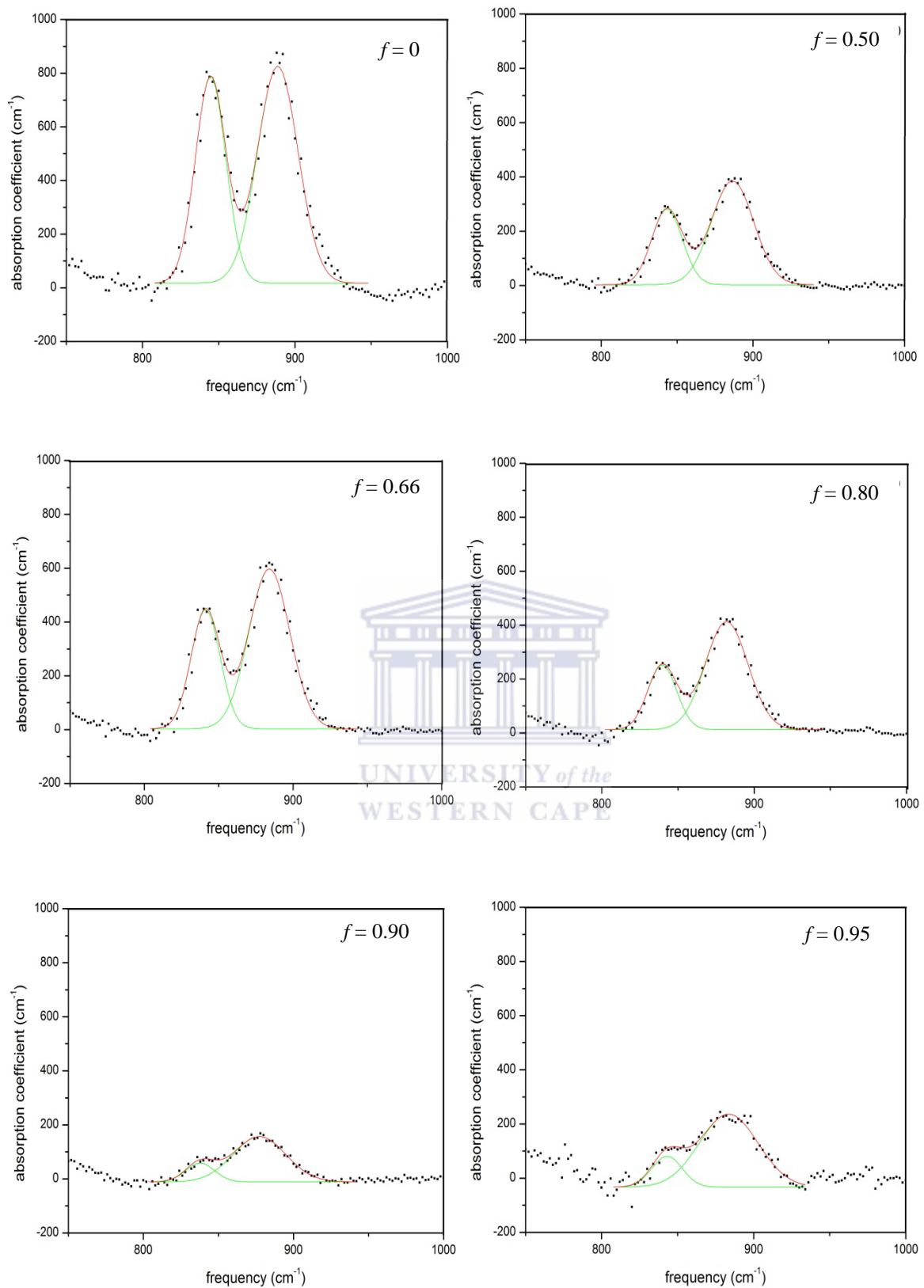


Figure 4.10 Deconvoluted bending vibrational mode into two Gaussians at frequencies 840 and 890 cm⁻¹. (Green solid line are two fitted Gaussian peaks, Red solid line is the peak sum).

To explore the presence of voids we consider the concentration of hydrogen within the 2100 cm^{-1} mode. This vibrational mode consists of Si-H bonded on the inner surface of voids and polyhydrides, which also give rise to the bending mode. We therefore deduce the following equation to be indicative of the concentration of hydrogen bonded on voids within the thin film;

$$C_{H2100} = C_{Hbending} + C_{Hvoids} \quad (4.3)$$

The concentration of hydrogen present in the 2100 cm^{-1} mode is the summation of the hydrogen concentrations on the inner surface of voids and hydrogen bonded in the bending mode.

Thus;

$$C_{Hvoids} = A_{2100}I_{2100} - A_{bending}I_{bending} \quad (4.4)$$

where $A_{bending}$ is given as $2 \times 10^{20}\text{ cm}^{-1}$ by Shanks *et al.* [4.31].

Figure 4.11 illustrates the relation between the thin film microstructure factor and the concentration of hydrogen bonded in voids. The increase of the structural inhomogeneity correlates to an increase in C_{Hvoids} , up to 12 at.%. We suggest that as a result of the extreme H-dilutions at $f = 0.92$ and 0.95 , the thin films approach the transition edge between amorphous and microcrystalline, resulting in the decrease in microstructure at $R^* > 12$ at.%. The transition width between nc- and a-Si:H, determined by Strahm *et al.* was shown to depend on the input silane concentration [4.32]. The higher the silane concentration the wider the transition, thus making lower silane concentrations ideal for nc-Si:H film growth.

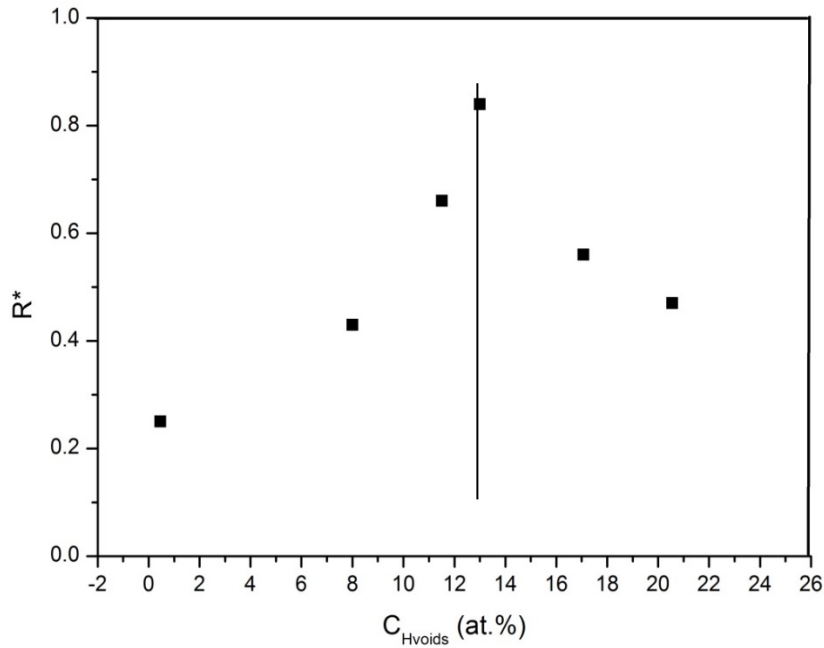
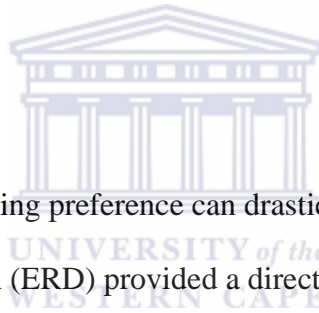


Figure 4.11 The dependence of the microstructure factor on the concentration of hydrogen bonded in voids.



The role of hydrogen and its bonding preference can drastically alter the structural properties of a thin film. Elastic Recoil Detection (ERD) provided a direct method to measure hydrogen content, complimentary to FTIR. The ERD modelled spectra are shown in figure 4.12 below. From these spectra the hydrogen is uniformly distributed throughout the thin film thickness.

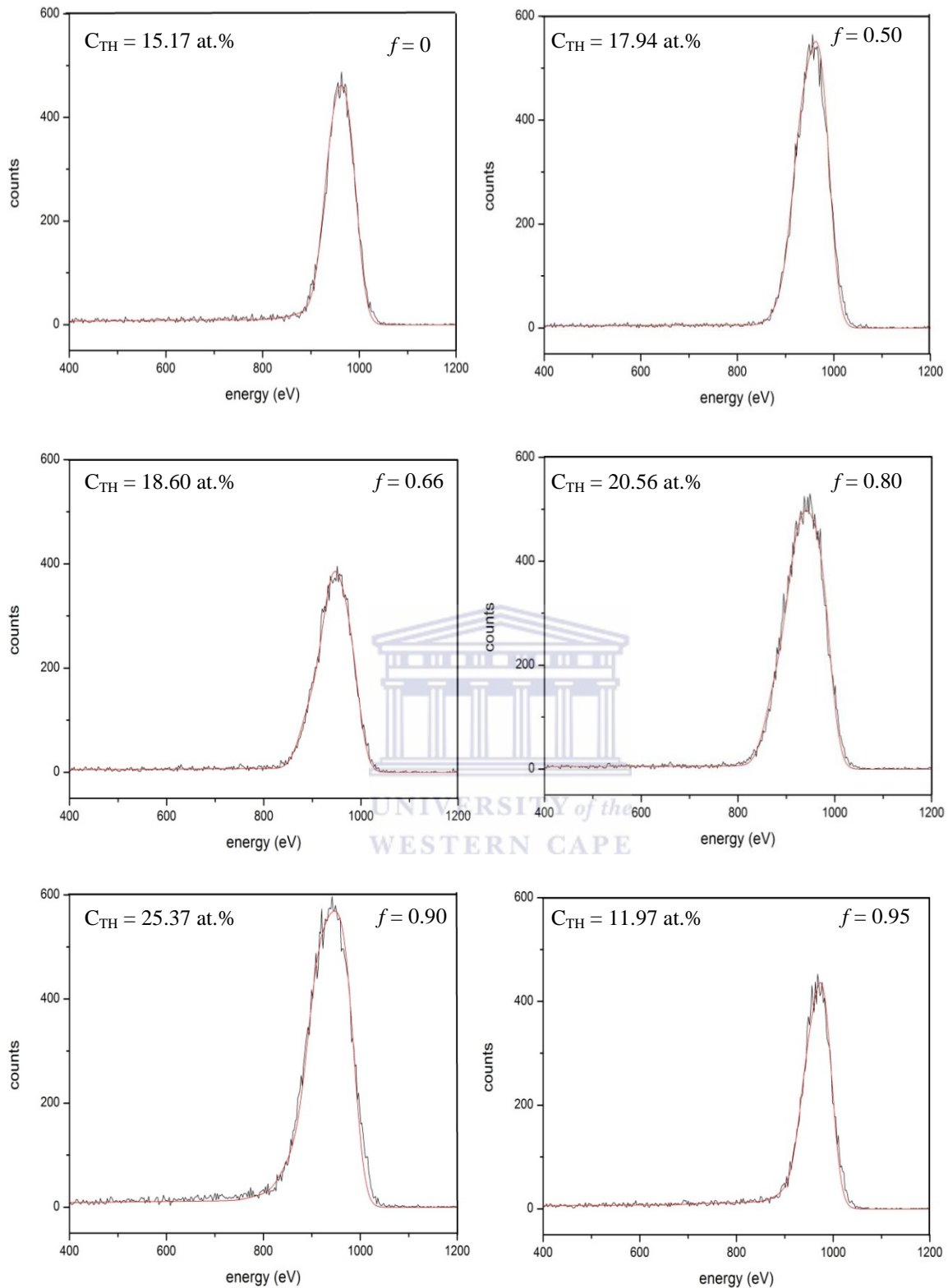


Figure 4.12 ERD modelled spectra for each sample and depth profiles displayed in the inset of the spectrum.

The total hydrogen content (C_{TH}) determined from ERD analysis are displayed on the inset of each ERD spectrum. C_{TH} takes into account both bonded hydrogen and molecular hydrogen (H_2) present in the films, hence a higher concentration of hydrogen is obtained from ERD technique compared to FTIR.

The difference between C_H and C_{TH} is indicative of the concentration of H_2 within the thin films. It is observed that the concentration of H_2 increases with f . The interaction of H atoms with a-Si:H induces the formation of H_2 by abstraction reaction [4.33,4.34] which get trapped in internal voids present in a-Si:H. The H_2 molecules, trapped in voids, puts pressure on the walls of the voids. This pressure further drives the increase in void volume fraction and its evolution within the sample [4.35, 4.36].

4.3.2 Morphology Investigation

The investigation into the surface morphology is vital for thin film studies with focused application in photovoltaics, since surface roughness can largely affect the manner in which light interacts with the thin film. Atomic force and scanning electron microscopy was employed to probe surface morphologies of the investigated thin films. Figure 4.13 displays the AFM surface images for the deposited thin films.



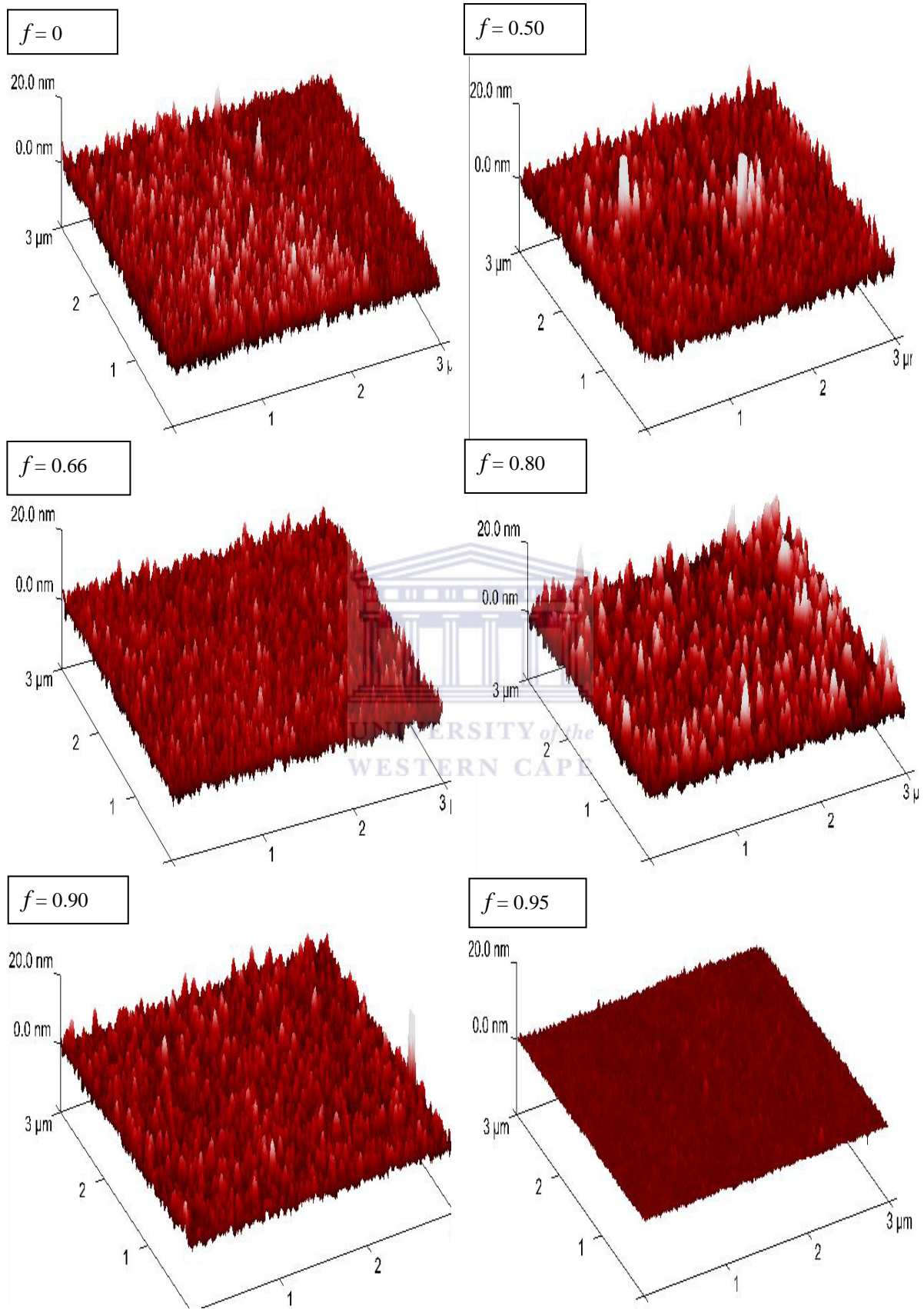


Figure 4.13 3D AFM surface images of various samples

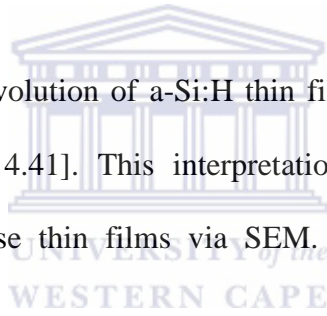
Columnar structures are observed on the surface for all the thin films. Some regions on the surface reveal tall columnar structures in comparison to the rest of the surface as seen for thin films deposited at $f = 0.50 - 0.80$. The microstructural evolution of a-Si:H thin films shows that during the growth process new growth material has a preferential attraction to existing nucleation sites on the growing surface rather than the bare substrate [4.37]. This preferential attraction results in the formation of these columnar features. Furthermore, these columnar features are indicative of a porous material as was observed by Chang-Ho Cho *et al.* [4.38]. A relatively featureless surface morphology is seen for the thin film deposited at $f = 0.95$ (figure 4.13). With a $\Delta\theta_b$ of 5.69° , the smoothening of the thin film surface is characteristic of a protocrystalline growth regime, as examined by Collins *et al.* due to enhanced nuclei coalescence [4.39].

The root-mean-square (rms) roughness is investigated in association with the H₂ dilution ratio, in table 4.5. The thin films roughness remains relatively constant for each sample except at $f = 0.95$, which has a roughness 0.5 nm. This is also attributed to the etching effect of atomic hydrogen, resulting in the lack of character on the surface, smaller bond angle variation and ultimately a decrease in thickness [4.40].

Table 4.5 Microstructural evolution of roughness and its dependence on H-dilution ratio

<i>f</i>	rms roughness (nm)
0	2.33 ± 0.02
0.50	2.40 ± 0.03
0.66	2.21 ± 0.18
0.80	2.96 ± 0.15
0.90	2.17 ± 0.21
0.95	0.59 ± 0.03

The microstructural and phase evolution of a-Si:H thin films has been deduced into 6 growth steps, by Collins *et al.* [4.39, 4.41]. This interpretation was used as a starting point to investigating the growth of these thin films via SEM. The SEM surface micrographs are displayed in figure 4.14.



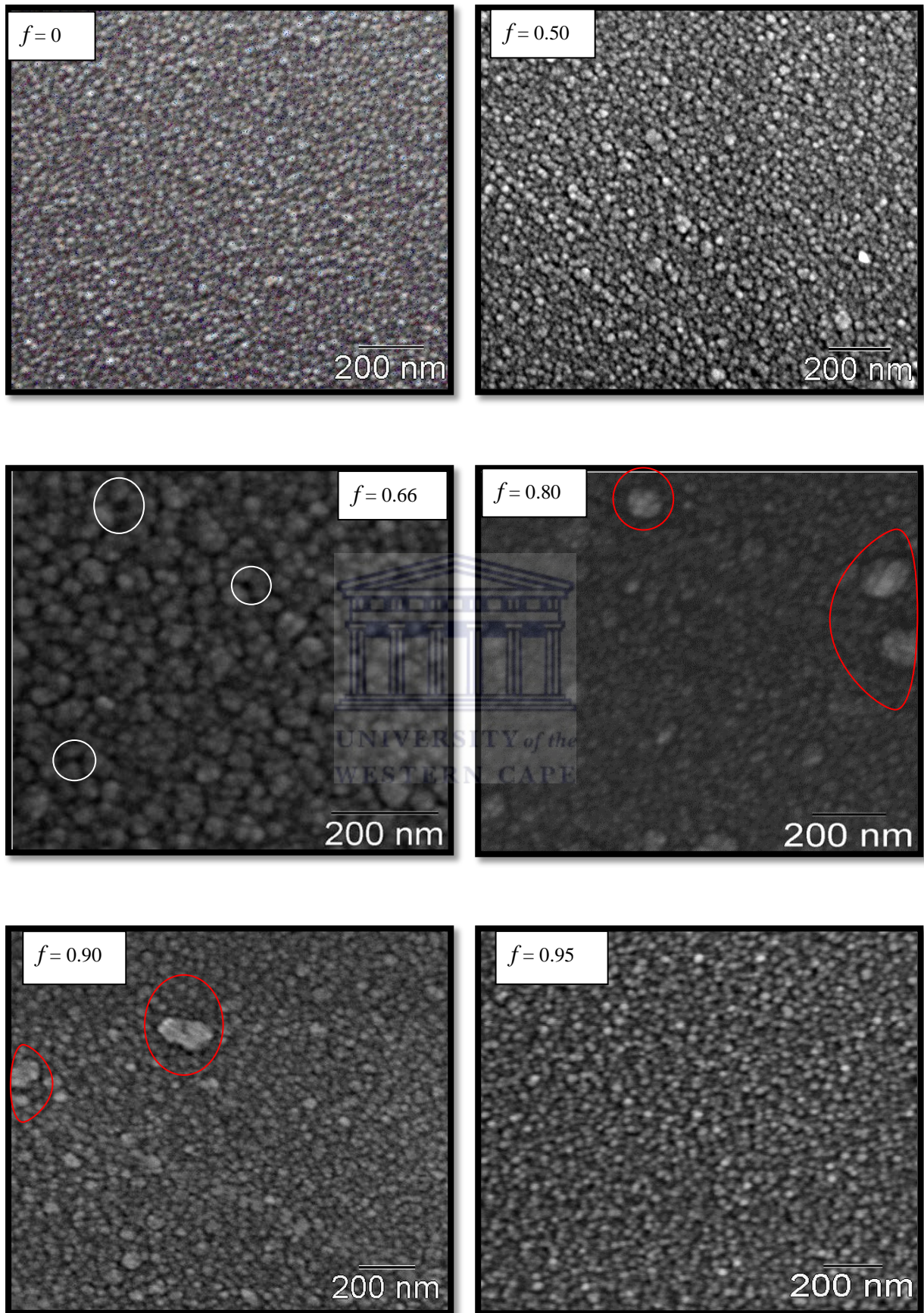
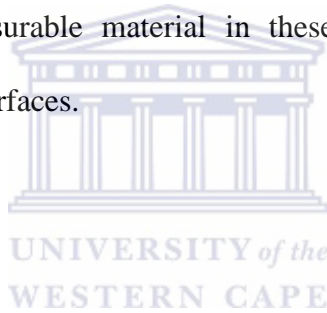


Figure 4.14 SEM micrographs of the various samples

The surface morphology, of samples deposited at $f = 0, 0.50$ and 0.95 , is one that consists of fine grained spherical features. Some large spherical-like features can be seen on the surfaces of samples $f = 0.80$ and 0.90 , (figure 4.14 red circles). These large features are randomly distributed, which may be indicative of the particles that have coalesced. This suggests that they are in the late stages of initial growth. At this stage, referred to as the amorphous-to-amorphous roughening phase transition, the initial amorphous nuclei start to coalesce and form clusters. For $f = 0.66$, the surface roughness becomes dominated by features spread out over a more lateral length scale [4.42] and mostly evinces the existence of a porous film structure, where spherically agglomerated structures are surrounded by dark regions (white circles). These dark regions are brought about when grains coalesce and leave behind vacant spaces which appear darker on the micrographs. The lack of measurable material in these vacant regions contributes to the inhomogeneity of the thin film surfaces.



4.3.3 Optical Properties

The main role of the intrinsic layer of a silicon thin film solar cell is to absorb light for the purpose of electron excitation. Therefore, the optical properties become crucial to determining the best possible film properties for a specific application.

Interference fringes in transmission spectra are directly related to the thin film thickness, where a thicker sample would yield more prominent interference fringes. These fringes make it possible to determine the optical properties of a thin film using the Swanepoel method [4.43]. When a thin film thickness is slightly tapered the interference effects diminish and results in a smoothing of the transmission spectrum as seen in figure 4.15, displaying the transmission spectra for the sample deposited at $f = 0.95$.

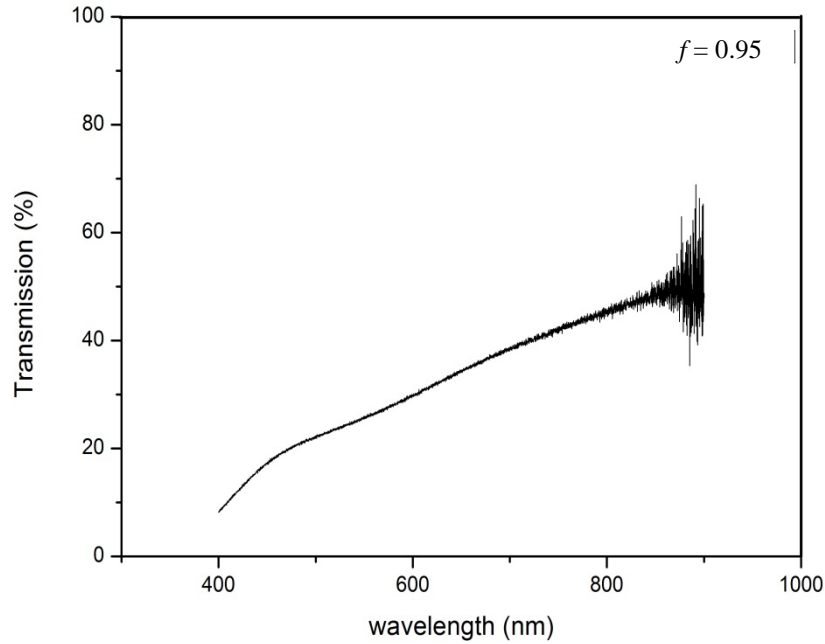


Figure 4.15 Transmission measurements for $f = 0.95$

This makes the determination of optical constants a much tougher task and the Swanepoel method less reliable. Instead, reflectance measurements were obtained for thin films deposited onto Si substrates. The refractive index, optical band gap, absorption coefficient and thickness are determined by optically modelling the UV-Vis reflection spectra. The modelled measurements were obtained using the optical model procedure stipulated in chapter 3 based on the Looyenga model.

The rating of a modelled spectra fit value is expressed as the deviation of the simulated spectra from the measured spectra. The rating can be categorized and are given in the table 4.6 below.

Table 4.6 Rating classification levels according to the deviation of the simulation from spectra.

Rating description	Excellent	Good	Acceptable	Bad	Rejected
Value	10^{-5}	10^{-4}	10^{-3}	10^{-2}	10^{-1}

The fitted spectra for all samples are illustrated in figure 4.16. The simulated spectra show the accuracy of the fit and the deviation associated with each fit was below 1.20×10^{-5} . This would be categorized as excellent simulated fits.

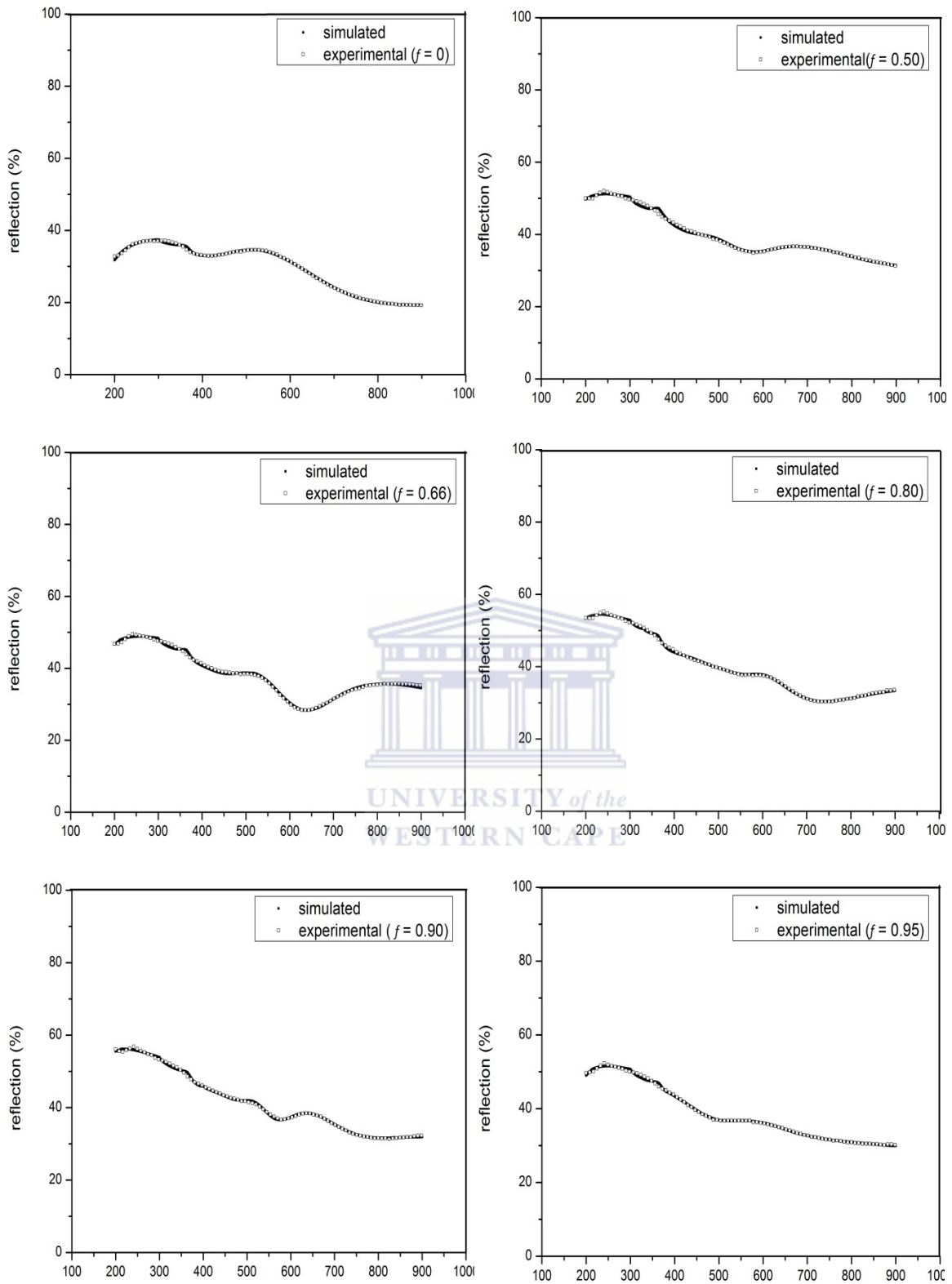


Figure 4.16 Modelled reflectance spectra for all samples

The thin films discussed in this work are not utilized for comparison or to find trends within the deposited samples. These thin films have been deposited to identify its individual properties,

retained at these specific deposition parameters. Therefore the optical properties; refractive index, void volume fraction, optical thickness, tauc optical band gap and absorption coefficient for each thin film is given in table 4.7 below.

The refractive index for the investigated samples along with the void volume fraction, optical thickness, Tauc optical band gap and absorption coefficient for each sample are given in table 4.7.

Table 4.7 Optical constants determined by Looyenga theoretical model using reflectance measurements.

<i>f</i>	Thickness (nm)	Void volume fraction	Static refractive Index (n_0)	Absorption coefficient ($\alpha_{2\text{eV}}$) ($\times 10^4 \text{ cm}^{-1}$)	Tauc optical band gap (E_g) (eV)
0.00	80.00	0.25	3.17	5.79	1.77
0.50	131.80	0.33	3.06	8.43	1.54
0.66	156.60	0.32	2.90	5.79	1.78
0.80	148.60	0.30	3.09	2.16	1.84
0.90	140.50	0.28	3.07	5.99	1.65
0.95	46.90	0.27	3.06	3.46	1.83

The optical absorption coefficient (α) spectrum provides insight into the electronic band structure. This information becomes important as it determines the spectral response of opto-electronic devices. Figure 4.17 shows the behaviour of α , for each thin film from which the absorption coefficient at energy 2 eV ($\alpha_{2\text{eV}}$) has been quoted.

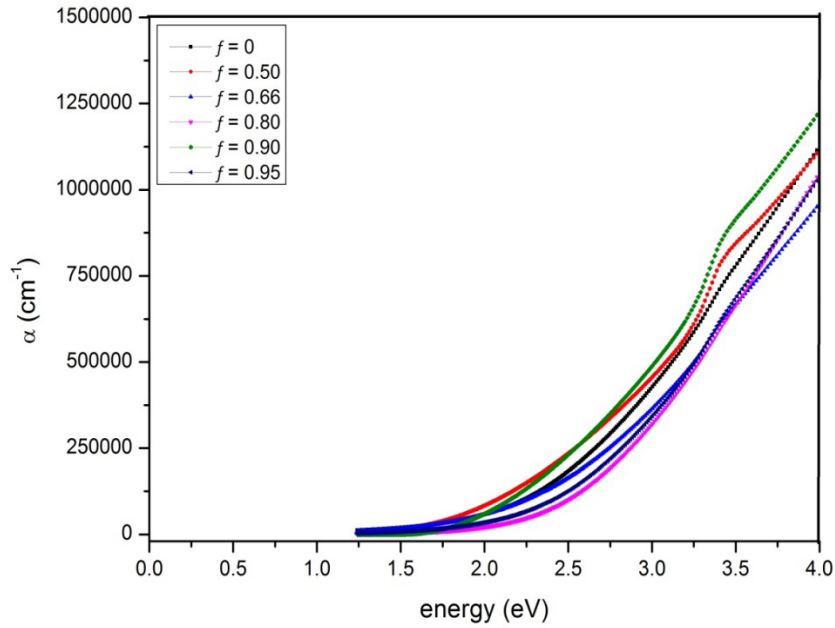


Figure 4.17 Optical absorption coefficient spectra for each thin film

A counter intuitive observation is made for the thin film with the highest $\alpha_{2\text{eV}}$, at $f = 0.50$, also has the largest void volume fraction. The E_g was determined using the Tauc model [4.44]. From the table above a direct correlation between $\alpha_{2\text{eV}}$ and the tauc optical band gap (E_g) is noted, whereby the increase in $\alpha_{2\text{eV}}$ is associated with a decrease in E_g [4.45].

The E_g was determined using the Tauc model [4.44]. The extrapolation of the Tauc curve is displayed in figure 4.18.

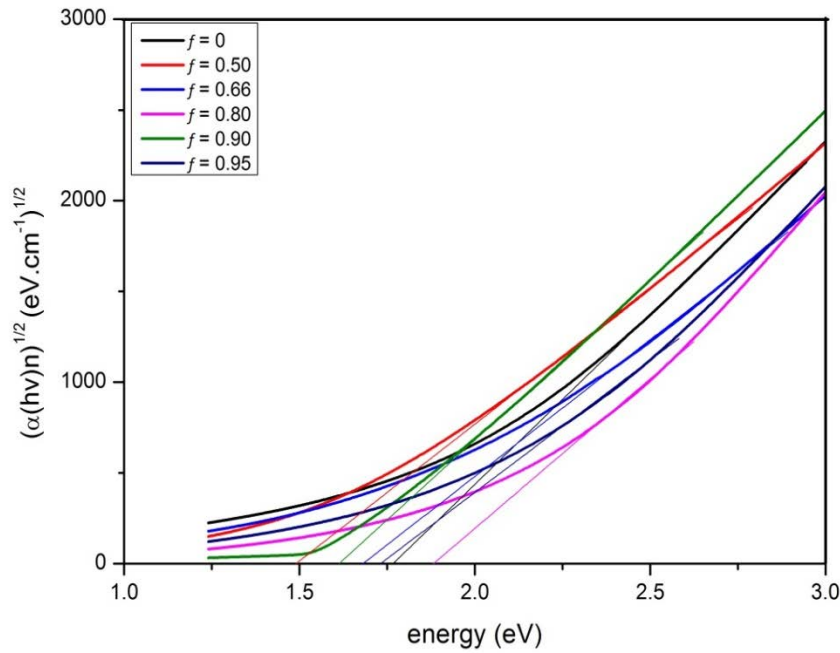


Figure 4.18 Tauc optical band gap curve

The E_g values range between 1.54 and 1.84 eV, which is typical for a-Si:H thin films [4.48]. In contrary to Meiling *et al.* the E_g does not remain constant for $C_H > 10$ at.%, and we suggest this is as a result of the trapping of hydrogen bonds in voids [4.46]. The stresses as a result thereof alter the E_g by introducing trapped states and band tailing [4.47, 4.48].

The refractive index of amorphous silicon is a good measure of the density of a material. The static refractive index (n_0) has been determined via extrapolation, seen in figure 4.19, and given in the table 4.7

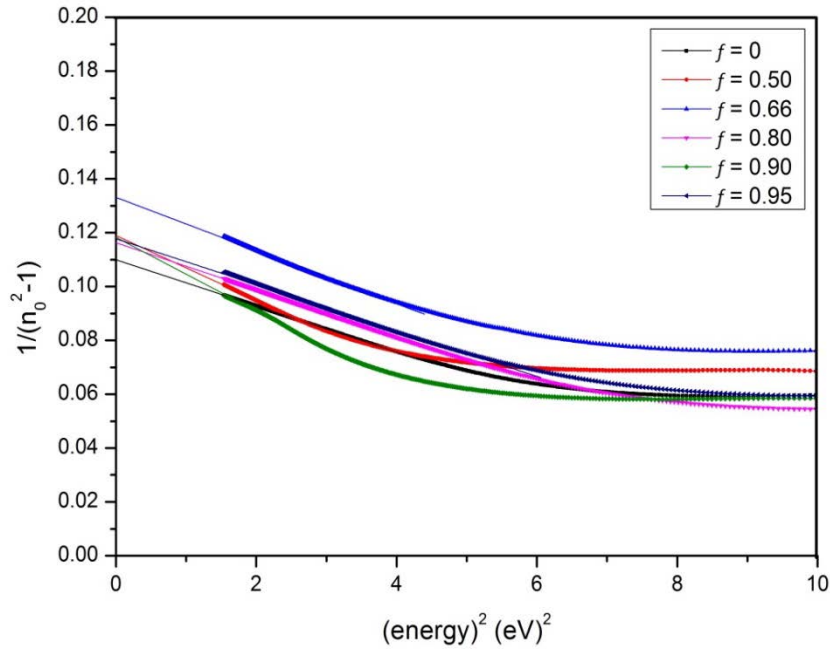


Figure 4.19 Extrapolation of $\frac{1}{n_0^2-1}$ as a function of energy squared

If the material is considered to consist of a tightly bonded structure containing voids, the density of the material follows from the void volume fraction as well. The refractive index of void rich silicon thin films is lower than that of bulk Si, and decreases with increasing porosity, tending to that of air [4.49, 4.50]. Figure 4.20 illustrates the relation between n_0 and void volume fraction with bonded hydrogen content.

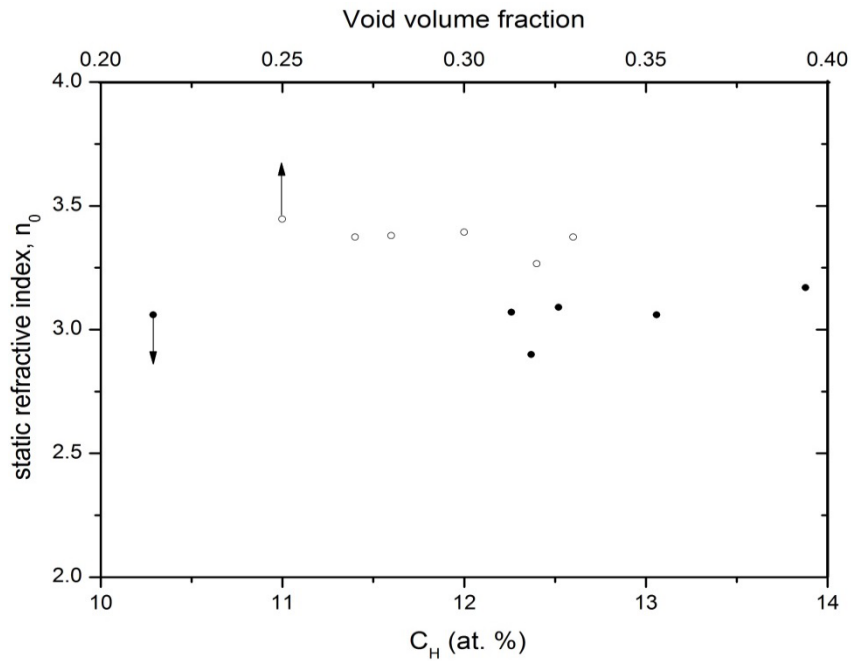


Figure 4.20 Illustration of the dependence of static refractive index (n_0) on bonded hydrogen concentration (C_H) and void volume fraction.

It is apparent that n_0 is constant throughout the series, despite the change in C_H , and in the range of values reported by Cody *et al.* and Severens *et al.* for a-Si:H thin films [4.51, 4.52]. The consistency in n_0 and void volume fraction with the change in C_H , implies a constant density among the deposited films.

4.4 Conclusion

In this contribution six thin films deposited by HWCVD technique, were investigated. Each thin film deposition varied in deposition time and H₂ dilution.

Raman spectroscopy showed that all the thin films have a bond angle variation within the range of maximum order for a-Si:H. The emergence of the (002) hexagonal Si diffraction plane for thin films deposited at $f = 0.5$ and 0.95 is seen in XRD analysis. Structural analysis proved a void rich nature and presence of molecular hydrogen in the thin films. The bonded hydrogen concentration exceeded 10 at.% for each thin film. Surface morphology investigations showed evidence of particle coalescence of grains and the rms roughness was constant for each sample except for the sample deposited at $f = 0.95$. For this deposition condition a relatively featureless surface morphology was observed.

After achieving excellent optical modelled reflection spectra fits, the optical interrogation showed the variation in optical band gap due to void presence. Furthermore void volume fraction and static refractive index shows a constant behaviour with bonded hydrogen concentration.

References:

- [4.1] A.C. Dillon, A.H. Mahan, J. L. Alleman, M. J. Heben, P.A. Parilla and K.M. Jones (2003) *Thin Solid Films*. **430**, 292.
- [4.2] K. F. Feenstra, R. E. I. Schropp, W. F. van der Weg (1999) *J. Appl. Phys.* **85**, 6843.
- [4.3] R.E.I. Schropp, H. Li, R.H. Franken, J.K. Rath, C.H.M. van der Werf, J.W.A. Schüttauf, R.L. Stolk (2008) *Thin Solid Films*. 516, 6818.
- [4.4] H. R Moutinho, C. S. Jiang, B. Nelson, Y. Xu et al. (2003) *Conference Proceedings. Materials Research Society*. San Francisco, California.
- [4.5] T. Berglundh and J. Lindhe (1997) *Clin. Oral Implants Res.* **8**, 117-124.
- [4.6] I. Abrahamsson, T. Berglundh and J. Lindhe (1997) *J. Clin. Periodontol.* **24**, 568.
- [4.7] C. Das, A. Dasgupta, S.H Saha and S. Ray (2002) *J. Appl. Phys.* **91**, 9401.
- [4.8] S. Zeng and N. Ali (2007) *Nanocomposite Thin Films and Coatings*. Imperial College Press, London, p474-482.
- [4.9] H. R Moutinho, C. S. Jiang, B. Nelson, Y. Xu et al. (2005) *Conference Paper. 31st IEEE Photovoltaics Specialists Conference*. Florida.
- [4.10] M. H. Brodsky, M. Cardona, J. J. Cuomo (1977) *Phys. Rev. B.* **16**, 3556.
- [4.11] H. Shanks, C.J. Fang, L. Ley, M. Cardona, F.J. Desmond, S. Kalbitzer (1980) *Phys. Status Solidi B.* 100, 43.
- [4.12] H. Looyenga (1965) *Physica*. 31, 636.
- [4.13] A. M. Brockhoff (2001) *Hydrogen-Related Modifications of Amorphous Silicon and Silicon Nitride*, Ph.D. thesis, Utrecht University.

- [4.14] V. Pecharsky and P. Zavalij(2008) *Fundamentals of Powder Diffraction and Structural Characterization of Materials, Second Edition*. Springer, ISBN: 9780387095783. pages 260-268.
- [4.15] C.J. Oliphant, C.J. Arendse, S.N. Prins, G.F. Malgas, D.Knoesen (2012) *Journal Material Science*. **47**, 2405.
- [4.16] N. Kniffler et al. (2009) *Thin Solid Films*. **517**, 3424.
- [4.17] H. Olijnyk, S.K. Sikka, W.B. Holzapfel (1984) *Phys. Lett. A*. **103**, 137.
- [4.18] Kenji Nakazawa and Keiji Tanaka (1990) *J. Appl. Phys.* **68**, 1029.
- [4.19] R.L.C. Vink, G.T. Barkema, and W.F. van der Weg (2001) *Phys. Rev. B*. **63**, 115210.
- [4.20] D. Beeman, R. Tsu and M. F. Thorpe (1985) *Phys. Rev. B*. **32**, 874.
- [4.21] S. Roorda, W. C. Sinke, J. M. Poate, D. C. Jacobson, S. Dierker, B. S.Dennis, D. J. Eaglesham, F. Spaepen, and P. Fuoss (1991) *Phys. Rev. B*.44, 3702.
- [4.22] T. Saito, T. Karasawa, and I. Ohdomari (1982) *J. Non-Cryst. Solids*. 50, 271.
- [4.23] W. C. Sinke, T. Warabisako, M. Miyao, T. Tokuyama, S. Roorda and F. W. Saris (1988) *J. Non-Cryst. Solids*. **99**,308.
- [4.24] C.L. Fang et al. (1980) *Journal Non-Cryst. Solids*.35.
- [4.25] H. Fujiwara, M. Kondo, and A. Matsuda (2002) *Jpn. J. Appl. Phys.* **41**, 2821.
- [4.26] H. Fujiwara, M. Kondo, and A. Matsuda (2002) *Surf. Sci.* 497, 333.
- [4.27] U. Kroll, J. Meier and A. Shah (1996) *J.Appl.Phys.* **80**, 4971.
- [4.28] H.R. Shanks, F.R. Jeffrey, M.E. Lowry (1981) *Journal de Physique*. **42**, 773.
- [4.29] H. Wagner and W. Beyer (1983) *Solid State Comm.* **48**, 585.
- [4.30] Z.W. Zuo, W.T. Guan, Y. Wang, J. Lu, J. Z. Wang, L. Pu, Y. Shi, Y.D. Zheng, X. Y. Luo and H. H. Wang (2011) *App. Phys. Lett.* **98**, 041902.
- [4.31] H.R Shanks *et al.* (1987) *Journal de physique*. **C4**,42, p773.

- [4.32] B. Strahm, A. Feltrin, G. Bugnon, F. Meillaud-Sculati, C. Ballif, A. A. Howling and C. Hollenstein (2009) *Study of the microstructure transition width from amorphous to microcrystalline silicon as a function of the input silane concentration*. SPIE conference on thin film solar technology. San Diego.
- [4.33] Y. Ziegler, V. Daudrix, C. Droz, R. Platz, N. Shah (2001) *Sol. Energy Mat. Solar Cells*. **66**, 413.
- [4.34] E. Srinivasan and G.N. Parsons (1997) *J. Appl. Phys.* **81**, 2847.
- [4.35] J.K. Rath, L.A. Klerk, A. Gordijn, and R.E.I. Schropp (2006) *Sol. Energy Mater. Sol. Cells*. 90, 3385.
- [4.36] F.C Marques, P. Wickbodt, D. Pang, J.H. Chen and W. Paul (1998) *J. Appl. Phys.* **84**, 3118.
- [4.37] H. Shirai, D. Drevillion, I. Shimizu (1994) *Jpn. J. Appl. Phys.* **33**, 5590.
- [4.38] Chang-Ho Cho and Young-Seok SEO (1998) *Journ. Korean Phys. Soc.* **33**, 3, 292.
- [4.39] R. W. Collins et al. (2003) *Solar Energy Materials and Solar Cells*. 78, 143.
- [4.40] Brockhoff, van der Weg and Habraken (2001) *J. Appl. Phys.* 89, 5.
- [4.41] W. M. M. Kessels et al. (2006) *Thin Solid Films*. 501, 81.
- [4.42] M.F. Gyure, J.J. Zinck, C. Ratsch, D.D. Vvendensky (1998) *Phys. Rev. Lett.* **81**, 4931.
- [4.43] R. Swanepoel (1983) *J. Phys. E: Sci. Instrum.* **14**, 1214.
- [4.44] A. Shah (2010) *Thin film silicon solar cells*. CRC Press. Italy. p35-43.
- [4.45] J. Tauc, R. Grigorovici, and A. Vancu (1966) *Phys. Stst. Sol.* **15**, 627.
- [4.46] H. Meiling (1991) PhD Thesis, University Netherlands, Utrecht.
- [4.47] K. Winer, I. Hiyabayashi, and L. Ley (1988) *Phys. Rev. B*. 38, 7860.
- [4.48] K. Winer, I. Hiyabayashi, and L. Ley (1988) *Phys. Rev. Lett.* 60, 2697.

- [4.49] W. Theiss and S Hilbrich (1997) *Properties in porous silicon, edited by Leigh Canham*. INSPEC, The Institute of Electrical Engineers.
- [4.50] S.K O’Leary, S.R. Johnson, and P.K Lim (1997) *J. Appl. Phys.* **82**,3334.
- [4.51] G D Cody, C R Wronski, B Abeles, R B Stephens and B Brooks (1980) *Solar Cells* **2**, 227.
- [4.52] R J Severens, G J H Brussaard, H J M Verhoeven, M C M Van De Sanden and D C Schram (1995) *Mater. Res. Soc. Symp. Proc.* **377**, 33.



CHAPTER FIVE

SILICON THIN FILMS BY DYNAMIC VARIATION OF HYDROGEN DILUTION

5.1 Introduction

Tandem-structured solar cells have made great advances at increasing solar cell efficiency [5.1, 5.2]. Along with its increased absorption capabilities, tandem solar cells show a reduction in recombination losses [5.3]. Although these solar cells are a major improvement from the single junction solar cells, its downfall lies in production cost. Furthermore, costs are increased by the energy required for heating during deposition. Commonly, hydrogenated amorphous (a-Si:H) and nanocrystalline silicon (nc-Si:H) single junction solar cells are stacked one above the other to achieve this tandem-structure. A crucial part in the structure of tandem solar cells is the junction that divides the individual cells, since this is where recombination occurs via a tunnelling process, which occurs due to crystallite formation [5.4]. Moreover, crystallite formation results in cracks within the bulk of the thin film, which serve as alternative recombination routes for charge carriers. This adds an additional factor to account for when establishing a current match between the two thin films layers in contact, from the different solar cells [5.5].

In this study, we propose to deposit a single, intrinsic-layer thin film to eliminate the issues attained from the tunnelling process in tandem solar cells, using an alternative deposition procedure for silicon thin films by hot-wire chemical vapour deposition (HWCVD) with no substrate heating.

With the insight gained on the structural and optical properties of the thin films investigated in Chapter 4, we proceed with this intriguing endeavour. The deposition conditions used in the former chapter will serve as the deposition regimes for the thin films deposited in this contribution. The structural and optical properties of two deposition protocols are investigated, i.e. by either increasing or decreasing hydrogen dilution during the deposition.

5.2 Experimental Details

The thin films were simultaneously deposited on single-side polished (100) crystalline silicon and Corning 7059 glass substrates using an ultra-high vacuum HWCVD system [5.6] from gas mixtures of SiH₄ and H₂. The Ta filament temperature and the deposition pressure were fixed during deposition at 1600 °C and 60 μbar, respectively. It should be noted that no substrate

heating was applied during deposition. The H-dilution ratio, defined as $f = \frac{\Phi_{H_2}}{(\Phi_{H_2} + \Phi_{SiH_4})}$,

where Φ denotes the gas flow rate, was varied from 0 – 95 % during deposition, either in an increasing (Protocol 1) or a decreasing direction (Protocol 2). Changes in the H₂ dilution were carefully controlled in specific time frames, referred to as regimes. After the completion of a particular regime, the shutter was inserted to stop the deposition, after which the gas flow rates were changed to the desired values. Once the gas flow rates and the deposition pressure were stable, the shutter was removed to allow for the deposition to continue at the new regime. The total deposition time for both samples amounted to 33 min. The deposition conditions for each protocol is summarised in table 5.1.

Table 5.1 Deposition condition for stacked film deposition runs

Deposition Regime		Deposition time (minutes)	Φ_{H_2} (sccm)	Φ_{SiH_4} (sccm)
Protocol 1	Regime 1	2	0	3
	Regime 2	3	3	
	Regime 3	5	6	
	Regime 4	8	12	
	Regime 5	10	27	
	Regime 6	5	28.5	
Protocol 2	Regime 1	5	28.5	3
	Regime 2	10	27	
	Regime 3	8	12	
	Regime 4	5	6	
	Regime 5	3	3	
	Regime 6	2	0	

Fourier transform infrared (FTIR) absorption spectra were collected in transmission geometry from 400 – 4000 cm^{-1} with a spectral resolution of 1 cm^{-1} , using a Perkin-Elmer Spectrum 100 FTIR spectrophotometer. The total bonded hydrogen concentration was estimated from the integrated absorption of the 640 cm^{-1} rocking mode using previous reported procedures [5.7, 5.8]. Elastic recoil detection (ERD) analysis was conducted using a 3 MeV mono-energetic and collimated beam of $^4\text{He}^+$ ions, where the recoiled H atoms were detected at an angle of 30° with respect to the incident ion beam. The H depth-profile was simulated using the SIMNRA simulation software.

X-ray diffraction (XRD) was performed using a PANalytical Xpert diffractometer at 2θ -values ranging from $5 - 90^\circ$, with a step size of 0.02° . Copper $K\alpha_1$ radiation with a wavelength of 1.5406 \AA was used as the x-ray source. The Raman measurements were performed in a range of 100 to 700 cm^{-1} . The measurements were performed using 514.5 nm argon (Ar) ion laser detector in the backscattering configuration [5.110]

The surface morphology was investigated using a ZEIS Auriga high resolution scanning electron microscope (SEM) at an accelerating voltage of 1 kV . Cross-sections of the films were prepared by a FEI Helios NanoLab 650 Dual Beam focussed-ion beam SEM (FIBSEM). Subsequently, high-resolution transmission electron microscopy (HRTEM) and scanning transmission electron microscopy (STEM) was performed and the cross-sections were analysed using a FEI Tecnai F20 FEGTEM at an accelerating voltage of 200 kV .

Optical reflection spectra were measured using a Semiconsoft mProbe UV-Visible photometer in the range $200 - 1000 \text{ nm}$ with a spectral resolution of 1 nm . The refractive index, absorption coefficients and optical thickness were calculated by employing the Looyenga effective medium approximation (LEMA) model [5.9].

5.3 Results and Discussion

5.3.1 Structural Properties

The first insight to the structural properties of the thin films was obtained by cross-sectional transmission electron microscopy. This interrogation provided detailed information on the structural nature of the thin films along the growth direction. Figure 5.1 shows the low magnification TEM micrographs of the complete cross-sections of deposition protocol 1 and 2. The film thickness as determined from TEM imaging amounted to ~ 670 nm for protocol 1 and ~ 750 nm for protocol 2. Two distinct regions can be identified in each protocol; i.e. a carbon surface region, deposited to protect the thin films during the FIBSEM preparation, and the bulk thin film region.

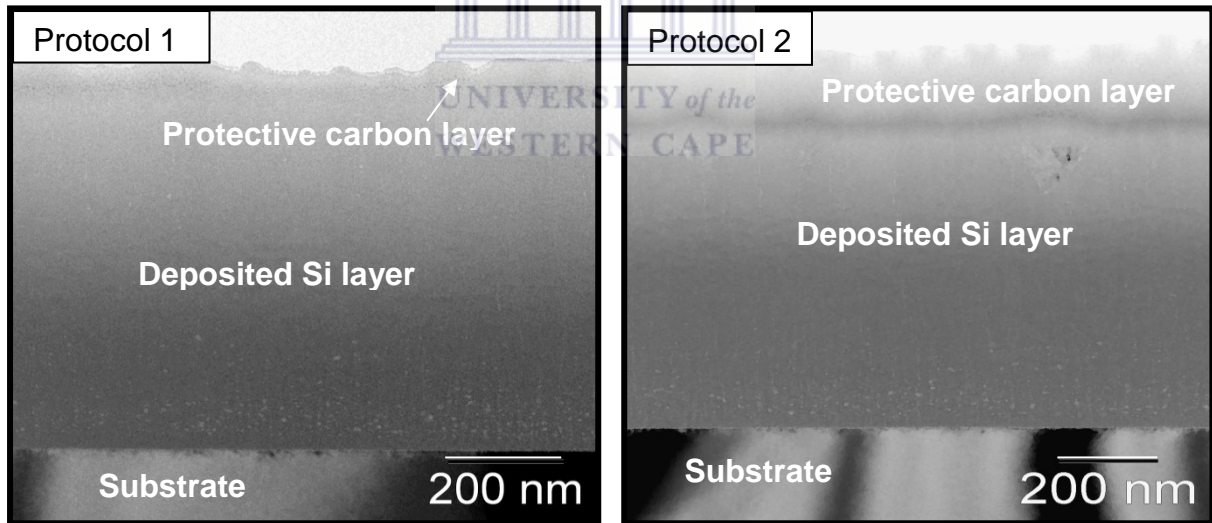


Figure 5.1: Cross-sectional TEM micrographs of samples deposited by protocol 1 and 2.

The various deposition regimes cannot be differentiated along the cross sectional TEM images, although structural variation is observed along the entire cross section of the thin films. As each new deposition regime is initiated, the previous deposited material continues to transform

throughout the deposition, due to continuous processes (such as diffusion, etching and annealing) that occur during the entire deposition.

In figure 5.2, which shows a higher magnification TEM image of protocol 1 at the interface, a well-defined substrate-film (SF) interface region is observed, followed by a 15 nm thick dense amorphous incubation layer. The amorphous incubation layer is generally formed in the initial growth stage of polycrystalline silicon thin film deposited at low temperature [5.11], which implies the onset of crystallinity for protocol 1. Heya *et al* suggested that the variation of hydrogen dilution during deposition could reduce the formation of this amorphous incubation layer [5.12]. A porous bulk layer with spherical structures, of diameter ranging from 2 – 10 nm, is evident after the incubation layer.

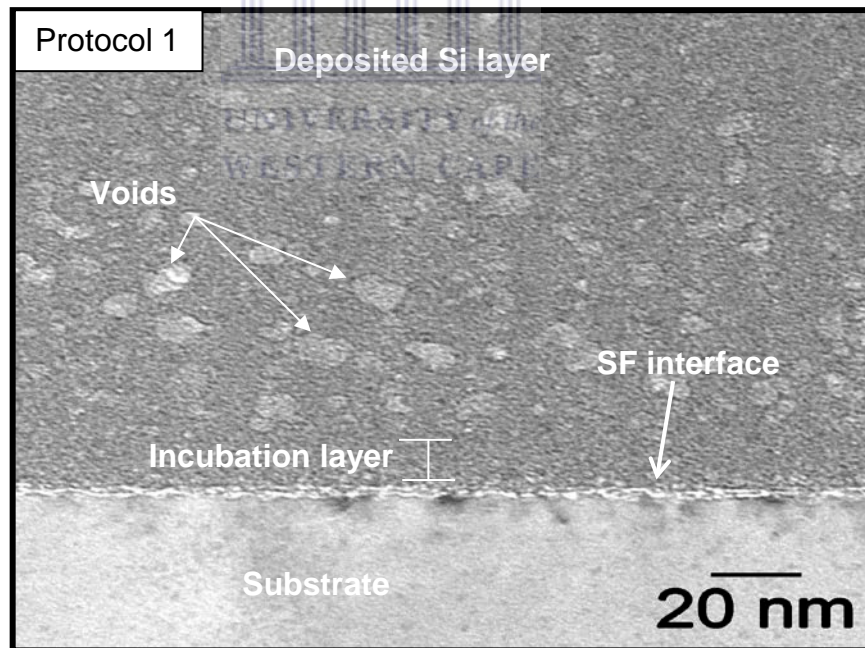


Figure 5.2 Magnified image of voids present in protocol 1

Scanning transmission electron microscopy (STEM) was performed across some of the spherical structures seen across the sample cross section. Figure 5.3 shows the STEM image and line scan signal obtained when the electron beam passed over the observed structures in the cross-section. STEM analysis show a reduction in the STEM signal as it passes over these structures, which infers fewer electrons are being diffracted. These features are therefore suggested to be nano-voids.

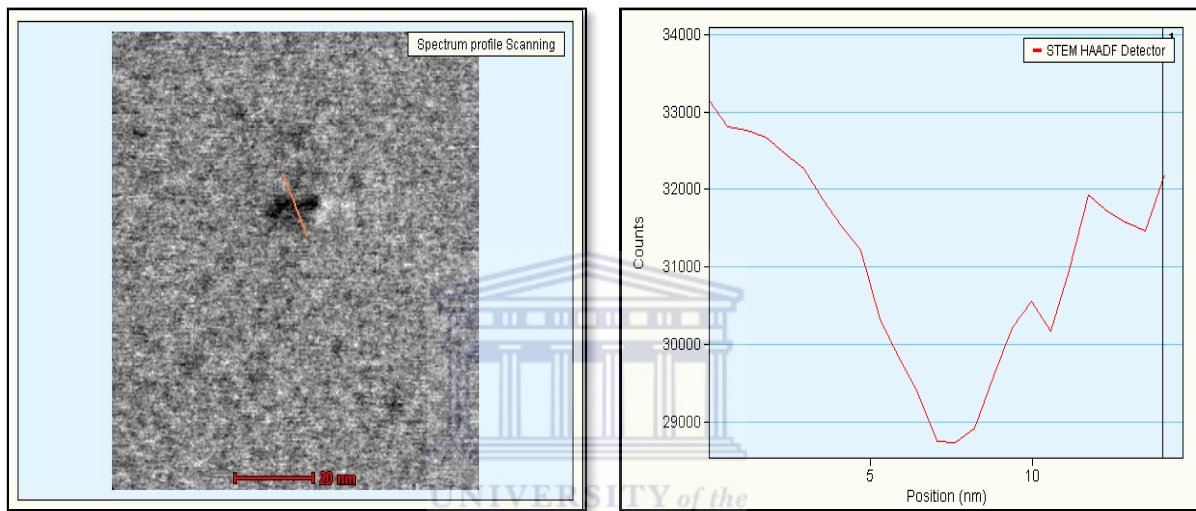


Figure 5.3 STEM signal analysis performed on nano-voids

The density of the voids decreases in the growth direction for both samples, as illustrated in figure 5.4 below. The diameter of the voids becomes smaller, more elongated and less frequent towards the surface for both samples.

Figure 5.5 depicts the SF interfacial region of protocol 2, which appears rough and undefined, with nano-void formation immediately from the SF interface. Closer inspection reveals small embedded regions of order at the SF interface, as evident by the lattice fringes observed. This is attributed to the initial 95% H₂ dilution, which promotes the growth of Si nano-crystallites [5.13, 5.14]. An incubation layer is absent for protocol 2.

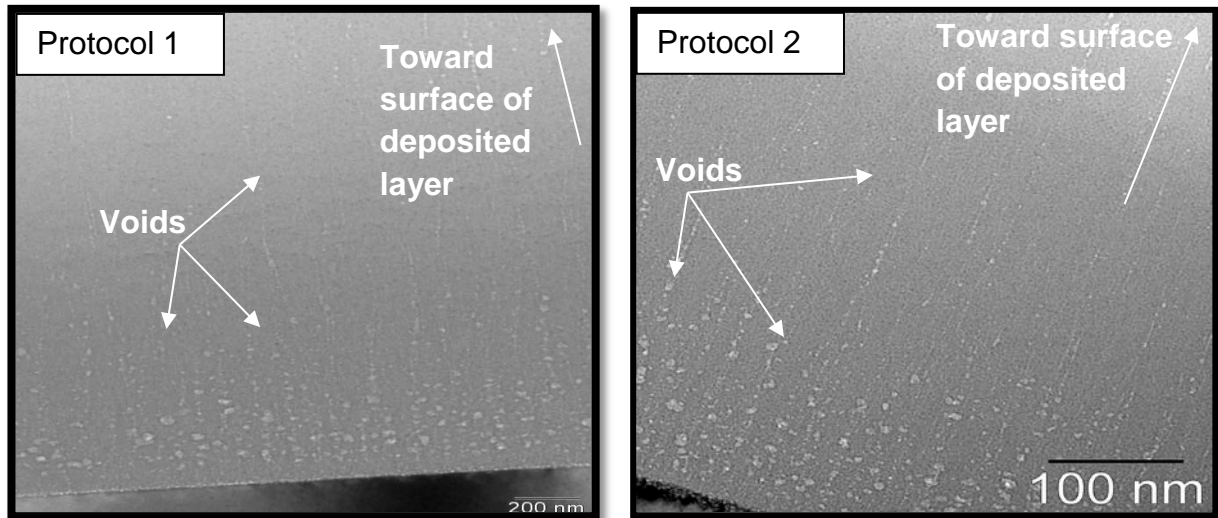


Figure 5.4 Entire cross-sectional views of nano-void formations in both samples.

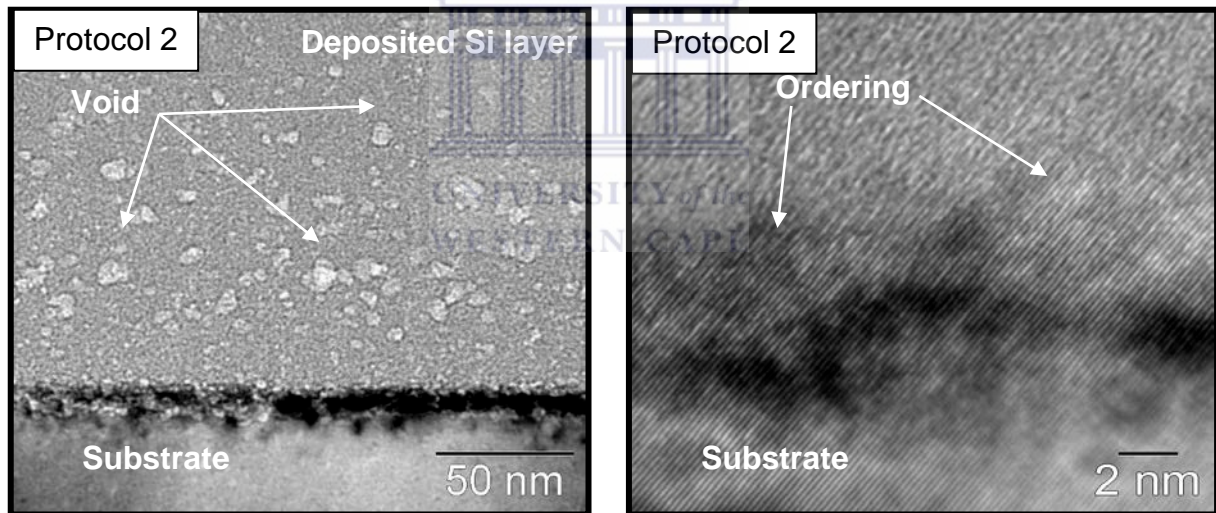


Figure 5.5 Substrate-film interfacial region for protocol 2.

We suggest that since the deposition for protocol 2 started in the extreme H₂ dilution conditions (95 % dilution), an amorphous incubation layer could not form due to unfavorable a-Si growth conditions caused by the overwhelming etching activity of the atomic hydrogen.

Further observation into the crystalline nature of these two protocols was probed by X-ray diffraction (XRD). The absence of any crystalline silicon diffraction peaks in the XRD spectra, shown in figure 5.6; indicate that an amorphous thin film structure is obtained for both deposition protocols.

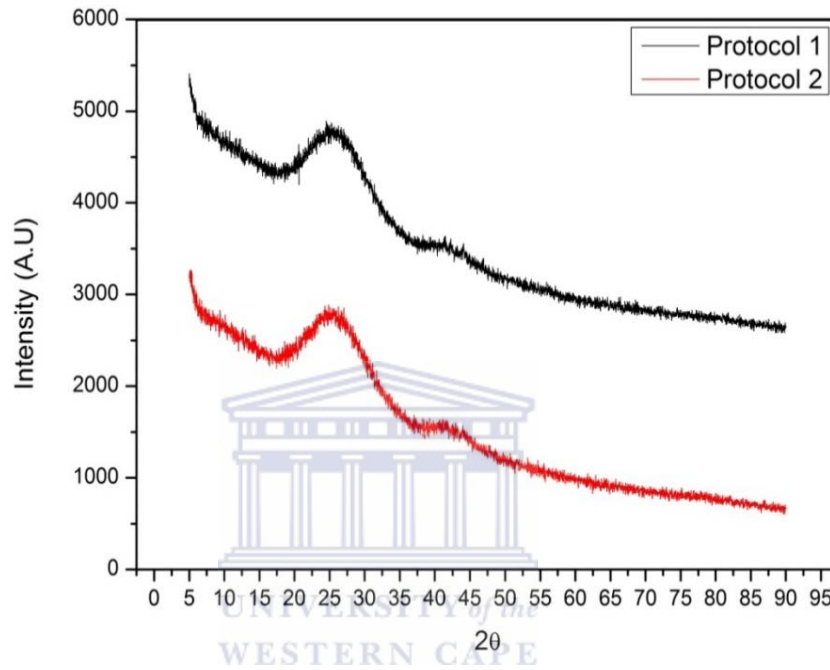


Figure 5.6 X-ray diffraction spectrum for Protocol 1 and 2.

Raman spectroscopy was employed to detect structural changes within the thin film network, more specifically the bond angle variation within both sample protocols. Raman spectra depicted in figure 5.7 has been deconvoluted into three Gaussians, following similar procedures previously mentioned in Chapter 4. No c-Si TO peak is evident at 520 cm^{-1} , which is indicative of no crystallinity present in both thin films.

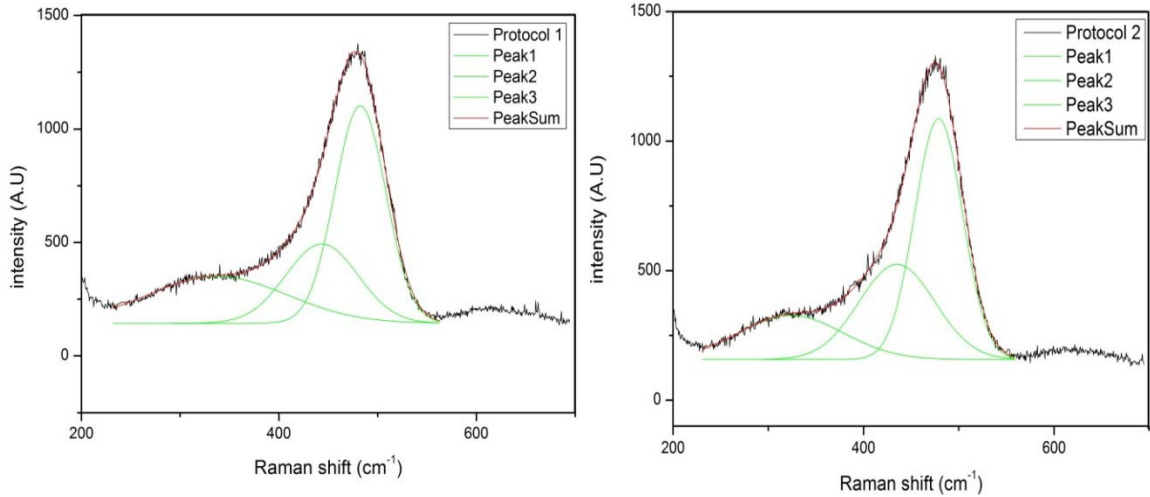


Figure 5.7 Deconvoluted Raman spectra for both samples

Surface diffusion is less active at lower temperatures, which results in the hindrance of the formation of nc-Si nuclei, proposed by the surface diffusion model of nc-Si:H [5.15]. TEM analysis confirms the existence of crystallites at the SF interface of sample protocol 2, though not detectable by XRD and Raman spectroscopy. The bond angle variation (θ_b) determined for Raman analysis is 7.20° and 6.95° for sample protocol 1 and 2, respectively, which is indicative of an ordered film structure [5.16, 5.17].

Surface analysis was carried out using scanning electron microscopy (SEM). Figure 5.8 shows the SEM micrographs of the surface of both protocols. The analysis discloses a high density of clusters on the surface of both samples, with an average diameter of 150 nm and 80 nm for protocol 1 and 2, respectively. Protocol 2 therefore appears relatively smoother and more compact than sample protocol 1.

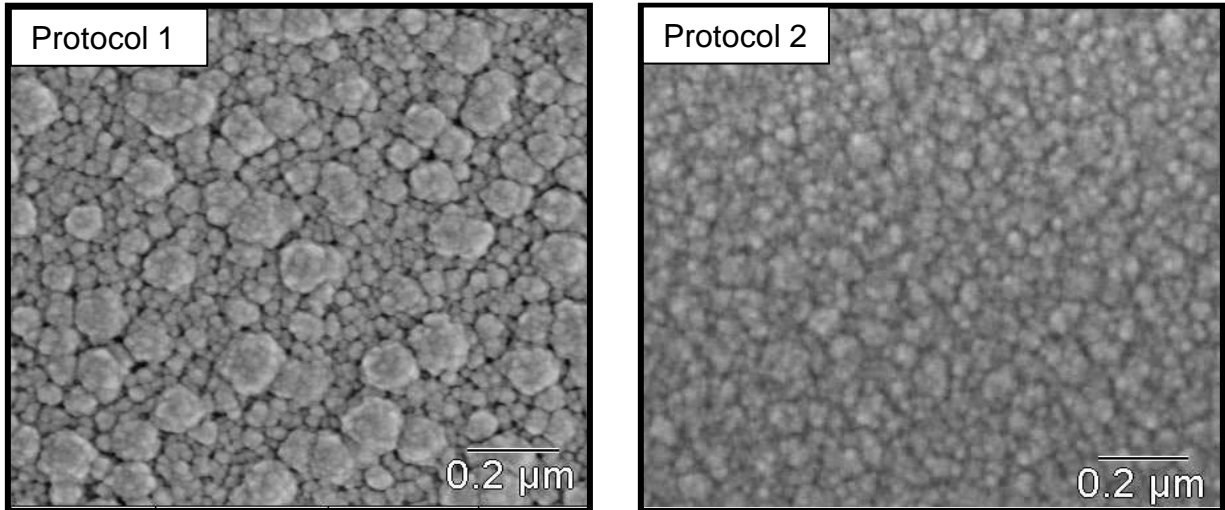


Figure 5.8: SEM micrographs of surface roughness

The selective etching model of nc-Si:H dictates that an increase in H₂ dilution during deposition, which results in an increase in the concentration of reactive atomic hydrogen, would enhance the etching of weak and strained near-surface Si-Si bonds [5.13, 5.18]. The nucleation of nano-sized Si-crystallites would therefore be promoted towards the surface of protocol 1, where increasing amounts of H₂ dilution was used, which will be accompanied by a porous surface [5.14]. Conversely, the decreasing H₂ dilution for protocol 2 would imply a compact, smoother surface due to the decrease in the reactive atomic hydrogen towards the end of the deposition run. This prohibited the formation of nucleation sites at the surface. Thus the nucleation of nano-sized Si-crystallites is evident at the SF interface of protocol 2, a regime in which excessive amounts of atomic hydrogen would have been present, as seen in figure 5.5.

5.3.2 Hydrogen Bonding and Microstructure

FTIR spectroscopy is the established analytical technique of choice to probe the silicon-hydrogen bonding configurations in silicon related material. In figure 5.9 the FTIR absorption spectra is displayed for both sample protocols. The absorption spectra reveal the existence of three characteristic vibrational modes; rocking, bending and stretching vibrational modes. These modes are attributed to the same bonding configuration as mentioned for the absorption spectra attained in chapter 4.

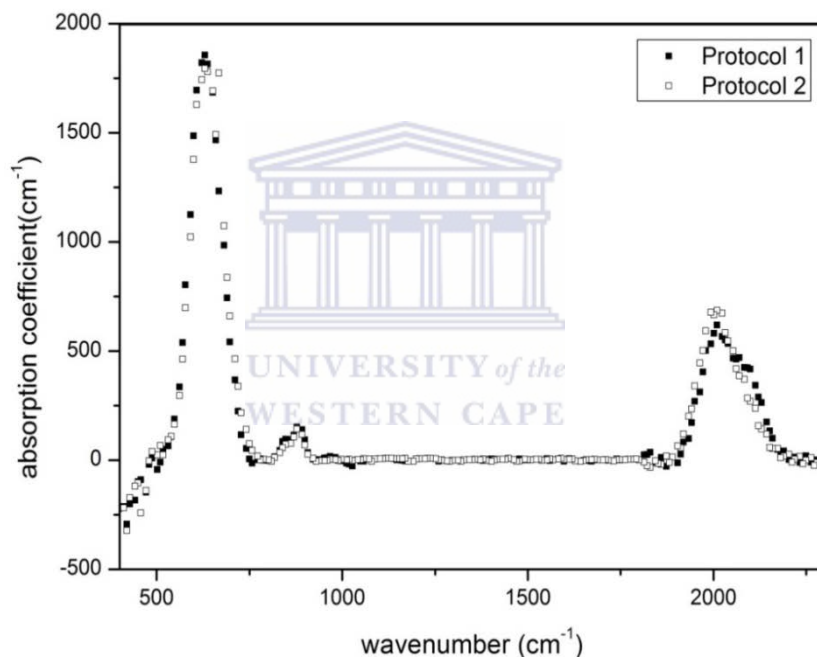


Figure 5.9 FTIR absorption spectra for the samples

Thin film oxidation is not present in both samples, as confirmed by the absence of Si-O stretching bonds at $\sim 1100 \text{ cm}^{-1}$ [5.19.]. As seen from TEM analysis; the nano-voids are densely populated closer to the substrate than compared to the surface, reducing oxidation capabilities at the sample surface. The bonded hydrogen concentration (C_H) was determined from the rocking

mode, at 640 cm^{-1} of the FTIR absorption spectrum, which amounts to $\sim 9.0\text{ at.}\%$ for both samples.

Elastic recoil detection's (ERD) sensitivity to light elements makes this technique ideal for studying hydrogen content in a thin film. The raw and fitted ERD spectra for protocol 1 and 2 are shown in figure 5.10.

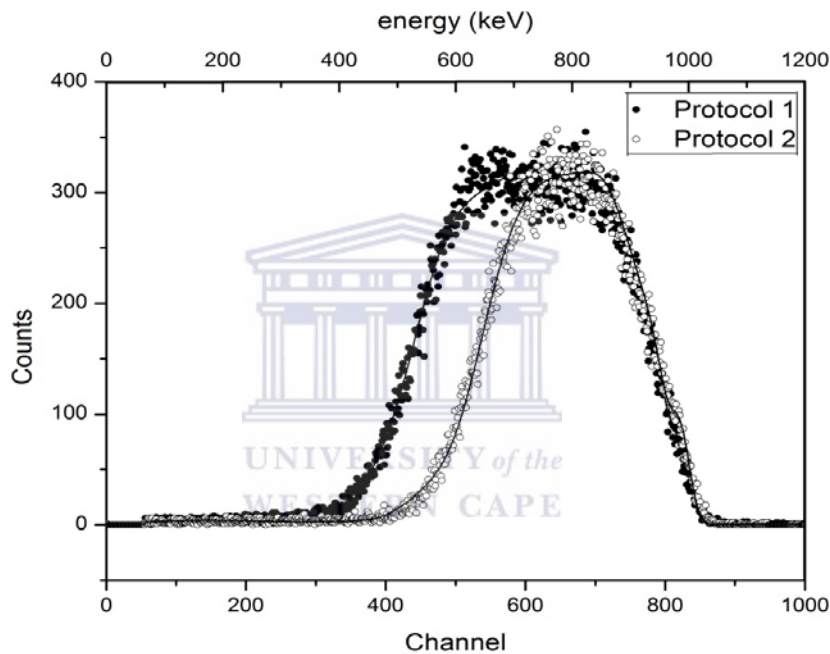


Figure 5.10: Raw and fitted ERD spectra for protocol 1 and 2.

It is evident that the hydrogen distribution was fairly homogeneous within the bulk of both thin films. The total hydrogen concentration (C_{TH}) for protocol 1 and 2, as calculated from ERD, amounts to $15.6\text{ at.}\%$ and $18.1\text{ at.}\%$, respectively, suggestive of a large concentration of molecular hydrogen present in both thin films. Molecular hydrogen (H_2) that is trapped in the nano-voids present within the thin film dictates the increase in void volume fraction and its evolution within the sample [5.20, 5.21]. Evidence of the presence of polyhydrides within the

thin film is further brought forth by the FTIR bending modes, associated with $(\text{Si}=\text{H}_2)_n$ chains, which emerge for both protocols seen in figure 5.9.

The microstructure factor (R^*), which represents the ratio of hydrogen bonded in the clustered phase is determined from the stretching mode absorption peaks. The FTIR stretching vibrational spectra are shown in figure 5.11.

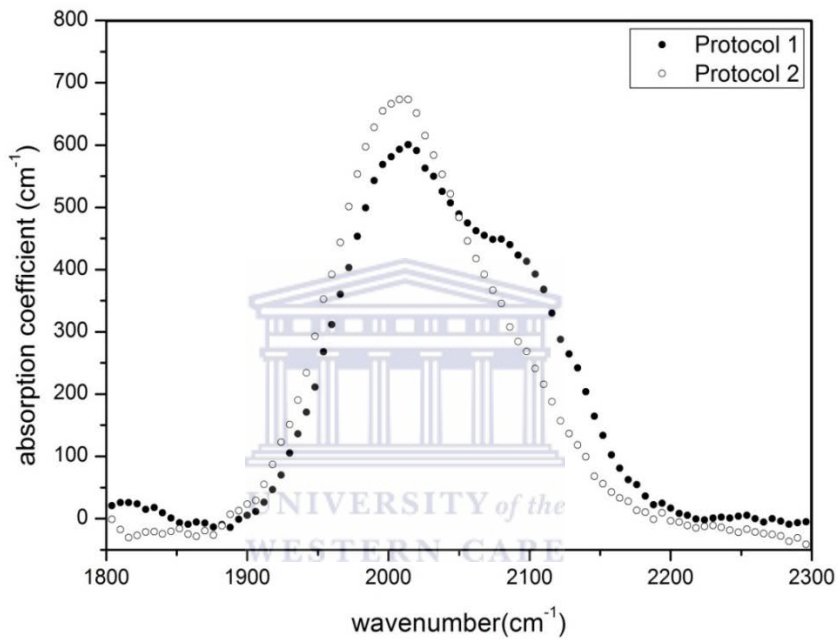


Figure 5.11 FTIR absorption spectra of the stretching vibrational mode

Two absorption peaks emerge, characteristic of α -Si:H and centred around 2000 cm^{-1} , assigned to isolated Si-H monohydrides, and 2100 cm^{-1} , associated with Si-H_x polyhydrides and Si-H bonded on the inner surface of voids [5.22]. The two associating peaks were deconvoluted for microstructural analysis of these thin films. Figure 5.12 illustrates the deconvoluted spectra of the stretching vibrational mode for both samples where it's seen that protocol 1 has a more pronounced 2100 cm^{-1} peak than that of protocol 2.

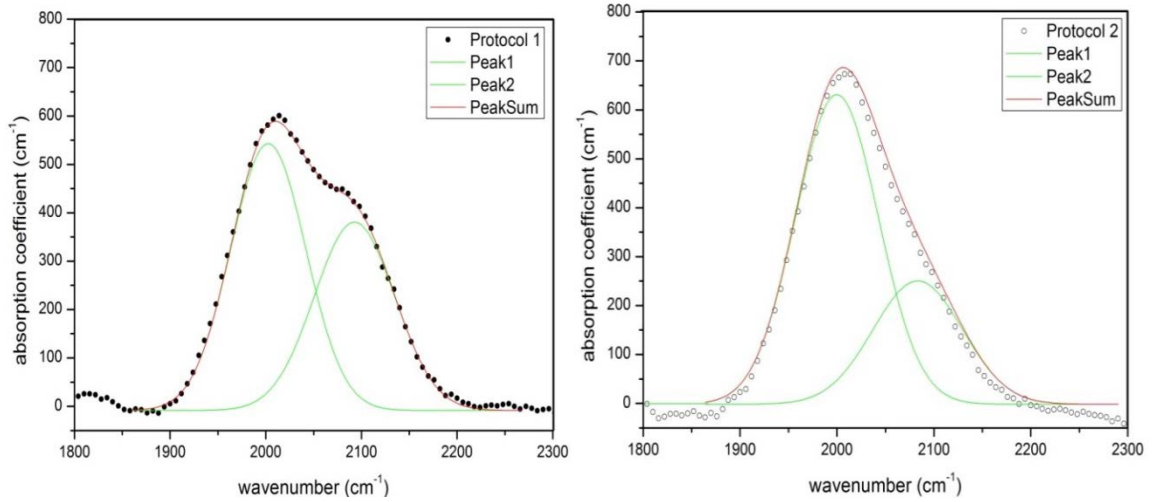


Figure 5.12 Deconvoluted spectra of the stretching vibrational mode of protocol 1 and 2 respectively.

The R^* values obtained amounts to ~ 0.4 and 0.3 for protocol 1 and 2, respectively. This result is indicative of a greater structural inhomogeneity for protocol 1. This is attributed to the low substrate temperature and the absence of hydrogen dilution during the initial growth stage of protocol 1, which promotes the formation of structural inhomogeneity, such as polyhydrides.

Differentiation between the two samples is observed from TEM analysis with the existence of crystallites in protocol 2 only. Other distinguishing features are the surface morphology and structural inhomogeneous increasing for sample protocol 1 compared to protocol 2. Although the concentration of molecular hydrogen is greater within protocol 2, the C_H is relatively constant for both sample protocols. The effect of these structural characteristics on the optical properties of these uniquely deposited Si thin films are imperative and will be examined in the next section.

5.3.2 Optical Properties

A complex film with an anisotropic character demands an intricate and rigorous analysis methodology to account for microscopically heterogeneous features. Excess hydrogen bonded on voids, as inferred from FTIR, and inferences from TEM analysis confirming the presence of ordered zones, disordered zones, boundaries between ordered and disordered zones, and porous zones, all add to the complexity of the optical equivalent of the material that must be constructed. The optical model must also account for a sharp, porous interface with the substrate, and the existence of very small crystallites in the interface region, or anywhere in the film.

A viable methodology is to consider the film on the macroscopic level as a random mixture of phases. The dielectric functions of various materials as a matrix and particles, which allows for the calculation of a theoretical spectrum are combined in the Effective Medium Approximations (EMA) [5.23]. This is well-suited for laborious calculations of the spectra of complex materials. For high porosities it is advisable to use the Looyenga formula [5.24, 5.9]. The OJL construct of a theoretical semiconductor is once again used to model these thin films [5.25], with embedded polycrystallites as the matrix, and embedded particles of air to account for porosity.

Our theoretical film in the optical model accounts for six individual pseudo layers in the depth of the film, which may exhibit anisotropic optical behaviour due to the six different deposition regimes used during film growth. A schematic representation of the theoretical model is illustrated in figure 5.13.

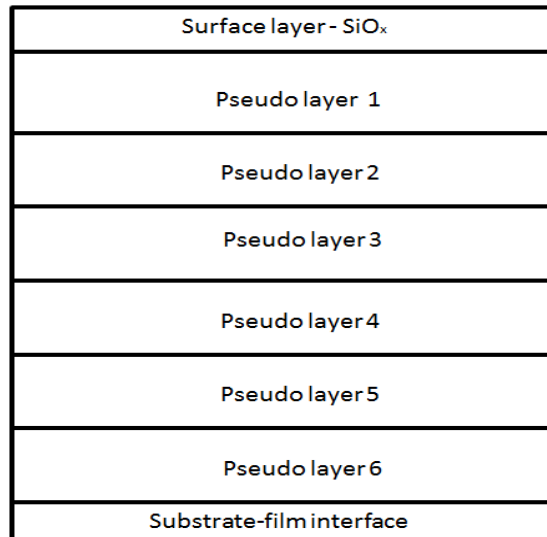


Figure 5.13: Schematic representation of theoretical semiconductor constructed

In addition we have evidence of the existence of a substrate-film interface, and surface-air interface regions, which is also accounted for in the Scout® simulation software [5.26].

Figure 5.14 shows the simulated fits on the reflectance data obtained by applying the Looyenga EMA. The simulated fits achieved below are categorized as excellent fits, with associated fit deviations of 1.53×10^{-5} and 1.07×10^{-5} for protocol 1 and 2, respectively. Furthermore, the independent optical modelling resulted in a total thickness of 686.3 nm and 755.9 nm for protocol 1 and protocol 2, respectively, which compares impeccably with the values concluded from TEM analysis.

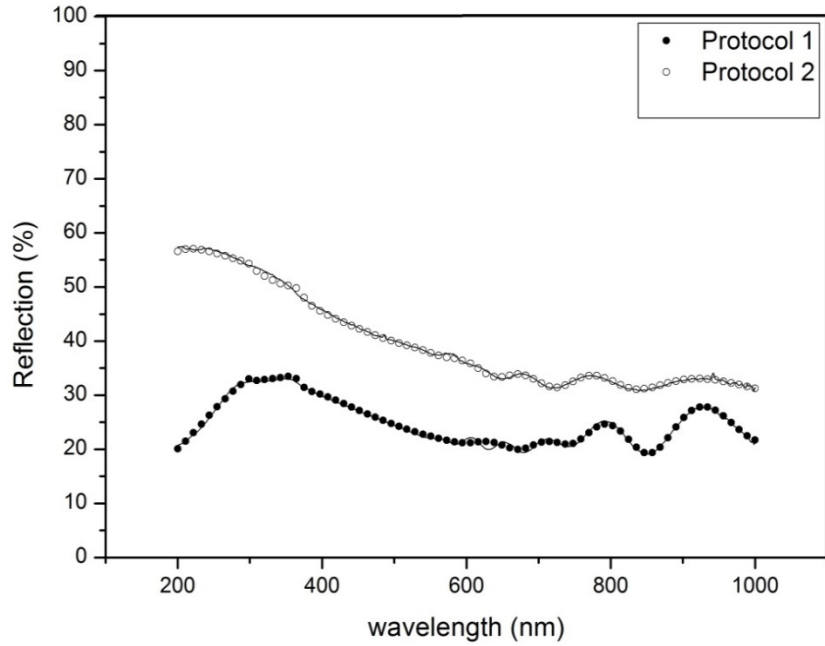


Figure 5.14 Simulated reflectance measurement fit using Looyenga EMA

The refractive index (n) curves are displayed in figure 5.15 below, for both deposition protocols. In this figure, we consider only the six optically insinuated pseudo layers assigned to the six deposition regimes. The variation in n with energy can be seen to change, without trend, with each deposition regime.

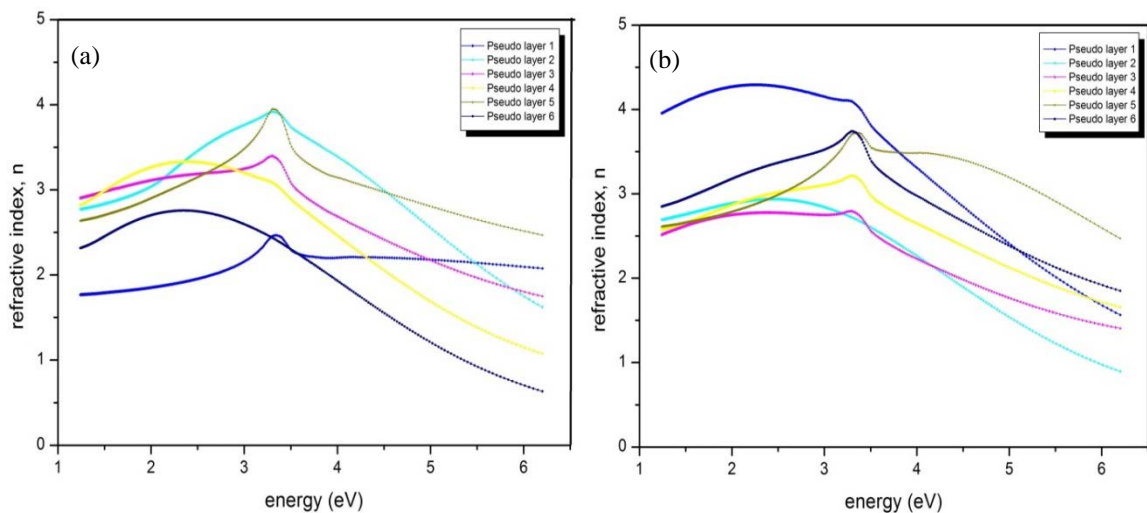


Figure 5.15 Refractive index variations with deposition regime, for (a) Protocol 1 and (b) Protocol 2

Figure 5.16 depicts the refractive index at 2 eV ($n_{2\text{eV}}$) as a function of a thickness ratio (t_r). This thickness ratio indicates the ratio of the increase in film thickness, with each deposition regime change, and total film thickness;

$$t_r = \frac{t_{i-1} + t_i}{t_{total}} \quad (5.1)$$

where t_i and t_{total} refers to the thickness of each optically modelled pseudo layer thickness and the total thickness respectively.

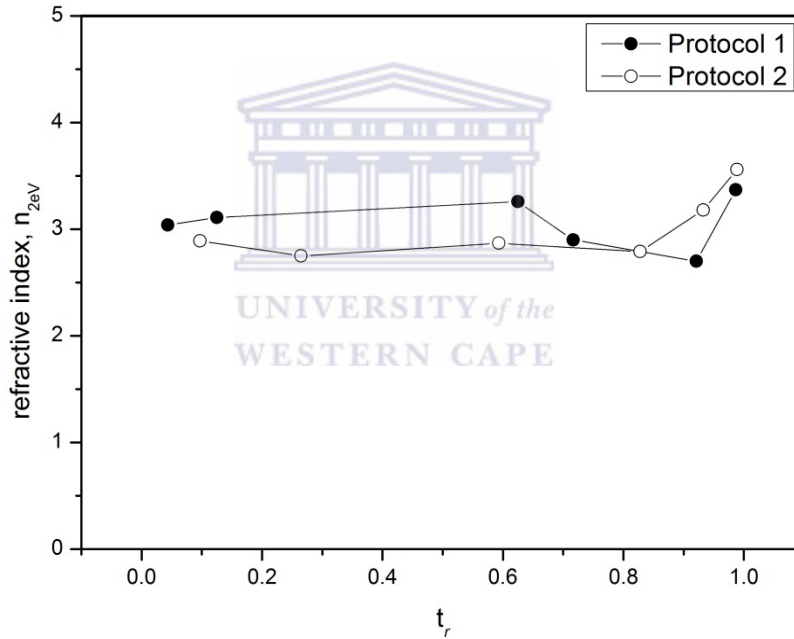


Figure 5.16 Variation in refractive index, at 2eV, with thin film depth

The $n_{2\text{eV}}$ is constant along the film depth for both protocol 1 and 2. Since the refractive index is related to thin film density, a constant refractive index is thus indicative of a constant density along the thin film depth. When comparing the behaviour of $n_{2\text{eV}}$ with depth of the two thin films, protocol 1 and 2, the $n_{2\text{eV}}$ shows a similar behavior. The $n_{2\text{eV}}$ remain constant from the surface going into the bulk, where protocol 1 is optically denser than sample protocol 2. As the

substrate is approached protocol 2 becomes optically denser at the near substrate region, than in the bulk of the film.

The dependence of n on energy, for the complete thin film, is displayed in figure 5.17. Generally the static refractive index (n_0), which is the refractive index value determined at 0 eV, for a-Si:H is found to be ~ 3.4 . For the n_0 of protocol 1 and 2, a value of 2.44 and 2.82 respectively, was determined in this study. This low refractive index is attributed to the void presence, observed from the structural analysis completed above.

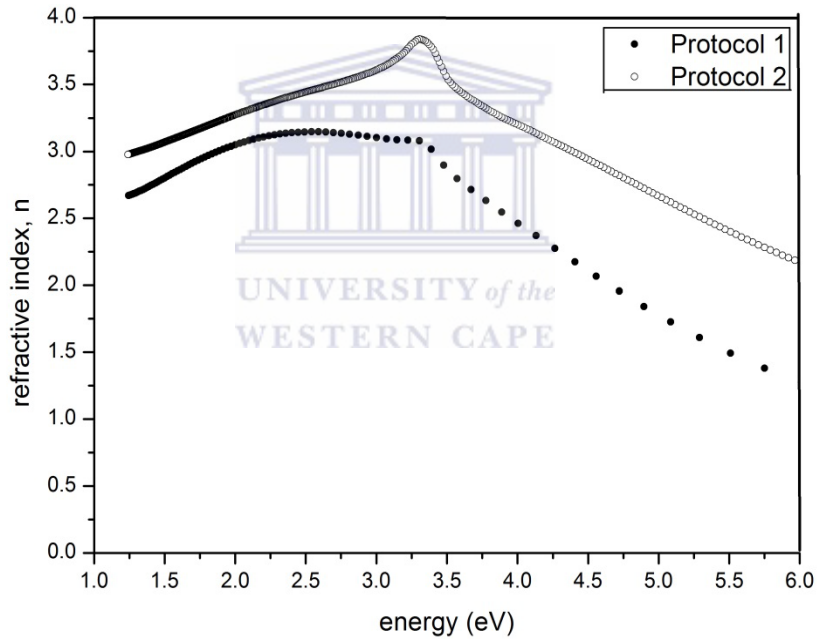


Figure 5.17 Refractive index for both deposition protocol 1 and 2

The refractive index influences the absorption behaviour of the thin film, and thus its band gap. Figure 5.18 illustrates the complete optical absorption behaviour of both thin films across the visible and ultra-violet (UV) energy range. There is a difference in optical behaviour, observed as the deposition regime is changed in a forward or reverse manner with respect to hydrogen dilution.

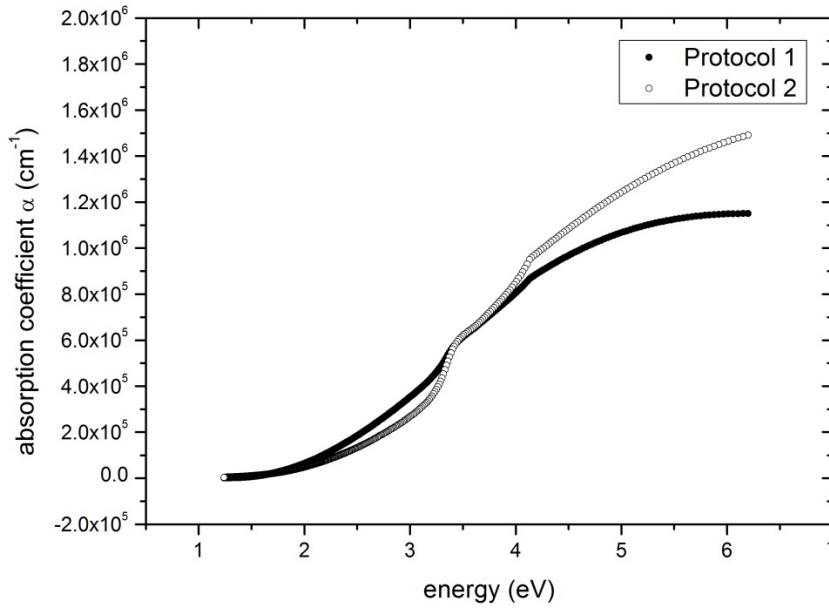


Figure 5.18 Absorption coefficient spectra of both samples

It is noticeable that deposition procedure, protocol 1 is more absorbing in the visible range than protocol 2, whereas protocol 2 is more absorbing in the UV-range than protocol 1. The variation in absorption behaviour is directly affected by the variation in optical density along the growth.

H_2 dilution has been reported to result in the increase of E_g due to the effects of quantum confinement [5.27, 5.28], with reported E_g values for nc-Si:H of 2 - 2.2 eV [5.29]. The overall optical band gap (E_g) was determined, following the same Tauc extrapolation procedure previously seen, for both deposition protocols depicted in figure 5.19 below.

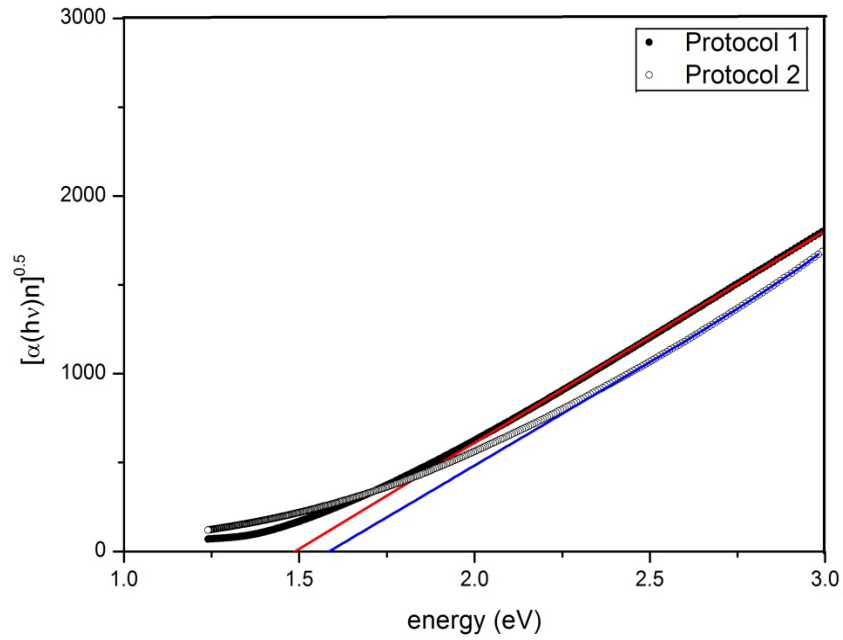


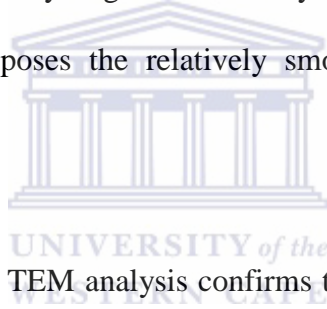
Figure 5.19: Tauc optical band gap determination for both protocols

An optical band gap of 1.49 eV, protocol 1, and 1.60 eV for protocol 2 were obtained. The observed widening of the optical band gap from protocol 1 to protocol 2 is due to the crystallite formation at the substrate-film interface for protocol 2. The widening of the optical band gap with crystallite volume fraction was also observed by Waman *et al.* [5.29].

An increase in defect density has a direct relation to the structural order within a thin film [5.30]. The presence of defects, such as dangling bonds, would result in the extension of band tails into the E_g [5.31]. Thus since sample protocol 1 has a lower E_g than sample protocol 2, we infer it has a greater defect density and thus an increased structural disorder, as previously confirmed by Raman analysis.

5.5 Conclusion

An alternative deposition procedure of silicon thin films by HWCVD, using two deposition protocols, i.e. by either increasing or decreasing hydrogen dilution during the deposition run, has been demonstrated in this study. Deposition conditions that initiates with a 95% H-dilution results in the formation of Si nano-crystallites on the substrate-film interface, not detected by the XRD or Raman techniques. TEM analysis confirms a reduced density of nano-voids in the growth direction for both deposition protocols. Raman analysis reveals θ_b of 7.20° for protocol 1 and 6.95° for protocol 2, indicative of a highly ordered structure. Structural analysis by FTIR reveals a larger structural inhomogeneity for protocol 2. Both sample protocols obtained C_H amounting to ~ 9 at.% with a relatively large molecular hydrogen concentration, as confirmed by ERD. SEM surface analysis exposes the relatively smoother surface for protocol 2 when compared to protocol 1.



Thickness determination done by TEM analysis confirms the thickness determined from optical modelling. Optical analysis, which accounts for the existence of voids, show that optical density of the samples remain constant with thin film thickness, thereby resulting in different absorption curves for the two protocols. Crystallite existence results in an increase in optical band gap and structural order from protocol 1 to protocol 2.

References

- [5.1] J. D. Kotlarski and P. W. M. Blom (2011) *Appl. Phys. Lett.*, **98**, 5.
- [5.2] Barry P. Rand, Peter Peumans, and Stephen R. Forrest (2004) *J. Appl. Phys.* **96**, 12, 7519.
- [5.3] P. Jayarama Reddy (2012) *Solar Power Generation: Technology, New Concepts & Policy*. Edition Illustrated. CRC Press, ISBN: 0415621100, 9780415621106, p39-41.
- [5.4] Simon M. Sze, Kwok K. Ng (2006) *Physics of Semiconductor Devices*. Edition 3, John Wiley & Sons, ISBN; 0470068302, 9780470068304.
- [5.5] Viral Y. Parikh (2007) *Studies of Two-terminal and Four-terminal Polycrystalline Thin Film Tandem Solar Cells Based on II-VI Materials*. The University of Toledo, ProQuest, ISBN; 0549403760, 9780549403760. p20-26.
- [5.6] C. J. Arendse, D. Knoesen and D. T. Britton (2006) *Thin Solid Films*. 501, 92.
- [5.7] M.H. Brodsky, M. Cardona, J.J. Cuomo (1977) *Phys. Rev. B*. 16, 3556.
- [5.8] H. Shanks, C.J. Fang, L. Ley, M. Cardona, F.J. Desmond, S. Kalbitzer (1980) *Phys. Status Solidi B*. 100,43.
- [5.9] H. Looyenga (1965) *Physica*. 31,636.
- [5.10] A. M. Brockhoff (2001) *Hydrogen-Related Modifications of Amorphous Silicon and Silicon Nitride*, Ph.D. thesis, Utrecht University.
- [5.11] S.Y. Lien, H.Y. Mao, B.R. Wu, R.H. Horng, D.S. Wu (2007) *Chem. Vap. Deposition*. **13**, p247–252.
- [5.12] A. Heya, A. Izumi, A. Matsuda, H. Matsumura (2000) *Jpn. J. Appl. Phys. (Part I)*, **39**, p3888–3895.
- [5.13] M. Fang, J.B. Chevrier and B. Drevillon (1991) *J. Non-Cryst. Solids*. **137**, 791.
- [5.14] D. Han, K. Wang, J.M. Owens (2003) *J. Appl. Phys.* **93**, 3776.
- [5.15] G. Lucovsky, R. J. Nemanich and J. C. Knights (1979) *Phys. Rev. B*. **19**, 2064.

- [5.16] A. J. M. Berntsen (1993) *Structural Disorder in Pure and Hydrogenated Amorphous Silicon*, Ph.D. thesis, Utrecht University, Utrecht, The Netherlands.
- [5.17] W. C. Sinke, T. Warabisako, M. Miyao, T. Tokuyama, S. Roorda and F. W. Saris (1988) *J. Non-Cryst. Solids*. **99**,308.
- [5.18] I. Solomon, B. Drevillon, H. Shirai and N. Layadi (1993) *J. Non-Cryst. Solids*. 989, 164.
- [5.19] Pereyra, Alayo (2002) *Thin solid Films*. **402**, 161.
- [5.20] J.K. Rath, L.A. Klerk, A. Gordijn, and R.E.I. Schropp (2006) *Sol. Energy Mater.Sol.Cells*. 90, 3385.
- [5.21] 4.36 F.C Marques, P. Wickboldt, D. Pang, J.H. Chen and W. Paul (1998) *J. Appl. Phys.* **84**, 3118.
- [5.22] A. Matsuda (1983) *J. Non-Cryst. Solids*. 767, 59.
- [5.23] D.A.G. Bruggeman (1935) *Ann. Phys.* 24, 385.
- [5.24] W. Theiss and S. Hilbrich (1997) *Properties of porous silicon, edited by Leigh Canham*, INSPEC, The Institution of Electrical Engineers.
- [5.25] S. K. O’Leary, S. R. Johnson, and P. K. Lim (1997) *J. Appl. Phys.* 82, 3334.
- [5.26] Software available at www.mtheiss.com.
- [5.27] S.Furukawa and T. Miyasato (1988) *Phys. Rev. B*. **38**, 8, 5726.
- [5.28] W. Li, D. Xai, H. Wang and X. Zhao (2010) *Journ. Non-Cryst. Sol.* **356**, 44, 2552.
- [5.29] V.S. Waman, A.M. Funde, M. M. Kamble, M. R. Pramod, R. R. Hawaldar, D. P. Amalnerkar, V. G. Sathe, S. W. Gosavi, S. R. Jadkar (2011) *J. Nanotechnology*,1.
- [5.30] K. Winer (1991) *Annu. Rev. Mater. Sci.* **21**.
- [5.31] P. A. Fedders, D.A. Drabold and S. Nakhansen (1998) *Phy. Rev. B*. **58**, 23, p624-631.

SUMMARY

In the world of nano science the intrigue into hydrogenated nanocrystalline silicon (nc-Si:H) is immense. With the unique features and character as a result of quantum size effects on the nano scale, nc-Si:H it exhibits exceptional properties in favour of solar application. Although, a downfall of nc-Si:H are the cracks that form within the thin film as a result of crystallite formation. These cracks provide alternative recombination routes for electrons and holes, which are undesired for both single and bi- junction solar cells.

An in depth look into the history of solar energy and its application, along with the properties of amorphous and nanocrystalline silicon thin films are revealed in chapter one. Hot wire chemical vapour deposition (HWCVD) holds a vast amount of potential for low cost, mass production of thin films. In chapter two the HWCVD system is explored, from the practical setup and gas inlet system to the growth process of amorphous and nanocrystalline silicon thin films. This is followed by an investigation of the analytical technique used for the characterisation of the various thin films deposited.

The scene has now been set and the knowledge gained in the previous chapters, we investigate specifically deposited thin films, which unveiled crucial information on the various characteristics attained at these deposition regimes. At extreme dilution conditions the initial signs of crystallinity; hexagonal (002) silicon diffraction plane, is observed. The void-rich nature of the thin films was evident from FTIR and SEM analysis. The coalescence of grains, indicating growth toward phase change from amorphous to protocrystalline is seen,

despite absence of substrate heating. The effects of hydrogen dilution were visible, not only at the deposition rate but its surface roughness and H₂ molecules being trapped in voids.

With this insight we unravel the complex nature of the two thin films as a consequence for the dynamic deposition procedure by HWCVD. Two deposition protocols have been used, namely; the increasing (protocol 1) or the decreasing (protocol 2) of hydrogen dilution during the deposition. We have shown that the growth of the sequentially deposited thin films is not merely a stacking up of the various deposition layers and its resulting properties, but the growth and resulting properties vary with depth. The resulting films did not have a layer by layer appearance, but instead appeared as a continuous thin film. These films exhibited voids extending from the substrate and becoming smaller and more elongated, tending toward the surface of both deposition protocols. For the reversed deposition procedure (protocol 2), an ordered region is seen at the substrate-film interface, which is not seen for the deposition protocol 1. Interesting optical behaviour is observed, whereby the deposition procedure, protocol 1, is more absorbing in the visible range and protocol 2 is more absorbing in the UV-range. This result is as a consequence of the variation in optical character along the growth direction of these two thin films. Deposition protocol 1 appeared optically denser in the bulk region and protocol 2, at the surface region.

It is thus concluded that there exists a structural and optical variation along the growth direction of the two thin films, when the dynamic deposition procedure is performed at those specific deposition regimes. For future work, to truly understand this material, the presence of voids should be further investigated by means of small-angle x-ray scattering (SAXS). SAXS could be used to determine the number and size of these nano-voids present within the thin films. More insight into the potential of this type of deposition procedure is required. The eventual desire is that this multi-structured, intrinsic-layer thin film could possibly replace the

Summary

traditional multi-layered silicon thin film structure used in tandem solar cell, and elimination the issues brought forth at the junction between two solar cells of a tandem solar cell.

